Simulations of bulk and confined bubble nucleation

SAPIENZA
UNIVERSITÀ DI ROMA

Facoltà di Ingegneria Civile e Industriale
Dipartimento di Ingegneria Meccanica e Aerospaziale

Dottorato di ricerca in Meccanica Teorica e Applicata
XXXI Ciclo

Simulations of bulk and confined bubble nucleation

Sara Marchio

A thesis submitted for the degree of
Dottore di Ricerca

Advisor
Dr. Simone Meloni

Co-Advisor
Dr. Alberto Giacomello

Contents

List of Publications

Published

- **Marchio, S.**, Meloni, S., Giacomello, A., Valeriani, C., and Casciola, C.M. *"Pressure control in interfacial systems: Atomistic simulations of vapor nucleation."* The Journal of chemical physics 148.6 (2018): 064706.

Submitted

- **Marchio, S.**, Meloni, S., Giacomello, A., and Casciola, C.M. *"Inertial effects in wetting and drying of nano-patterned surfaces"* Submitted to Physical Review Letters.

Ongoing work

- **Marchio, S.**, Meloni, S., Giacomello, A., Valeriani, C., and Casciola, C.M. *"Dynamical effects in thermally activated bubble nucleation pathways."*. In preparation.

List of Figures

Abstract

The present thesis investigates, with atomistic simulations, vapor nucleation and liquid dynamics under nanoscale confinement. The main objective of this work is to go beyond the quasi-static classical picture of liquid-vapor phase transition, including kinetic and inertial effects. The performed simulations provide an accurate description of the phenomenon and a framework to interpret experimental observations. The dynamics of vapor nucleation is investigated in the pure bulk liquid and in confined conditions. In the last case, also wetting transition is studied.

Particular attention is devoted to surfaces that combine textured geometries with an hydrophobic chemistry. These are able to stabilize vapor phase within surfaces asperities, producing a state in which liquid is suspended above the entrapped vapor pockets. In these conditions, remarkable properties arise that are collectively known as superhydropobicity. In this suspended state, known also as Cassie-Baxter state, the contact area between solid and liquid is reduced with respect to a flat surface and with respect to the textured surface in which the corrugations are flooded with the liquid. Moreover, the liquid presents a higher contact angle (CA), with a lower CA hysteresis and a reduced liquid-solid friction. Due to these properties, superhydrophobic surfaces are suitable for applications such as self-cleaning glass, window, and wall paint. They prevent moisture accumulation, help anti-icing, and allow dropwise condensation to increase the heat transfer efficiency and water harvesting. These are all in-air applications. However, the presence of a large shear free liquid/gas interface suggested that super-hydrophobic surfaces can be used in many submerged applications, e.g. drag reduction, anti-friction, anti-adhesive, anti-corrosion, and boiling heat transfer.

Cassie-Baxter state can be destabilized by changes in pressure and temperature, that produce the intrusion of the liquid within surface defects. The corresponding state in which the surface is completely wetted is known as Wenzel state. The loss of super-hydrophobic properties (Cassie-Baxter to Wenzel transition) has proved to

be experimentally irreversible. It is therefore crucial to characterize both wetting and recovery mechanisms in order understand how to design surfaces supporting a robust Cassie-Baxter state, *i.e.* a suspended state that can resist to temperature and pressure fluctuations.

Wetting transition and recovery of superhydrophobic state take place via vapor/liquid and liquid/vapor phase transitions occurring under confinement at the nanoscale within geometric defects. Over the last decades, a significant amount of experimental and theoretical work has been devoted to the study of confined liquid-vapor transition. In spite of this, not much is known yet about the kinetics of the process. The contribution to the topic obtained during the three years of my PhD is presented in this thesis.

The first part of the work has been devoted to develop and test Molecular Dynamics and Monte Carlo methods able to properly simulate multiphase systems. Indeed, it has been demonstrated that serious issues arise when the standard global barostats, developed to simulate bulk systems, are straightforwardly applied to systems with subdomains at different pressures, e.g. liquid and vapor domains during nucleation. A solution to overcome these artifacts has been proposed, consisting in the implementation of a local barostat that imposes a local force balance between a piston and the contacting liquid. With this approach, a more accurate prediction of the vapor nucleation barrier in a super-heated liquid has been obtained.

Secondly, the simulation techniques developed at the first stage of my PhD work have been employed to study homogeneous bubble nucleation. At the liquid pressure and temperature here investigated, this phenomenon is a rare event: the waiting time to observe the inception of vapor formation is order of magnitude longer than the typical time that can be explored by atomistic simulations. This issue, that causes waste of computational resources, has been tackled by carefully selecting special techniques able to preserve kinetic and inertial effects during bubbles growth. With this approach, "dynamical" quantities have been estimated, e.g. the nucleation rate. Other two essential aspects have been addressed: the limits of theoretical expressions routinely used to evaluate the kinetic prefactor in Eyring equation for vapor nucleation; the relation between successful nucleation events and relevant observables, such as temperature and liquid velocity, at beginning and during bubble expansion.

The last section of this thesis is focused on heterogeneous nucleation and wetting of super-hydrophobic surfaces. Recent theoretical and experimental studies have produced conflicting results in the characterization of the pathways by which liquid intrudes in pores. The disagreement resides, specifically, in the symmetry properties

expected for the advancing meniscus shape. Experiments show a symmetric pathways, in which the liquid penetrates in the surface pores with an essentially flat meniscus, while quasi-static theories predict that the asymmetric pathway is more probable, in which the liquid entering in the surface cavities bend forming a bubble in a corner. My simulations have proved that inertial effects change the wetting and recovery path with respect the predictions of quasi-static approaches. This reconcile theory and experiments: when the transition is barrierless, as expected in experimental conditions in which only nearly spontaneous processes can be addressed, the more complete theory developed here predicts a symmetric wetting as observed in the experiments.

Chapter 1

Introduction

Liquid/vapor phase transition in hydrophobic confinement has a wide relevance in many fundamental and applicative contexts. In biology, water evaporation between hydrophobic surfaces plays a role in protein folding, biomolecular and colloidal assemblies [Chandler, 2005]. In the field of energetics, water intrusion/extrusion in/from hydrophobic porous systems allow energy dissipation, accumulation and restoring, by producing a reciprocal transformation of mechanical energy into interfacial energy [Eroshenko et al., 2001]. In the context of superhydrophobicity, liquid to vapor and reverse vapor to liquid phase transitions produce the inception and loss of the Cassie (or super-hydrophobic) state [Cassie and Baxter, 1944], when occurring within the asperities of geometrically textured and chemically hydrophobic surface. Superhydrophobicity refers to a set of remarkable surface properties arising when stable vapor pockets are trapped in the surface corrugations. The replacement of a portion of the liquid/solid interface with a shear-free liquid/vapor interface produces a decrease in the liquid drag under flow conditions. Superhydrophobicity is therefore well suited for drag reduction applications [Truesdell et al., 2006, Daniello et al., 2009], *e.g.* in microfluidic devices or marine vessels. Superhydrophobicity is also important for emerged applications, *e.g.* to enhance vapor condensation [Enright et al., 2014b], energy application or for water harvesting [Zhang et al., 2008]. Super-hydrophobic state can collapse via the cavitation of the vapor pockets entrapped in the asperities or via the liquid intrusion into the surface defects. The last event corresponds to the wetting transition, that leads to *Wenzel* state [Wenzel, 1936]. Once that Cassie to Wenzel transition occurs, superhydrophobicity and the related properties can be hardly recovered [Giacomello et al., 2012b]. Indeed, the recovery process is hindered by very high energy barriers. As a consequence of this difficulty, the design of super-

hydrophobic surfaces aimed at enhancing the stability of Cassie state requires the development of robust models able to describe both wetting (Cassie to Wenzel) and recovery (Wenzel to Cassie) mechanisms. The last one can be associated to a vapor nucleation event occuring under confinement, within the surface groove.

Due to the wide range of lenght and time scale involved, confined vapor nucleation and wetting phenomena can be hardly addressed both theoretically and experimentally. In some thermodynamical conditions these transitions are thermally activated: there is a scale separation between the short duration of the events, and the waiting time to observe their inception, that instead could be significantly long. In experiments, small lenght scales prevents to capture important details about the mechanism. As an example, it could be difficult to tell whether bubble nucleation is occuring in homogeneous conditions, or it is triggered by the presence of impurities [Caupin and Herbert, 2006].

Theoretical models routinely used to study liquid/vapor phase transition are based on a continuum description. Basic assumptions are that the interface between the phases is sharp and that the transition is a quasi equilibrium process. The last one implies that, at each point of the progress in the transition, the system has ideally enough time to relax to the conditional equilibrium configurations. Sharp interface and quasi equilibrium assumptions are in some cases not accurate: the thickness of the liquid/vapor interfaces could not be negligible especially near spinodal conditions [Cahn and Hilliard, 1959, Gallo et al., 2018], and kinetic or inertial effects may arise producing deviation of the actual path from the expected one. In this context, the atomistic description of the fluid in terms of its fundamental components provides the tool of choice to overcome the sharp interface assumption. Moreover, the dynamical simulation of phase transitions using *e.g.* Molecular Dynamics can be employed to validate theory and get insights on the mechanism.

The aim of this thesis is the study of the dynamical properties of liquid/vapor (bubble nucleation) and vapor/liquid (wetting) transitions under hydrophobic confinement at the nanoscale. Atomistic simulations of submerged super-hydrophobic surfaces are devised using techniques able to preserve intertial effects during transitions. The problem of vapor nucleation in a bulk liquid (homogeneous conditions) has been also addressed as benchmark, evaluating dynamical properties such as nucleation rate or bubble expansion velocity. Significant effort has been devoted at the first stage of this PhD work in developing and testing simulation protocols able to reproduce, at the atomistic scale, thermodynamical conditions typical of experiments and continuum theories. In particular barostat developed for bulk simulation proved

to be unable to control liquid pressure during bubble growth. To overcome this issue, a new local barostat has been devised, based on the force balance between the liquid and solid walls acting as pistons [Marchio et al., 2018].

1.1 Homogeneous vapor nucleation

This section is aimed at introducing the process of vapor growth within bulk liquid phase. In absence of impurities acting as nucleation sites, e.g. specks of dust, bubbles form via homogeneous nucleation. At given thermodynamic conditions, homogeneous nucleation is significantly less probable than heterogeneous nucleation, *i.e.* the inception of vapor phase in proximity of solid surfaces. Infact, the homogeneous process is suppressed by a significant higher energy cost with respect to the heterogeneous counterpart at a given thermodynamic state.

Due to this reason pure liquids can exist in a superheated metastable state, at temperature above the boiling point, until the inception of the new stable vapor phase. Similarly, liquid phase can exist in a stretched metastable state in which pressure is decreased below vapor saturation value [Debenedetti, 1996].

The probability of observing a bubble of volume V_V within a metastable liquid phase is proportional to the negative exponential of the grand potential variation with respect to the pure bulk liquid state:

$$\rho(V_V) \propto \exp(-\beta \Delta\Omega(V_v)), \tag{1.1}$$

where $\beta = 1/k_B T$ is the inverse of temperature in units of the Boltzmann constant k_B, and $\Delta\Omega(V_v) = \Omega(V_v) - \Omega(0)$. Classical Nucleation Theory (CNT) is the fundamental theory to obtain benchmark estimation of the energetic cost of forming a bubble in bulk liquid. Within CNT, the grand potential of a two phase (liquid/vapor) system, under the assumption that the interface is sharp, can be written as

$$\Delta\Omega(V_v) = \Omega(V_v) - \Omega(0) = \Delta P\, V_v + \gamma_{lv}\, A, \tag{1.2}$$

where $\Delta P \equiv P_l - P_v$ is the difference between vapor and liquid bulk pressures, γ_{lv} is the liquid/vapor surface tension and A is the bubble surface area. Under quasi-static assumption, the interface between the two phases relaxes to the conditional equilibrium configuration. In homogeneous nucleation, the spherical shape of the bubble minimizes energetic cost associated to the interface $\gamma_{lv}\, A$. The quasi static or quasi equilibrium CNT path is therefore a succession of spherical bubbles of growing

radius. The terms in Eq. (1.2) have the shape shown in Fig. 1.1. The maximum of the profile $\Delta\Omega(V_v^*)$ is the nucleation barrier, occurring at the bubble critical volume $V_v^* = (32\pi/3)(\gamma/|\Delta P|)^3$. For $V_v > V_v^*$, the free energy profile decreases. Therefore, once that bubble volume has reached this value, the transition to vapor state beomes a spontaneous process.

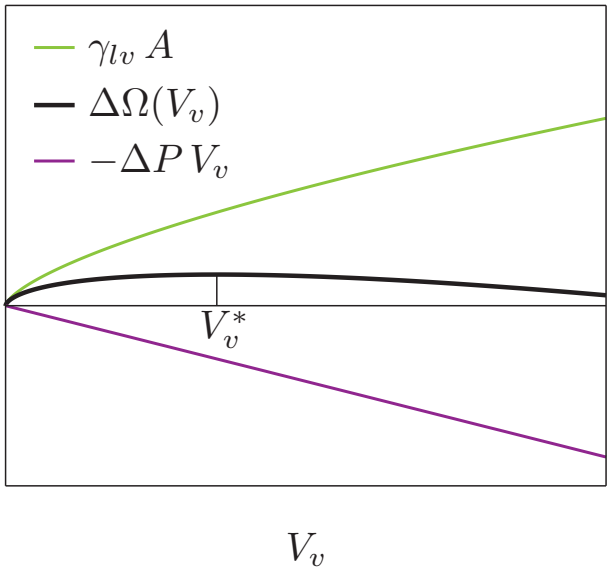

Figure 1.1: Black line is homogeneous nucleation grand potential as a function of the volume of the spherical bubble. The green line is the surface term, while the violet is bulk negative term. The maximum corresponds to the critical bubble volume.

From experimental point of view, there are intrinsic difficulties in obtaining insights into homogeneous nucleation mechanism. Typical time intervals to observe the inception of the process are significantly longer than bubble nucleation events. Moreover, due to the small lenght scales involved, it is difficult to tell wether vapor growth starts in the liquid bulk or in proximity of impurities. At ambient conditions, CNT estimates the limit of stretched metastable water at -140 MPa. Up to date, the only experimental technique able to approach such value exploits water inclusions in quartz [Zheng et al., 1991, Azouzi et al., 2013].

As we said before, nucleation starts at the atomistic scale and is driven by thermal fluctuations. Thus, atomistic simulations, molecular dynamics (MD) and Monte Carlo (MC) are the ideal tools to investigate the inception of the liquid-to-vapor phase transition. Differently from CNT, in molecular simulations bubble shape can be in principle non spherical and liquid/vapor interface can have a non zero thickness. Several molecular simulations studies [Shen and Debenedetti, 1999, Wang et al., 2008,

Meadley and Escobedo, 2012] have shown that bubbles have ramified rather than spherical shapes. The istantaneous interface of a growing bubble in a super-heated Lennard-Jones liquid simulated with Molecular Dynamics [Meadley and Escobedo, 2012] is shown in Fig. 1.2. The shape appears irregular, oblong and with small bumps reaching out from the main bubble. Similar results has been obtained in the same work for a stretched liquid.

One of the issues arising when phase transitions are studied with Molecular Simulations is connected to the huge time intervals spent in the metastable state before that a nucleation event allows the transition to the stable vapor state. This problem, typical of thermally activated event with high energy barriers, is usually referred to as the "rare events" problem. It will be presented in the next section, with a brief introduction to the different classes of rare events methods, devised to avoid waste of computational time.

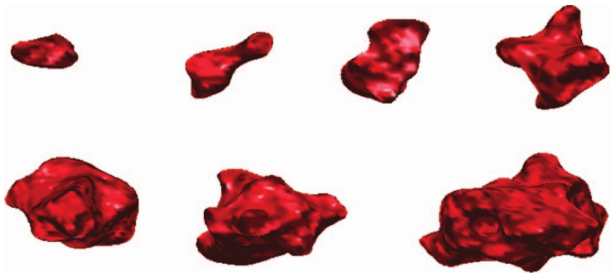

Figure 1.2: Istantaneous interfaces of a growing bubble within a metastable superheated Lennard Jones liquid, obtained in [Meadley and Escobedo, 2012].

1.2 The rare events problem

Rare events in computer simulations are processes that occur on timescales significantly larger than those accessible with brute force calculations. These processes include phase transitions, chemical reactions, as well as conformational changes and translocation in biological systems. Rare events can be described as transition between metastable states, i.e. local minima of the free energy landscape. If the barrier separating metastable states is higher than available thermal energy, the system will spend most of the time in proximity of the basins. The dynamics is therefore characterized by a long permanence in the metastable states, with fast and infrequent transitions from one metastable state to another. A sketch of the dynamics in generic bistable energy landscape is shown in Fig. 1.3, from Ref. [Bonella et al., 2012].

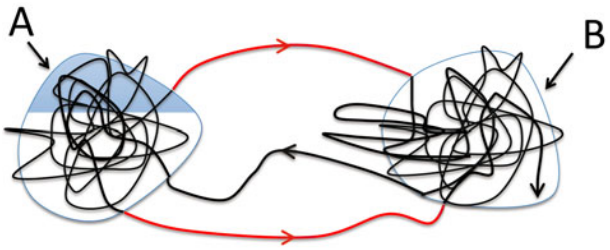

Figure 1.3: Trajectory in the phase space of a system moving in a free energy landscape with two metastable states A and B, separated by high but finite barriers. The two basins are the shaded areas, while transition from A to B are indicated with red lines. [Bonella et al., 2012].

The two metastable states are called A and B. Sometimes, if state B is much more stable (lower energy) than A, only the "direct" transition from A to B is observed. For example, in the case of homogeneous bubble nucleation, the initial metastable basin corresponds to the liquid state, where the system spends a long time before bubble growth starts. Once that nucleation free energy barrier is overcome and the system is in the vapor state, the inverse transition cannot be observed. The free energy of the vapor phase is indeed much lower than the free energy of the liquid phase.

In order to reduce computational efforts connected to the simulation of thermally activated events, a wide variety of rare events techniques have been developed. These can be classified in two main classes. In the first class, the kinetics and mechanism of the process is addressed by reconstructing the free energy landscape as a function of appropriate order parameters. The concepts of order parameter will be discussed in the methods section of this thesis, introducing the use of the collective variables. Umbrella Sampling (US) [Smith and Frenkel, 2002], Metadynamics [Laio and Gervasio, 2008], Thermodynamic integration [Sprik and Ciccotti, 1998], Temperature Accelerated Molecular Dynamics (TAMD) [Maragliano and Vanden-Eijnden, 2006a] and Restrained Monte Carlo (RMC) [Elena et al., 2013] are examples of these methods. They exploit a biasing potential in addition to the physical potential, to force the sampling of unprobable regions of the phase space, whose states are compatible with a fixed value of the order parameter. By eliminating a posteriori the effect of the biasing term, it is possible to reconstruct the free energy profile via appropriate procedures. The second group of rare events methods includes techniques aimed at obtaining statistical information on the dynamical transition paths from one free energy basin to another. Dynamical paths are crucial to get insights on the mech-

anism of thermally activated events. Therefore, when interest is aimed at kinetic and inertial effects, the second class of rare events techniques must be adopted. The importance of dynamical effects in bubble nucleation and wetting phenomena is one of the key points addressed in this thesis and will be widely discussed in the following. Transition path sampling (TPS) [Bolhuis, 2003] and Forward Flux Sampling (FFS) [Allen et al., 2006b] are examples of techniques aimed at the sampling of reactive paths. In the Methods section of this thesis RMC and FFS will be described in detail, since they have been employed to obtain the results discussed in this thesis. For a detailed discussion of rare events, the reader can refer to [Bonella et al., 2012].

1.3 Heterogeneous vapor nucleation

Heterogeneous vapor nucleation occurs at a surfaces of *e.g.*impurities or solid walls. Classical Nucleation Theory introduced in Sec. 1.1 for bubble nucleation in bulk liquid can be extended to include solid surfaces in the model [Skripov et al., 1988]. Within sharp interface and quasi equilibrium assumptions, results show that heterogeneous process is greatly enhanced with respect to the homogeneous counterpart, since it has smaller energetic cost. As a consequence, apart notable exeptions [Azouzi et al., 2013] vapor nucleation is always heterogeneous. The grand potential for a solid−liquid−vapor system is

$$\Omega = -P_l V_l - P_v V_v + \gamma_{ls} A_{ls} + \gamma_{lv} A_{lv} + \gamma_{sv} A_{sv}, \tag{1.3}$$

where it is taken into account the cost for each sharp interface between solid (s), liquid (l), and vapor (v) phases. When solid surface is flat, vapor nucleus is a spherical cap (see Fig. 1.4(a)). The contact angle θ_Y, where Y stands for Young angle, satisfies the following relation:

$$\theta_Y \equiv (\gamma_{vs} - \gamma_{ls})/\gamma_{lv}. \tag{1.4}$$

Expliciting grand potential (1.3) for heterogeneous nucleation on a flat surface reads

$$\begin{aligned}\Delta\Omega(V_v) \equiv \Omega(V_v) - \Omega(0) &= \Delta P\, V_v + (\gamma_{vs} - \gamma_{ls})A_{vs} + \gamma_{lv}A_{lv} \\ &= \Delta P\, V_{sp}\left[\frac{1}{4}(1+\cos\theta_Y)^2(2-\cos\theta_Y)\right] \\ &+ \gamma A_{sp}\left[\frac{1}{4}(1+\cos\theta_Y)^2(2-\cos\theta_Y)\right] \\ &= \Delta\Omega(V_{sp})\left[\frac{1}{4}(1+\cos\theta_Y)^2(2-\cos\theta_Y)\right]\end{aligned} \tag{1.5}$$

where V_{sp} and A_{sp} are volume and area of a spherical bubble with the same radius as the cap, and $\Delta\Omega(V_{sp})$ is the homogeneous CNT barrier of a bubble having volume V_{sp}.

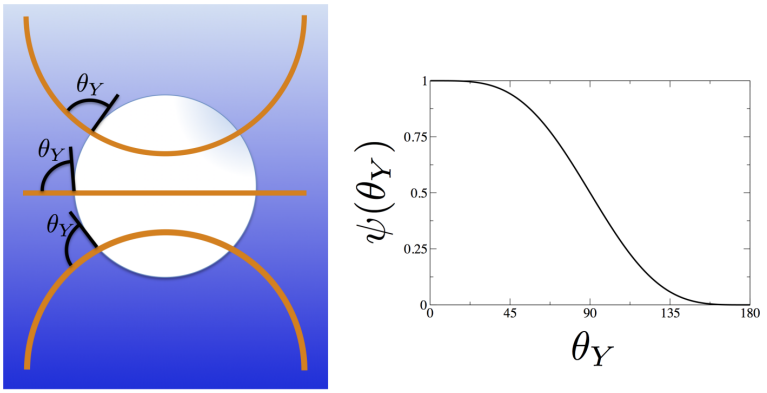

Figure 1.4: Vapor bubble nucleating on a concave (top), flat (middle), and convex (bottom) surface. The angle θ_Y is the Young contact angle. (b)Wetting angle function.

The term in the square brackets $\psi(\theta_Y) = \left[\frac{1}{4}(1+\cos\theta_Y)^2(2-\cos\theta_Y)\right]$ is called wetting angle function. Its monotonically decreasing profile is shown in Fig. 1.4(b).

Since $\psi(\theta_Y) \leq 1$, free energy barrier in the heterogeneous case is smaller than homogeneous counterpart. This explains why in actual systems vapor nucleation occurs at surfaces.

1.4 Superhydrophobicity

In this thesis, the broad issue of thermodynamical and dynamical characterization of liquid/vapor transition paths under confinement has been addressed in the specific framework of superhydrophobic surfaces.

Superhydrophobicity, or Cassie-Baxter state, arises from the stabilization of vapor pockets within the surface defects of an hydrophobic surface. Liquid droplets deposited on superhydrophobic surfaces exibits an high contact angle (the angle where the liquid/vapor interface meets the solid) with low hysteresis. In general, the hysteresis of the contact angle originates from pinning and depinning from geometrical defects when liquid advances or receeds above the surface [Johnson Jr and Dettre, 1964, Joanny and De Gennes, 1984]. Pinning of the triple line is sketched in Fig. 1.5, in which the range of the possible contact angles is shown for a sharp corner having angle φ.

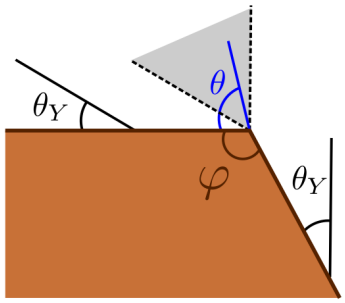

,

Figure 1.5: Range of possible contact angles $\theta_Y \leq \theta \leq \pi - \varphi + \theta_Y$ on a surface having a sharp corner with angle φ. The range of the possible contact angle at the corner is shown with the grey shaded area.

The actual angle θ of a static droplet deposited on a superhydrophobic surface is in the range $\theta_r < \theta < \theta_a$, where θ_r is the minimum contact angle just before drop movement, when the triple line (the line at which interfaces of the three phases meet) starts to reced from its pinned position, and θ_a is the maximum contact angle when the droplet is advancing.

The most important property arising from contact angle hysteresis is that a droplet can remain attached to the surface also when it is tilted. This would be impossible if the angles of the andvancing and receding side of the drop were the same. The force that balances gravity when surface is tilted is the hysteresis force defined as

$$H = \gamma_{lv}(\cos(\theta_r) - \cos(\theta_a)). \tag{1.6}$$

Hydrophobic chemistry and texturation of the surface allow to minimize this hysteresis force, promoting the mobility of the droplet [Lafuma and Quéré, 2003]. This property of superhydrophobic surfaces is known as "Lotus" effect and produces the self-cleaning ability. Indeed, rolling on the Lotus leaf droplets capture dust [Barthlott and Neinhuis, 1997], that is tipically hydrophilic.

There are several other examples of biological surfaces that exibit superior water-repellency properties. The nanogrooves on the microsetae structures of water striders legs allows their effortless movement on water. Salvinia molesta leaves are able to sustain an air layer when submerged, due to their egg-beater like shaped airs. These biomaterials have inspired researcher with the aim of create engineering applications both for submerged and in air applications. Indeed, in addition to self-cleaning, other properties arise from the low hysteresis of contact angle, such as non-wettability, and anti-biofouling.

1.4.1 Cassie and Wenzel model

In order to understand the origin of superhydrophobicity in ducks feathers, Cassie and Baxter imagined that the surface was not completely wet, and roughnesses were filled with air, with the subsequent formation of a flat liquid-vapor interface [Cassie and Baxter, 1944]. The configuration is schematically shown in Fig. 1.6 (right).

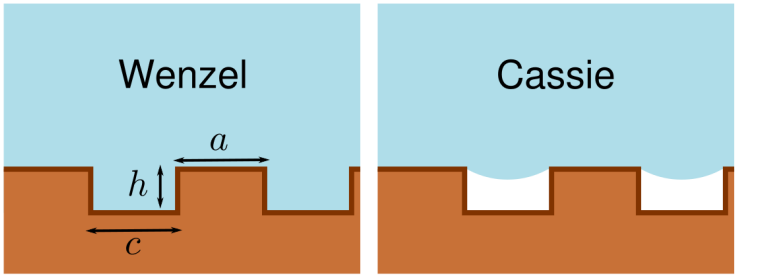

Figure 1.6: Sketch of superhydrophobic surface with rectangular grooves having height h, width c, and with crest widht a. Wetted Wenzel state is shown on the left, while Cassie state is shown on the right.

Defining f_1 and f_2 the area fractions corresponding to solid-liquid and liquid-vapor interfaces, the surface term in the grand potential normalized per unit of projected area is

$$\frac{\Delta\Omega^{(s)}}{A} = f_1(\gamma_{sl} - \gamma_{sv}) + f_2\gamma_{lv}, \tag{1.7}$$

where the reference surface grand potential is the one of pure liquid phase $\Omega^{ref} = \gamma_{sv}A_{tot}$. Using Eq. (1.7), the apparent contact angle can be defined, in analogy with Young relation (1.4), as [Cassie and Baxter, 1944]

$$\cos\theta^* = \frac{\Delta\Omega^{(s)}}{A\gamma_{lv}} = f_1\cos(\theta_Y) - f_2, \tag{1.8}$$

where $\theta_Y = (\gamma_{vs} - \gamma_{ls})/\gamma_{lv}$ is the Young angle defined in previous section. Eq. (1.8) can be generalized to solid with an heterogeneous chemistry or complex interfaces as

$$\cos\theta^* = \sum_i f_i\cos\theta_{Y,i}, \tag{1.9}$$

where $\theta_{Y,i}$ is the contact angle for chemistry i. From Eq. (1.9) it is clear that the appearent contact angle is a weighted average of the contact angle at different chemistries, where the weights are the relative area fractions. Defining the solid fraction when there is a sinlge solid spiecies as φ_s, Eq. (1.8) can be rewritten as

$$\cos\theta^* = \varphi_s\cos\theta_Y - (1 - \varphi_s), \tag{1.10}$$

known as Cassie formula. When the same system is considered in the completely wet state, the surface energy per unit of projected area is

$$\frac{\Delta\Omega^{(s)}}{A} = r(\gamma_{sl} - \gamma_{sv}), \tag{1.11}$$

where r is the roughness factor, defined as the ratio between actual surface and projected area. In this case the apparent contact angle is

$$\cos\theta^* = r\cos\theta_Y, \tag{1.12}$$

that is named after Wenzel, the first to derive it. Equations (1.10) and (1.12) are derived via energy arguments that can be summarized as $\cos\theta^* = -\Delta\Omega^{(s)}/(A\gamma)$. These correspond to the statement that, for hydrophobic surfaces, the system tend to maximize the apparent contact angle while, for hydrophilic surfaces, to minimize it.

This argument is shown in Fig. 1.7, where solid lines corresponds to the configurations having minimal energy between Cassie and Wenzel states. For $\theta_Y \sim \pi/2$,

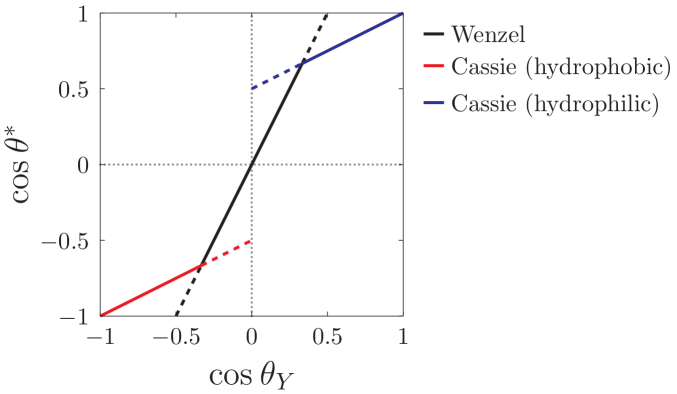

Figure 1.7: Apparent contact angle θ^* on a rough surface as a function of the Young angle. The values are predicted with Wenzel equation (1.12) (black line), Cassie equation (1.10) for an hydrophobic surface (red line), and Cassie equation (1.10) for an hydrophilic surface (blue line).

Wenzel state is more stable. For large θ_Y (hydrophobic surfaces), Cassie state is favoured. In presence of very hydrophilic surfaces, $\theta_Y < \pi/2$, the surface roughness are filled with liquid and the the contact angle is computed for a liquid solid surface with Eq. (1.9), where θ_Y of the liquid is zero. The corresponding state is called superhydrophilic. The coexistence angle for which surface energy of Wenzel and Cassie is the same is

$$cos\theta_Y = \pm\frac{1-\varphi_s}{r-\varphi_s}. \tag{1.13}$$

The results shown in Fig. 1.7 highlight that, under certain conditions, two states are possible corresponding to different surface energies. Dashed lines correspond to metastable states associated to an higher surface energy with respect to stable states, shown with solid lines. If Cassie and Wenzel state are separated by large free energy barriers with respect to the thermal energy, the transition from one state to the other is thermally activated and occurs on a long timescale. Next sections are devoted to discuss the state of the art in the characterization of wetting (Cassie to Wenzel) and dewetting (Wenzel to Cassie) transition paths. This subject has a fundamental relevance in an applicative context, since wetting transion produces the loss of the superhydrophobic state and all the related properties. Therefore the kinetic characterization of these transitions allows to identify design criteria to prevent wetting and favour the restore of Cassie state. In particular, the limits of the quasi equilibrium approach are discussed. This would provide a framework to

introduce the variety of dynamical effects that can be captured with the atomistic simulation carried out in this thesis, crucial to understand the kinetic mechanism of the transitions.

1.4.2 Wetting and nucleation paths at textured surfaces

Actual surfaces are usually characterized by complex geometries with defects and asperities. When a rough surface is combined with hydrophobic coating, the presence of trapped gas or vapor pockets has a catalytic action that strongly enhances the inception of cavitation, *i.e.*the expansion of vapor cavities when subject to negative pressures [Giacomello et al., 2013]. Cavitation of gas pockets, followed by the liquid replacing the gas in the cavity, is the first of the mechanism by which superhydrophobicity is lost. The second one is the intrusion of the liquid in the surface defects, *i.e.* the transition in the wetted Wenzel state.

One of the main method to investigate the mechanism of catalysis induced by surface defects is the one developed by [Atchley and Prosperetti, 1989] and applied to the crevice model. It is based on a force balance between the expanding forces, due to gas pressure within the bubble, and the collapsing ones, due to surface tension. The approach of crevice model is able to accurately evaluate the cavitation spinodal pressure of gas pockets trapped in axisymmetric asperities, *i.e.*the pressure at which the process occurs spontaneously with zero energetic cost. However, since the model is based on a mechanical derivation, it does not take into account metastabilities. Therefore, thermodynamical condition at which the process is thermally activated cannot be studied.

The approach adopted in Sec. 1.1 and 1.3 to study bubble nucleation in bulk liquid and near an ideally flat surface cannot be easly extended to investigate liquid/vapor phase transition under confinement in complex geometrie. Indeed, in presence of surfaces with generic shapes, the procedure of the minimization of the functional (1.3), that is able to highlight the presence of metastabilities, could be a difficult task. In these circumstances the analytic approach must be replaced by a numerical approach. The Continuum Rare Event Method (CREaM) has been developed to overcome this issue [Giacomello et al., 2012a]. Consistently with CNT, CREaM is based on the assumption that the process is quasi-static. It finds the most probable vapor domain configuration at a given value of vapor volume V_v. The procedure consists in a numerical minimization of the functional (1.3), conditioned to $V_V = const.$ The implementation for different values of V_v allows one to identify the expected quasi-static path, *i.e.* the sequence of configurations that minimize the

energetic cost along the transitions. The conditional minimization leads to two conditions. The first one is the Young equation for the contact angle θ_Y (see Eq. (1.4)), while the second one is the modified Laplace equation,

$$J = \frac{P_l - P_v - \lambda}{\gamma_{lv}}, \tag{1.14}$$

where $J = 1/R_1 + 1/R_2$ is twice the mean curvature of the interface between liquid and vapor and λ is the Lagrange multiplier necessary to impose $V_v = const.$ For $\lambda = 0$, *i.e.* when the system is at an extremal point (local minima, maxima, saddle points), the standard Laplace equation is recovered.

CREaM has been used to study vapor nucleation within asperities with several geometries. Bubble morphology and free-energy profiles in three different cases are reported in Fig. 1.8.

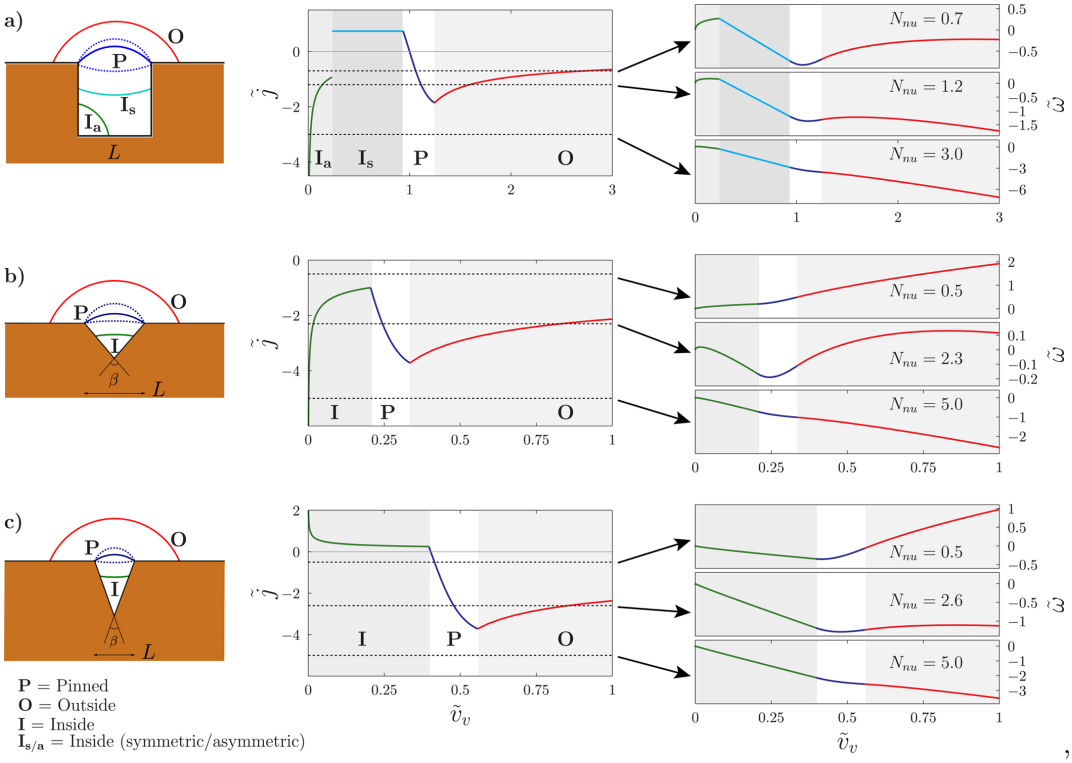

Figure 1.8: Nucleation paths (left), bubble curvature versus volume (center), and nucleation free energy profiles (right) computed with CREaM for (a) 2D squared pore and 3D (b) wide and (c) narrow conical crevice. Dimensionless quantities are used: $\tilde{V}_v = V_v/L^d$, where d is the dimensionality of the system and L is a characteristic lenght of the surface texture, $\tilde{j} = JL$ and $\tilde{\omega} = \Omega/(\gamma_{lv}L^{d-1})$. Free energy are shown for different nucleation numbers: $N_{nu} \equiv -L\Delta P/\gamma_{lv}$.

For the rectangular pore, the quasi-static approach of CREaM predicts a nucleation path that starts from one of the two bottom corners of the pore (green line). The meniscus then become simmetric and climbs up the pore until it gets pinned to the corners at the top of the corrugation (blue line). This first part is the dewetting transition from the Wenzel to the Cassie state. Finally, the triple line depins and the bubble grows as a circular segment (red line). Since the path is made of configurations that minimize the interface cost at each value of V_V, the wetting transition from Cassie to Wenzel state is expected to follow the same intermediate configurations under the quasi-static assumption (see Fig. 1.9). It is expected to start from the Cassie state with a flat meniscus intruding in the pore and finish with an asymmetryc bubble at one of the bottom corner of the pore that progressively collapses.

Atomistic quasi equilibrium free energy calculations confirmed the presence of an asymmetric bubble at the last stage of wetting and at the beginning of vapor nuclation within a square hydrophobic pore [Giacomello et al., 2012b].

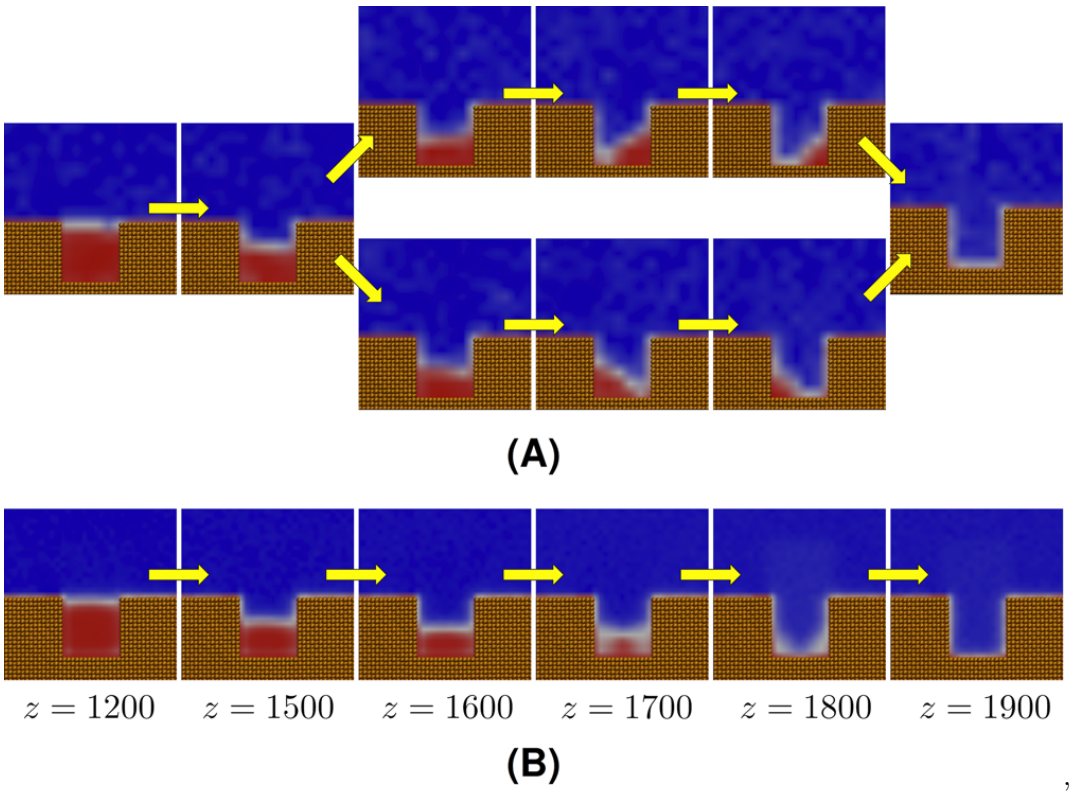

Figure 1.9: Atomistic transition paths from Cassie to Wenzel state. Panel (A) shows each of the two specular paths, while panel (B) shows their ensemble average.

The asymmetric quasi-static path of wetting and nucleation resulting from atomistic simulation and continuum calculation has been rarely observed in experiments. Laser Scanning Confocal Microscopy has been employed in [Lv et al., 2015] to observe *in situ* the last stage of the collapse of superhydrophobicity. Experiments reveal the presence of both symmetric and asymmetric meniscus (see Fig. 1.10). However, the observation of the asymmetric path has been attributed to the presence of hydrophilic impurities at the bottom of the pore, due to the prior liquid intrusion and extrusion within the same pore. When the bottom of the pore is textured, preventing the persistance of residual droplets, unlike simulations only symmetric pathway is observed (see Fig. 1.11).

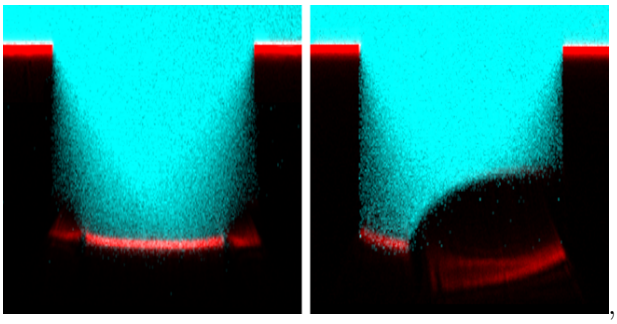

Figure 1.10: Symmetric (left) and asymmetric (right) configurations of bubble collapse within a micron-sized pore [Lv et al., 2015].

The mismatch between the quasi-static asymmetric path and the actual symmetric path observed in experiments suggest that quasi-static hypothesis of classical models might be, in some cases, not realistic. One of the main aim of this work is to perform atomistic simulations able to capture the dynamical effects that deviate the path from the expected quasi-equilibrium one, providing a framework to interpret experimental observations. Next section will be devoted to clarify the mechanism by which kinetic and inertial effects might affect transition paths.

1.5 Beyond quasi static picture: kinetic and inertial effects

Quasi-static continuum and atomistic methods introduced so far to describe wetting and nucleation phenomena assume that the system is always at the conditional equilibrium along transition paths from one metastable state to another. In other words, at each intermediate value of the variable that monitors the advancement in the

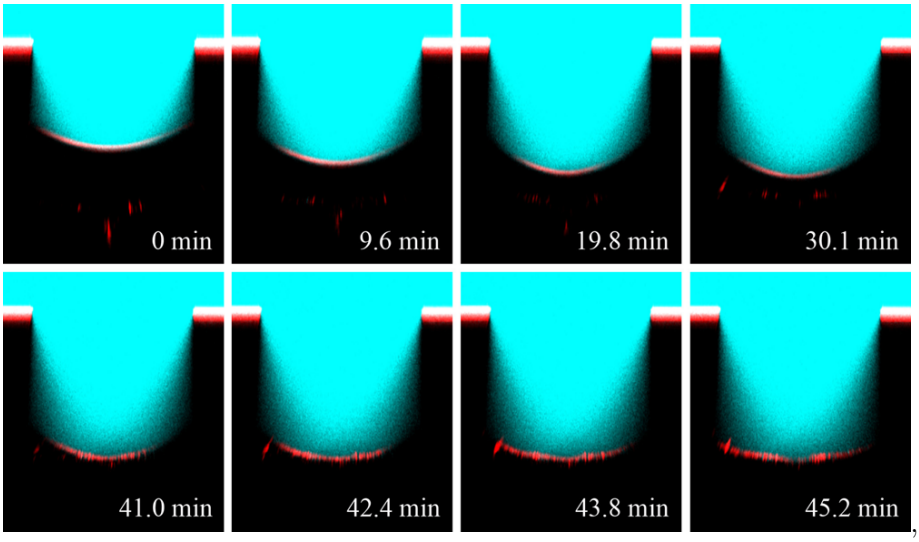

Figure 1.11: Liquid intrusion within a pore with textured bottom. The hierarchical structure prevents formation of residual droplets, therefore only symmetric path is observed [Lv et al., 2015].

transition path, the system oscillate around the minimum energy configuration. In the case of vapor nucleation within a bulk liquid and from a flat surface (Sec. 1.1 and Sec. 1.3), this condition implies a spherical shape of the forming bubble, since this configuration minimizes the energetic cost due to the formation of the liquid/vapor interface.

In the less trivial case of confined vapor nucleation and wetting, numerical studies have shown that the liquid/vapor meniscus shape is expected to be flat for low liquid filling level, and relax to a configuration with an asymmetric bubble at one of the bottom corner, when the liquid touches the bottom wall (see Fig. 1.9). However, quasi equilibrium is a strong assumption that might be violated in actual conditions, when the process occurs at finite speed. Indeed, under kinetic and inertial effects, actual transition paths may deviate from the ideal ones.

In [Wang et al., 2008], the role of kinects effects has been addressed in homogeneous bubble nucleation within a superheated liquid. Using atomistic simulations not based on the quasi equilibrium assumption, the authors demonstrated that the inception of vapor growth is triggered, at the first stage, by hot spots, *i.e.* local fluctuations of temperature above the equilibrium one. However, the role of hot spots and other dynamical phenomena in bubble nucleation has been questioned and is still an open question [Diemand et al., 2014].

In general, in order to investigate the mechanism of a transition revealing the

presence of kinetic effects, observables such as temperature, bubble expansion rate, or fluid velocity must be evaluated at different times along the same transition path. This would allow to highlight *e.g* the presence of statistical correlation between the inception of the transition and the dynamical properties of the fluid before and during the event itself. Simulations should be therefore able to produce dynamical trajectories rather than a sequence of configurations at conditional equilibrium. Among simulation techniques able to go beyond quasi equilibrium picture, one possible approach is the one of Forward Flux Sampling that has been widely employed in this work, since it allows the sampling of reactive trajectories. The details of this technique will be described in Chap. 3.

Deviation from the reversible quasi equilibrium path may also arise as a consequence of the "*inertia*" of the system in its motion through the free-energy landscape. Within quasi-static picture, when the system is not at the conditional equilibium state, it is expected to relax to the minimum energy configuration. However, if the velocity is high enough along the reaction coordinate perpendicular to the relaxation direction, the system might not have enough time to reach the conditional equilibrium.

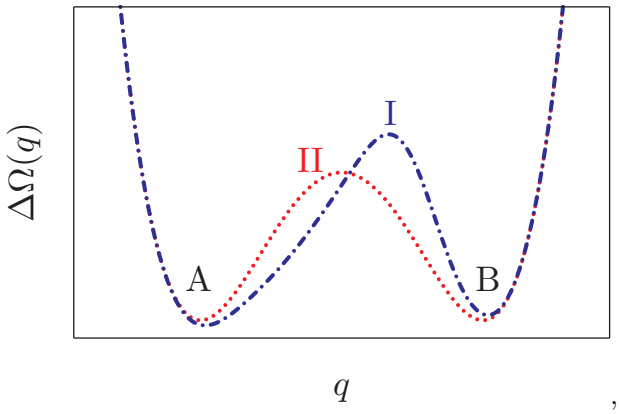

Figure 1.12: Separate reaction channels I and II that connect the two metastable states A and B. Channel I has the highest barrier but it can be preferred in the A to B transition since, near A, the slope of the profile is lower.

An illustrative case to introduce the effect of dynamics in one of the many possible scenarios is a free energy landscape with two metastable states, A and B, connected by two separated channels, I and II (see Fig. 1.12). The channel with the lowest barrier is II. Reasonably, transition from A to B would start more likely following channel I, since it has a lowest slope and therefore the corresponding states will be

more populated. If inertia along the reaction coordinate q is high and the friction is low, the displacements to B would continue following this path, even if it has an highest free-energy barrier. From B to A, the system is instead expected to follow the channel II due to the fact that, near to B, it has the lowest slope. In this second case, the dynamical path is expected to correspond to the ideal minimum-energy barrier, that corresponds to the one that would be identified by quasi-static methods.

In general, if the transition is very fast, actual configurations might differ from the expected ones because the relaxation time could be comparable with the typical time of the transition. In the case of homogeneous bubble nucleation, at quasi equilibrium bubble is expected to be spherical at each stage. However, if the nucleation event starts with an elongated vapor cavity due to thermal fluctuations, the asymmetry might persist along the nucleation path if bubble expansion is very fast (see Fig. 1.13. The case of an asymmetric vapor bubble expansion, discussed in the results section of this thesis (Ch. 5), constitutes a dynamical effect that can be captured uniquely with dynamical simulations.

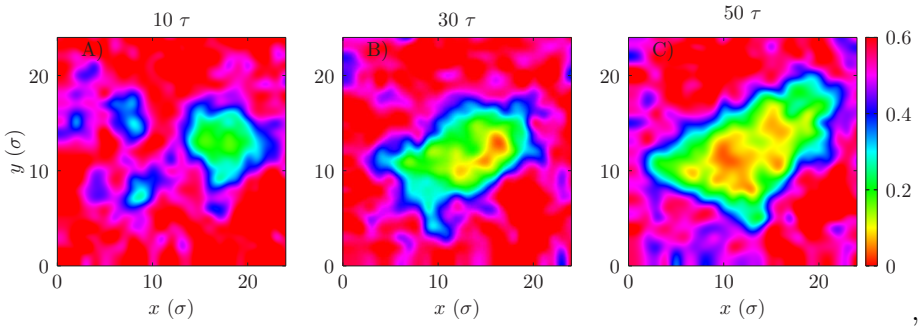

Figure 1.13: 2D Density field during vapor nucleation within a bulk super-heated liquid. The asymmetric shape, that can be interpreted as a deviation from the minimum energy path, is preserved during expansion.

This work also investigates how inertial effects affect vapor nucleation and wetting pathways under confinement in nanotextured surfaces. In this case a more complex phenomenology arises, connected to the symmetry properties of the liquid vapor meniscus during liquid intrusion and extrusion within pore.

The atomistic simulations presented in Ch. 6 are designed to investigate the origin of the mismatch between experimental and quasi-static transition during the liquid intrusion within a single pore discussed in previous section.

The free energy profiles of the vapor configurations between Cassie and Wenzel states has been evaluated in the atomistic and continuum calculations carried out in

Ref. [Giacomello et al., 2012b]. In the wetting of a square pore, theory predicts that the most probable quasi equilibrium path passes through the formation of a bubble at one of the two corners at the bottom of texturation. However, in the experiments performed in Red. [Lv et al., 2015], both the symmetric and asymmetric transition paths are found in the collapse of super-hydrophobicity on a surface patterned with cylindrical nanopores. Moreover, the authors identified the symmetric pathways as the "natural" one, attributing the asymmetric to the presence of impurities such as residual droplets due to a prior use of the surface.

1.6 Thesis outline and objectives

This thesis presents the results obtained in a three-year Ph.D. program in Theoretical and Applied Mechanics. The main objective is to design atomistic simulations able to overcome the quasi-static picture of liquid-vapor phase transition. The reconstruction of the actual transition paths is indeed crucial to characterize the dynamics of the process and to interpret experimental observations.

The first stage of the work consisted in developing and testing methods able to reproduce the properties of multi-phase systems within the framework of atomistic simulations. In a relatively small molecular systems ($\mathcal{O}(10^3)$ atoms), a barostat that keeps constant the global pressure, e.g. the Klein-Tobias-Martyna barostat [Martyna et al., 1994], proved to be unable to control liquid pressure during bubble growth and collapse. This circumstance prevents to properly compare simulations with experiments and theory. To overcome this issue, a new local barostat has been devised, based on the force balance between the liquid and solid walls acting as pistons.

Once tested with Monte Carlo simulations, the protocol has been applied to simulate homogeneous bubble nucleation including dynamical effects. Molecular Dynamics was combined with Forward Flux Sampling (FFS), that reproduces actual "reactive" trajectories. The dynamical properties of the system have been studied analysing time-dependent observables, such as bubble expansion rate. Moreover, simulation results allowed also to test the accuracy of forumulas routinely used to estimate kinetic prefactor Γ_0 in the Eyring expression (1.15) for the transition rate k:

$$k = \Gamma_0 \exp(-\beta \Delta\Omega(V_v^*)), \tag{1.15}$$

where β is the inverse of temperature in units of Boltzmann constant k_B, and $\Delta\Omega(V_v^*)$

is the free-energy barrier.

Heterogeneous vapor nucleation and wetting have been studied in the proximity of super-hydrophobic surfaces. Reactive trajectories have been obtained at different thermodynamic conditions. The study was aimed at clarifying a mismatch between the symmetry properties of the liquid/vapor meniscus observed in experiments and the one in quasi-static simulations. Investigating the dynamical behaviour at several pressure and temperature points allowed to discover the presence of multiple behaviors. In presence of relatively high energy barriers, dynamical trajectories follow the minimum energy path. When the process is barrierless, inertia plays a role inducing the meniscus shape to preserve the initial shape. An inertial and a non inertial regimes have been identified in both wetting and de-wetting transitions. Within this picture, that has a general validity, it is possible to develop a framework to interpret experimental observations.

The thesis is organized as follows. In part I, continuum and atomistic methods employed to study liquid/vapor phase transitions are discussed. In Ch. 2 Kramers theory is discussed to derive an explicit analytic expression to estimate the transition rate.

In Ch. 3, Molecular Dynamics algorithms and rare event methods adopded to simulate vapor nucleation and wetting are introduced. Among quasi-static techniques, Restrained Monte Carlo and Restrained Molecular Dynamics have been used to evaluate nucleation and wetting free energies barriers. RMC can be implemented using a non-analytical order parameter, i.e. the volume of the largest bubble in the bulk system, while RMD requires analytical order parameters such as the number of particles within a given volume in the simulation box. Dynamical trajectories are instead generated using Forward Flux Sampling.

In part II, results will be discussed in detail. In Ch. 4 ,reproducing the paper [Marchio et al., 2018],the simulation protocol devised to simulate the multi-phase system is presented. The results obtained in the case of homogeneous nucleation are disussed, showing that an improper choice of the barostat algorithm can significantly alter the values estimated for the nucleation rate. In Ch. 5, FFS results from the study of homogeneous nucleation are presented. The problem is addressed both from quantitative (estimation of transition rates) and qualitative (properties of reactive paths) point of views. In Ch. 6, kinetics of confined liquid/vapor phase transition is studied with Forward Flux Sampling. Transition paths in several thermodynamical conditions are analysed, showing the presence of an inertial regime, in which trajectories deviate from the expected quasi-static ones. This behaviour is addressed both

for wetting and de-wetting transitions. The final chapter is left for conclusions.

Part I

Methods

Chapter 2

Continuum methods

This part of the thesis is aimed at summarize continuum and atomistic simulation methods adopted in this thesis to characterize the energetic landscape, the kinetics, and the mechanism of liquid/vapor phase transitions. In the context of vapor nucleation and wetting of super-hydrophobic surfaces, these processes are studied analysing the role of metastabilities.

This Chapter is aimed at discussing how the free-energy profiles obtained with Classical Nucleation Theory, or other quasi equilibrium methods *e.g* CREaM (eq. (1.2)), can be used within the context of Kramers theory [Zwanzig, 2001] in order to evaluate the rate at which transitions occur. Firstly, the Kramers problem is introduced. Then, relevant quantities in Kramers formula will be estimated within CNT and other continuum theories.

2.1 Kramers problem and transition rate

Kramers problem consists in deriving an expression for the rate at which a Brownian particle escapes from a potential well over a potential barrier.

For a complete discussion of Kramers theory the reader is referred to [Zwanzig, 2001]. In Ref. [Jungblut and Dellago, 2016], Kramers theory is specialized to study nucleation and growth of crystals.

Kramers problem is sketched in Fig. 2.1. The process is described in terms of a particle of position q, representing the reaction coordinate, moving according to the overdamped dynamics over a potential $U(q)$:

$$\dot{q} = -D(q)\frac{\partial \beta U(q)}{\partial q} + \sqrt{2D(q)}\epsilon(t), \tag{2.1}$$

where $D(q)$ is the position-dependent diffusion coefficient, $\beta = 1/k_B T$ is the inverse of temperature in units of Boltzmann constant k_B, and $\epsilon(t)$ is Gaussian white noise. For a particle that moves accordingly to Eq. (2.1), one may be interested in the probability $P(q,t)$ that the particle is at the position q at time t. In the overdamped regime, $P(q,t)$ obeys the Smoluchosky equation [Zwanzig, 2001], that is a special case of Fokker-Plank equation valid in the limit of the overdamped regime:

$$\frac{\partial P(q,t)}{\partial t} = -\frac{\partial J(q,t)}{\partial q}, \tag{2.2}$$

where

$$J(q,t) = -D(q)\exp(-\beta U(q))\frac{\partial}{\partial q}\exp(\beta U(q))P(q,t). \tag{2.3}$$

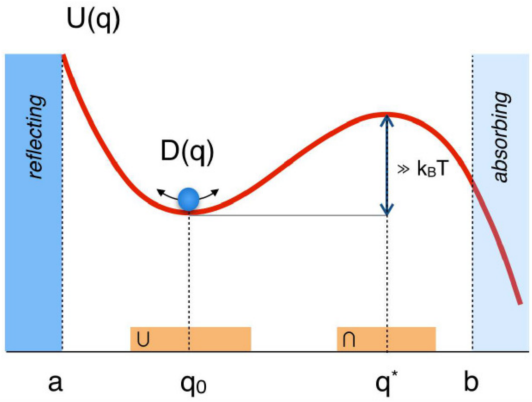

Figure 2.1: Sketch of Kramers problem: particle moves diffusively with coefficient $D(q)$ over the potential $U(q)$. In order to evaluate the escape rate from the well, a reflecting boundary is set at a while an adsorbing boundary is set at b. [Jungblut and Dellago, 2016]

Starting from expressions (2.2) and (2.3), the aim is to derive an expression for the mean first passage time (MFPT) $\tau(q)$, *i.e.* the mean time required for a system, starting from q_0, to reach q for the first time. A reflecting boundary is placed at a, before the basin ($a < q_0$), and an adsorbing boundary is placed in b, after the barrier ($b > q^*$).

The MFPT satisfies the adjoint equation of (2.2):

$$\exp(\beta U(q))\frac{\partial}{\partial q}D(q)\exp(-\beta U(q))\frac{\partial}{\partial q}\tau(q) = -1. \tag{2.4}$$

Dividing Eq. (2.4) by $\exp(\beta U(q))$, integrating over q, dividing by $D(q)\exp(-\beta U(q))$,

and integrating once more over q reads

$$\tau(q) = \int_{q_0}^{b} \frac{1}{D(x)} \exp(\beta U(x)) dx \int_{a}^{x} \exp(-\beta U(y)) dy. \tag{2.5}$$

In the study of the escape from a potential well over a barrier, Eq. (2.5) can be noticeably simplified. Assuming that $D(x)$ does not change significantly between a and b, one may notice that the variation of the first integrand is mainly due to the exponential term. This last is large where $U(x)$ is large, *i.e.* left and rigth of the well. Moreover, for values of x far apart on the left side of the well the inner integral does not have a significant contribution, since $\exp(-\beta U(y))$ have large large values only near the well region. As a consequence, the integration domain of the first integral of (2.5) can be restricted to the region near the top of the barrier, denoted by the symbol $\cap$. The inner integral of (2.5), is such that the main contribution in the integration domain is obtained in proximity of the potential well. Therefore, in this second case, integration can be carried out uniquely in the well region of the potential, denoted by $\cup$:

$$\tau(q) = \int_{\cap} \frac{1}{D(x)} \exp(\beta U(x)) dx \int_{\cup} \exp(-\beta U(y)) dy. \tag{2.6}$$

Assuming also that the shape of the potential is approximately parabolic near the top of the barrier, Eq. (2.6) can be further simplified adopting the Laplace method. Expanding $U(q)$ in Taylor series up to the second order, near the maximum of the profile q^*, one obtains

$$U(q) = U(q^*) - \frac{1}{2}\omega^2 (q - q^*)^2, \tag{2.7}$$

where ω^2 is the absolute value of the curvature at the top of the barrier $\omega^2 = \left|\partial^2 U(q)/\partial q^2\right|$, and $\partial U(q)/\partial q = 0$. Substituting the diffusion coefficient with a constant $D(q^*)$ equal to its value over the top of the barrier, and inserting (2.7) into (2.6), reads

$$\begin{aligned} \tau(q) &= \frac{\exp(\beta U(q^*))}{D(q^*)} \int_{\cap} \exp(1/2\beta\omega^2 (q - q^*)^2) dx \int_{-\infty}^{\infty} \exp(-\beta U(y)) dy \\ &= \frac{\sqrt{2\pi k_B T}}{\omega} \frac{\exp(\beta U(q^*))}{D(q^*)} \int_{\cup} \exp(-\beta U(y)) dy, \end{aligned} \tag{2.8}$$

where the integral over the top of the barrier has been extended from $-\infty$ to ∞

since the contribution of the integrand is not negligible only around q^*. The escape rate from the potential well, *i.e.* the number of trajectories crossing the maximum of the $U(q)$ per unit time and per unit volume, is the inverse of MFPT divided by the total volume of the system V

$$J_{Kr} = \frac{1}{V}\frac{1}{\tau(q)} = \frac{1}{V}\frac{\omega D(q^*)}{\sqrt{2\pi k_B T}}\frac{\exp(-\beta U(q^*))}{\int_{\cup}\exp(-\beta U(y))dy}, \tag{2.9}$$

where

$$P(q^*) = \frac{\exp(-\beta U(q^*))}{\int_{\cup}\exp(-\beta U(y))dy}. \tag{2.10}$$

is the probability density, properly normalized, to find the particle at q^*. Next sections are devoted to specify analytic expressions for the unknown terms in Kramer expression (2.9), in the case of vapor bubble nucleation: the potential $U(y)$ and its curvature ω (Sec. 2.2), and the diffusion coefficient at the top of the barrier (Sec. 2.3).

Here Kramers problem is considered in the overdamped regime. For a discussion of non-overdamped situation the reader is referred to [Hänggi et al., 1990].

2.2 Nucleation rate from Classical Nucleation Theory

Results obtained in previous section can be used to obtain a rough estimation of transition rates for thermally activated processes, such as vapor nucleation within metastable liquids. In order to evaluate bubble nucleation rate from expression (2.9), relevant quantities must be estimated from other theories. The reaction coordinate q for this specific problem can be chosen as the volume of largest bubble in the system V_v. In analogy with Kramers problem, vapor nucleation can be modeled as a diffusive process with a diffusion coefficient $D(V_v)$. The process is driven by a thermodynamical force given by the derivative of the free energy $\Delta\Omega(V_v) = -k_B T \ln P(V_v)$, where $P(V_v)$ is the probability that the largest bubble in the system has volume V_v.

Expression (2.9) can be made more explicit using the CNT profile for the free energy barrier

$$\Delta\Omega(V_v) = \Omega(V_v) - \Omega(0) = \Delta P\, V_v + \gamma_{lv}\left(\frac{3V_v}{4\pi}\right)^{2/3}, \tag{2.11}$$

introduced in Sec. 1.1, where homogeneous nucleation has been discussed. Consistently with CNT quasi equilibrium assumption, the area of the liquid vapor interface is the surface of a sphere of volume V_v. Using Eq. (2.11), the free energy profile maximum is $\Delta\Omega(V_v^*) = 16\pi\gamma_{lv}^3/3\Delta P^2$, while the curvature at the top of the barrier is

$$\omega^2 = \left|\partial^2\Omega(q)/\partial q^2\right|_{V_v=V_v^*} = \frac{\Delta P^2}{\sqrt{32\pi\gamma^3}}. \tag{2.12}$$

Eq. (2.9) become

$$J_{Kr} = \frac{1}{V}\frac{\Delta P^2 D(V_v^*)}{8\pi\sqrt{\gamma^3 k_B T}}\frac{\exp(-16\beta\pi\gamma_{lv}^3/3\Delta P^2)}{\int_\cup \exp(-\beta\Delta\Omega(V_v))dV_v}. \tag{2.13}$$

At this point, an explicit expression for the diffusion coefficient at the top of the barrier is still required. In [Menzl et al., 2016], an approach based on the use of Raileigh-Plesset equation is proposed, whose main points are discussed in the following section.

2.3 Bubble dynamics and diffusion coefficient

Following the work of [Menzl et al., 2016], the analytic expression for the diffusion coefficient $D(V_v^*)$ at the top of the barrier is obtained using the Rayleigh-Plesset (RP) equation, that describes bubble dynamics at the macroscopic level. RP equation is the equation of motion for the volume V_v of a spherical bubble having internal pressure P_v surrounded by a liquid with mass density m, shear viscosity η, pressure P_l, and surface tension γ_{lv}:

$$m\ddot{V}_v - \frac{m\dot{V}_v^2}{6V_v} = 4\pi\left(\frac{3V_v}{4\pi}\right)^{1/3}\left[P_v - P_l - 2\gamma_{lv}\left(\frac{4\pi}{3V_v}\right)^{1/3} - \frac{4\eta}{3}\frac{\dot{V}_v}{V_v}\right]. \tag{2.14}$$

Neglecting inertial terms in left hand-side of Eq. (2.14), RP equation becomes

$$\dot{V}_v = -\frac{3V_v}{4\eta}\left[P_l - P_v + 2\gamma_{lv}\left(\frac{4\pi}{3V_v}\right)^{1/3}\right] = -\frac{1}{\Phi(V_v)}\frac{d\Delta\Omega}{dV_v}. \tag{2.15}$$

Eq. (2.15) describes an overdamped motion over the CNT free energy profile $\Delta\Omega(V_v)$, with friction $\Phi(V_v) = 4\eta/3V_v$. The role of fluctuations, crucial at microscopic scale, can be included in the model by adding a random force $F(t) =$

$\sqrt{2k_BT/\Phi(V_v)}\epsilon(t)$, where $\epsilon(t)$ is white noise and the amplitude factor is evaluated using the fluctuation dissipation theorem. At this stage, the diffusion coefficient can be evaluated using the Einstein relation $D(V_v) = 3k_BTV_v/4\eta$. Inserting the expression for the critical bubble volume $V_v^* = 32\pi\gamma_{lv}^3/3\left|\Delta P^3\right|$, one obtains the diffusion coefficient at the top of the barrier:

$$D(V_v^*) = \frac{8\pi k_BT\gamma_{lv}^3}{\eta\left|\Delta P\right|^3}. \tag{2.16}$$

Once that Eq.(2.16) is inserted in the expression for the nucleation rate (2.13), the only implicit term remains the integral at the bottom of (2.13) that cannot be evaluated explicitly. However, it can be carried out numerically using as the argument of the exponential the free energy profile in units of k_BT.

2.4 The Blander and Katz approach

An alternative approach to evaluate the nucleation rate of bubble within metastable liquids, that is widely used in the literature, is the one derived by Blander and Katz [Blander and Katz, 1975].

The basic assumption to derive Blander and Katz formula is that the number of bubble of volume V_v per unit volume, $n_b(V_v)$, is proportional to the number density of the metastable liquid n:

$$n_b(V_v) = n\exp -\beta\Delta\Omega(V_v) \tag{2.17}$$

This hypothesis is not rigorously justified. However the authors assume that it is reasonable, due to the fact that the error on the prefactor is expected to be order of magnitude less significant than the error in the estimation of the free energy barrier. The last one indeed appears as the argument in the exponential term. Albeit its inaccuracy, the Blander and Katz formula is routinely used due to its simplicity. For homogeneous nucleation the formula is

$$J_{BK}^{hom} = n\sqrt{\frac{2\gamma_{lv}}{\pi m_p}}\exp\left(-\beta\Delta\Omega(V_v^*)\right), \tag{2.18}$$

while for heterogeneous nucleation on a flat surface

$$J_{BK}^{hete} = n^{2/3}\frac{(1-cos(\theta_Y))}{2}\sqrt{\frac{2\gamma_{lv}}{\pi m_p}}\exp\left(-\beta\Delta\Omega(V_v^*)\right), \tag{2.19}$$

where θ_Y is the Young angle (1.4) and m_p is the mass of a fluid particle. The limits of the Kramers and Blander and Katz formulas are addressed in Ch. 5, exploiting as benchmark the results obtained from atomistic simulations and addressing separately the role of the free energy estimation and the kinetic prefactor.

Chapter 3

Simulation methods

The main advantage of using atomistic simulations approach to study vapor nucleation and wetting lies in the fact that it allows to go beyond the limitations and approximation of continuum models. Liquid and vapor are modeled in terms of their fundamental components, *i.e.* atoms or molecules, interacting via a suitable potential. In atomistic simulations, liquid/vapor interface can have a finite thickness and bulk properties of each phase are not assumed to be homogeneous up to the interface. The absence of these assumptions allows to obtain a more realistic description of the phenomena, observing aspects that are not captured by continuum theories.

In this chapter Molecular Dynamics will be introduced in the context of statistical mechanics. Discussing the problem of rare events, two different techniques will be also described: Restrained Hybrid Monte Carlo (RhMC) and Forward Flux Sampling (FFS). The first one is exploited in this thesis to characterize the energetic landscape of the process under investigation, the second one to describe the kinetic mechanism and the properties of the dynamical trajectories.

3.1 The microcanonical ensemble

In statistical mechanics, the macroscopic properties of physical systems are derived in terms of their fundamental components. Macroscopic observables are connected to the microscopic ones, providing a tool to compute relevant physical quantities and derive general thermodynamical laws [Huang, 2009, Tuckerman, 2010].

Let us consider an isolated physical system made of $N \approx 10^{23}$ particles in a volume V. Its state is defined by the canonical coordinates $q_1, q_2, ..., q_{3N}$ and conjugate momenta $p_1, p_2, ..., p_{3N}$ of each particle.

The state of the system can be identified as a point in the $6N$ dimensional phase space and its time evolution as a trajectory in the same space. The time evolution of an isolated system is governed by Hamilton equation:

$$\begin{cases} \dot{q}_i = \frac{\partial H(\mathbf{\Gamma})}{\partial p_i} \\ \dot{p}_i = -\frac{\partial H(\mathbf{\Gamma})}{\partial q_i}. \end{cases} , \tag{3.1}$$

where $\mathbf{\Gamma} = \{q_1, q_2, ..., q_{3N}, p_1, p_2, ..., p_{3N}\}$ and $H(\mathbf{\Gamma})$ is the Hamiltonian of the system.

The trajectory produced by Eq. (3.1) lies on the $6N-1$ dimensional ipersurface, identified by the constraint $H(\mathbf{\Gamma}) = E$, where E is the total energy of the system. If a number of particles of the order of the Avogadro number interact via an highly non linear potential, the numerical resolution of Eq (3.1) is unaffordable, due to the limits of computational resources. Therefore, position and velocity of each single particles cannot be known at each time.

However, since interest is mainly aimed at the macroscopic properties of a physical system rather then at each microscopic details, the notion of Gibbs ensemble has been introduced. An ensemble is a collection of replica of the same system which have in common the value of a set of macroscopic observables. Each ensemble is defined by the probability density function (PDF) in the phase space.

The PDF $\rho(\mathbf{\Gamma}, t)$ is such that $\rho(\mathbf{\Gamma}, t)d^{6N}\Gamma$ is the probability that, at time t, the system is found in the small volume $d^{6N}\Gamma$ around point $\mathbf{\Gamma}$. From this definition, it follows that

$$\rho(\mathbf{\Gamma}, t) \geq 0 \tag{3.2a}$$

$$\int \rho(\mathbf{\Gamma}, t)d^{6N}\Gamma = 1. \tag{3.2b}$$

If the PDF of the ensemble is known, macroscopic observables $O(t)$ can be evaluated as the expectation values defined over the phase space $\hat{O}(\mathbf{\Gamma})$:

$$O(t) = \langle \hat{O} \rangle_t = \int \hat{O}(\mathbf{\Gamma})\rho(\mathbf{\Gamma}, t)d^{6N}\Gamma. \tag{3.3}$$

Since microcanonical ensemble is a collection of systems evolving with the same energy, from Eq. (3.2b) we deduce that a conserved quantity exists. Starting from this observation, Liouville equation for the time evolution of phase space density can be derived [Tuckerman, 2010]:

$$\frac{\partial}{\partial t}\rho(\mathbf{\Gamma},t) + \{\rho(\mathbf{\Gamma},t), H(\mathbf{\Gamma},t)\} = 0. \tag{3.4}$$

where symbol $\{\cdot,\cdot\}$ indicates the Poisson brackets. At equilibrium, the Hamiltonian and the phase space PDF do not depend explicitly on time. Therefore $\partial\rho/\partial t = 0$ and equation (3.4) reduces to:

$$\{\rho(\mathbf{\Gamma}), H(\mathbf{\Gamma})\} = 0, \tag{3.5}$$

for which the general stationary solution is a function that depend on p and q uniquely via the system Hamiltonian

$$\rho(\mathbf{\Gamma}) = \frac{\rho'(H(\mathbf{\Gamma}))}{Z}, \tag{3.6}$$

where Z, the partition function, is the normalization defined as

$$Z = \int \rho'(H(\mathbf{\Gamma}))d^{6N}\Gamma \tag{3.7}$$

The PDF $\rho(\mathbf{\Gamma})$ has non zero values only where the macroscopic conditions of the specific ensemble are satisfied.

A generic isolated system is described by microcanonical ensemble. It has N particles, volume V and energy between E and $E + \Delta E$. Assuming that all the accessible states have the same probability to be visited, $\rho(\mathbf{\Gamma})$ is such that:

$$\rho(\mathbf{\Gamma}) = \begin{cases} cost & se\ \ E < H(\mathbf{\Gamma}) < E + \Delta \\ 0 & otherwise. \end{cases} \tag{3.8}$$

The concept of ensemble can be extended to several thermodynamical conditions. At equilibrium, system coupled with thermostat, barostat or particles reservoirs can be studied defining other equilibrium ensembles.

For example, a system at constant temperature, number of particles and volume is described by the PDF of the canonical ensemble:

$$\rho_c(\mathbf{\Gamma}) = \frac{\exp(-\beta H(\mathbf{\Gamma}))}{Z_c(N,V,T)} \tag{3.9}$$

where $\beta = 1/k_B T$ is the inverse of temperature in units of the Boltzmann constant k_B, and $Z_c(N,V,T)$ is the canonical partition function.

Coupling the system with a barostat and a thermostat produces the PDF of the isobaric isothermal ensemble in which pressure, temperature and number of particles

are constant:

$$\rho_i(\mathbf{\Gamma}) = \frac{\exp(-\beta PV)\exp(-\beta H(\mathbf{\Gamma}))}{Z_i(N,P,T)}. \tag{3.10}$$

where and $Z_i(N,P,T)$ is the partition function of isothermal isobaric ensemble.

Once that the ensemble concept has been introduced, the next step is to define the connection of the statistical theory with thermodynamics and the physical observables. For microcanonical ensemble, the relation that connects the entropy function of state to the volume of the phase space accessible to the system is:

$$S(E,V,N) \equiv k_B log Z(E,V,N), \tag{3.11}$$

where k_B is the Boltzmann constant and $Z(E,V,N)$ is the partition function of microcanonical ensemble:

$$Z(E) \equiv \int_{E<H(\mathbf{\Gamma})<E+\Delta} d^{6N}\Gamma. \tag{3.12}$$

From the entropy expression it is possible to derive all the quantities of physical interest, using Maxwell relation:

$$\frac{1}{T} = \left(\frac{\partial S}{\partial E}\right)_{N,V} \qquad \frac{P}{T} = \left(\frac{\partial S}{\partial V}\right)_{N,E} \qquad \frac{\mu}{T} = -\left(\frac{\partial S}{\partial N}\right)_{V,E}. \tag{3.13}$$

Analogous relation can be obtained for the other ensembles [Huang, 2009].

3.2 Brief overview on Classical Molecular Dynamics

The discussion of previous section has shown that macroscopic properties of physical systems can be evaluated as ensemble average of functions defined over phase space. Let us consider the trajectory of a system, obtained solving (3.1), that visits in an infinite time all the accessible points in the phase space with a frequency proportional to the PDF. A system of this type satisfies the ergodic hypothesis, according with the ensemble average is equivalent to a time average over a trajectory of infinite length:

$$< \hat{O} >= \int d^{6N}\Gamma \hat{O}(\mathbf{\Gamma})\rho(\mathbf{\Gamma}) = \lim_{T\to\infty} \frac{1}{T}\int_0^T dt \hat{O}(\mathbf{\Gamma}(t)) \equiv \overline{\hat{O}}, \tag{3.14}$$

The trajectory of an ergodic system can be interpreted as a sampling of the ensemble PDF. Macroscopic properties can be evaluated as time averages over the

trajectory obtained integrating the equation of motion. This concept is at the basis of Equilibrium Molecular Dynamics. The procedure consists in selecting a representative sampling of the elements that constitutes the system, modeling the interaction among these elements and integrating numerically the equation of motion with appropriate algorithms.

The equation of motion in the Hamiltonian form are the starting point to reconstruct the trajectory in phase space. When canonical coordinates coincide with the positions of the particles, *i.e.*

$$(q_1, q_2, q_3, ..., q_{3N-2}, q_{3N-1}, q_{3_N}) = (r_{1x}, r_{1y}, r_{1z}, ..., r_{Nx}, r_{Ny}, r_{Nz})$$

and

$$(p_1, p_2, p_3, ..., p_{3N-2}, p_{3N-1}, p_{3_N}) = (p_{1x}, p_{1y}, p_{1z}, ..., p_{Nx}, p_{Ny}, p_{Nz}),$$

Eq. (3.1) can be written as:

$$\begin{cases} \dot{\mathbf{r}}_i = \dfrac{\mathbf{p}_i}{m_i} \\ \dot{\mathbf{p}}_i = \mathbf{F}_i(\mathbf{r}_1, ..., \mathbf{r}_N). \end{cases} \tag{3.15}$$

A good integration scheme for (3.15) should be time reversible and preserve the conserved quantities of the dynamics. Velocity verlet algorithm satisfies this requirements for the microcanonical ensemble:

$$\mathbf{r}_i(t+h) = \mathbf{r}_i(t) + \frac{\mathbf{p}_i(t)}{m_i}h + \frac{1}{2}\frac{\mathbf{F}_i(\mathbf{r}(t))}{m_i}h^2 \tag{3.16a}$$

$$\mathbf{p}_i(t+h) = \mathbf{p}_i(t) + \frac{1}{2}(\mathbf{F}_i(\mathbf{r}(t)) + \mathbf{F}_i(\mathbf{r}(t+h)))\,h. \tag{3.16b}$$

The equations of motion (3.15) can be extended in order to simulate systems at constant pressure and/or temperature. The integration algorithms of these extended equations are widely employed since they better describe experimental conditions. Typically, additional degrees of freedom are introduced in order to mimic the effect of barostat and thermostat. For a more detailed discussion of this topic, the reader is referred to [Tuckerman, 2010]. Once that the appropriate algorithm has been chosen, thermodynamical quantities can be evaluated by averaging over the trajectories suitable observables defined over the phase space.

The following relations, that can be obtained by applying the generalized equipartition theorem, define the global pressure P and temperature T.

$$P =< \hat{P} >= \frac{1}{3V} \left\langle \sum_{i=1}^{N} \frac{\mathbf{p}_i^2}{2m} + \sum_{i<j} \mathbf{r}_{ij}\mathbf{F}_{ij} \right\rangle \tag{3.17}$$

$$T =< \hat{T} >= \frac{1}{3Nk_B} \left\langle \sum_{i=1}^{N} \frac{\mathbf{p}_i^2}{2m_i} \right\rangle . \tag{3.18}$$

3.3 Rare events

The brute force integration of classical equations of motion (3.1) for a system made of thousand of particles can be typically carried out for a time interval of the order of microseconds. Sometimes the processes under investigation are transitions between metastable states, *i.e.* minima in the free energy surface. If the energy required to switch from one metastable state to another is significantly higher than the thermal energy k_BT available to the system, transitions would occur infrequently and, possibly, on timescales not accessible to MD. In such conditions, the system is expected to have a persistent motion around one of the minima, preventing a complete sampling of the phase space. This kind of process is usually referred to as an activated event.

Several methods have been developed to cope with rare events. These are aimed at addressing typical question such as the identification of the mestastable states, the mechanism of the transition from one state to another, and the evaluation of the transition rate. In the following sections two different rare events methods are discussed. The first is Restrained Monte Carlo, used in this work to characterize the free energy landscape of bubble nucleation within a metastable liquid. The advantage of this technique is that it can be used also with non analytic collective variables, *i.e.* non analytic function of particles coordinates. The second technique here discussed is the Forward Flux Sampling (FFS). Here FFS has been used to evaluate transition rate and characterize the kinetic mechanisms of heterogeneous nucleation and wetting of nano-structured surfaces. FFS, which allows to obtain an ensemble of reactive trajectories, allows to identify dynamical effects that are missing in quasi-equilibrium methods such as Restrained Monte Carlo.

3.3.1 Collective variables

Rare events can be described with fewer degrees of freedom with respect to the $6N$ phase space variables. Observables that are function of atomistic coordinates can be defined, that are usually called collective variables or, sometimes, reaction

coordinate or order parameter. In the following a generic collective variable function of the atomic coordinates $\mathbf{r} = (r_{1x}, r_{1y}, r_{1z}, ..., r_{Nx}, r_{Ny}, r_{Nz})$ is indicated as $\epsilon(\mathbf{r})$. Depending on the specific problem, one can define ad hoc collective variables that are able to monitor the progress of the transition. When a collective variable is used, the PDF in the phase space $\rho(\mathbf{\Gamma})$ can be replaced with the PDF that the collective variable assumes a specific value z:

$$P(z) = \int \rho(\mathbf{\Gamma})\delta(\epsilon(\mathbf{r}) - z)d\mathbf{\Gamma}. \tag{3.19}$$

The probability $P(z)$ is proportional to the number of available states that are compatible with the condition $\epsilon(\mathbf{r}) = z$. Starting from Eq. (3.20), one can define the Landau free energy related to the collective variable

$$F(z) = -k_B T \ln P(z). \tag{3.20}$$

From the free energy profile in Eq. (3.20), the energy barriers in units of $k_B T$ that separates the metastable states, as well as the relative stability of the profile minima can be evaluated. In the study of the Cassie/Wenzel transition in a rectangular groove, whose results are discussed in Ch. 6, the collective variable has been chosen as the number of particles within the pore $\epsilon(\mathbf{r}) = \sum_{i=1}^{N} \chi(\mathbf{r}_i)$ (see Fig. 3.1), where $\chi(\mathbf{r}_i) = 1$ if the position $\mathbf{r}_i$ of the particle i is inside the pore, 0 otherwise. This analytic function of the atomistic variables is not appropriate when vapor nucleation is not localized. In the study of homogeneous nucleation (Ch. 4 and 5), where the inception of vapor phase can occur at any point of the simulation box, a non analytical collective collective variable has been adopted that is able to estimate the volume of the largest vapor bubble within the liquid bulk. One of the procedure that can be used to evaluate this collective variable is the M-method developed by [González et al., 2014].

The M-method consists of four different steps. Particles are classified as liquid-like if they have more than five particles within 1.6 σ, and vapor-like otherwise. A grid is defined over the simulation box, to partition it into cells that contains at most one particles. A cell is labeled liquid or vapor if it contains a liquid-like or vapor-like particle. Empty cells are classified analysing both the first and second neighbors cells. If the number of nearest neighbor face-sharing empty/vapor cells is 7 or more also the number of second nearest neighbor face-sharing empty/vapor is evaluated. If also the number of these cells is 7 or more, the original empty cell is labeled as vapor. Once this procedure is carried out assigning each cell to vapor or liquid, a

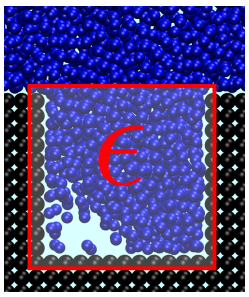

Figure 3.1: Schematic representation of the collective variable used to study the mechanism of the Cassie/Wenzel transition. ϵ is the number of particle within the volume of the pore.

cluster analysis is performed on the vapor cells and the size of the largest bubble is established as the total volume of largest cluster of interconnected cells, i.e. cells sharing a face or a corner. The istantaneous shapes of a growing bubble obtained with the M-method are shown in Fig. 3.2.

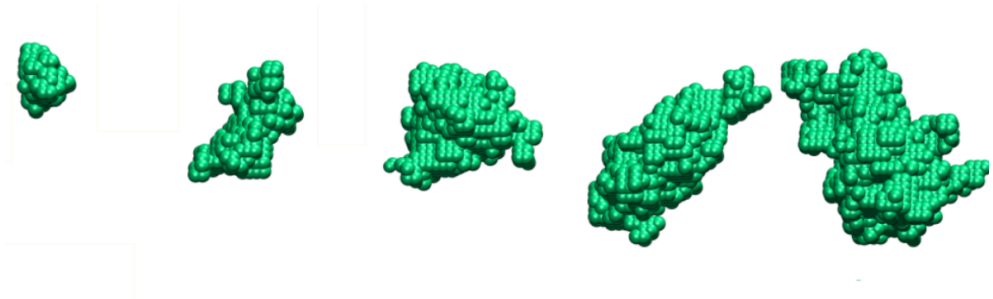

Figure 3.2: Instantaneous shapes of a vapor bubble at different volumes. The points are the cells of the grid assigned to the largest vapor domain in the system.

3.3.2 Sampling free energy landscape: Restrained Hybrid Monte Carlo

The energetic landscape of homogeneous vapor nucleation has been characterized in this thesis using the Restrained hybrid Monte Carlo (RhMC) approach, developed in Refs. [Ciccotti and Meloni, 2011, Elena et al., 2013]. This method allows to use non-analytical collective variables and we use it in conjuction with the volume of the largest vapor bubble in the system.

Standard Monte Carlo (MC) method that produces the sampling of *e.g.* isothermal isobaric ensemble consists in alternating particles and volume moves. A single particle is randomly selected and displaced. The move is accepted or rejected according to the Metropolis criterion. Then, a volume move is performed with a random (isotropic) expansion/compression obtained, in practice, rescaling particles positions. The volume move is accepted or rejected on the basis of the energy and PV values before and after the move. A complete discussion of standard Monte Carlo method can be found in Ref. [Frenkel and Smit, 2001].

The conventional approach of MC in which a single particle is subjected to a random displacement is highly inefficient in our simulations of homogeneous nucleation. The order parameter, computed via the expensive procedure of the M-method described in previous section, must be evaluated at each step. The efficiency can be increased using the hybrid Monte Carlo (hMC) approach in which, at each timestep, the displacement of a single atom is replaced by a collective displacement of the entire system according to a short MD trajectory.

In the first step, a short NVE MD simulation is integrated, starting from current positions and extracting momenta from a Maxwell-Boltzmann distribution at the relevant temperature. The global move is accepted with probability

$$\alpha_{acc} = \min\{1, \exp[-\beta[H' - H]\}, \tag{3.21}$$

where H' and H are the *extended* Hamiltonian of the system before and after the move, respectively. The extended Hamiltonian is the sum of kinetic, $K(\boldsymbol{p})$, and (physical) potential energy, $U(\boldsymbol{r})$, plus a biasing potential energy term which forces the system to visit configurations in which V_V fluctuates around the target value V_V^*: $H(\boldsymbol{p}, \boldsymbol{r}; V_V^*) = K(\boldsymbol{p}) + U(\boldsymbol{r}) + k/2(V_V(\boldsymbol{r}) - V_V^*)^2$; k is the coupling constant determining the degree of fluctuations allowed to the volume of the bubble. The value of k is tuned in order to have an acceptance ratio of $\sim 30\%$. The second MC step consists in a change of the volume of the system. The volume move is accepted/rejected according to the probability:

$$\alpha_{acc} = \min\{1, \exp[-\beta[(H' + PV') - (H + PV)] + N \ln(V'/V)\}, \tag{3.22}$$

where H' and H, V' and V are the *extended* Hamiltonian and volume of the system before and after the move, P is the target pressure and N is the number of particles.

Differently from standard MC, the acceptance criterion takes into account also

the initial and final kinetic energy. In the hMC the Hamiltonian which generates the MD dynamics could be different from the one adopted in the acceptance test [Duane et al., 1987,Mehlig et al., 1992]. Since the dependence on $\mathbf{r}$ in $V_V(\mathbf{r})$ is non-analytical, here we choose to use the physical potential $U(\mathbf{r})$ to generate the dynamics and the restrained potential $U^k(\mathbf{r}) = k/2(V_V(\boldsymbol{r}) - V_V^*)^2$ for the MC acceptance.

The restrained potential allows to sample configurations consistent with the presence of a bubble with a given volume and compute the free energy barriers of nucleation [Ciccotti and Meloni, 2011, Elena et al., 2013]. Following Ref. [Bonella et al., 2012], it is possible to show how the free energy can be reconstructed from restrained simulations. Consider the average

$$\begin{aligned} f^k(z) &= -\frac{\int d\mathbf{r}\, k(V_V(\mathbf{r}) - V_V^*) \exp\left[-\beta U^k(\mathbf{r}, V_V^*)\right]}{\mathcal{Z}^k(V_V^*)} \\ &= -\nabla_{V_V^*}\beta \ln\left(\frac{\mathcal{Z}^k(V_V^*)}{\mathcal{Z}}\right) \end{aligned} \tag{3.23}$$

where $\mathcal{Z}^k(V_V^*) \equiv \int d\mathbf{r} \exp\left[-\beta U^k(\mathbf{r}, V_V^*)\right]$ and $\mathcal{Z} = \int d\mathbf{r} \exp\left[-\beta U(\mathbf{r})\right]$ is the canonical partition function. Since $\mathcal{Z}$ is independent of V_V^*, it was introduced in the second equality in (3.23) in order to interpret $f^k(V_V^*)$ as derivative of $F_k(V_V^*) = -\beta \ln\left(\mathcal{Z}^k(V_V^*)/\mathcal{Z}\right)$. Noting that $\lim_{k\to\infty} \exp[-\beta k/2(V_v(\mathbf{r}) - V_V^*)^2]/(2\pi/\beta k)^{1/2} = \delta(V_V(\mathbf{r}) - V_V^*)$. In this limit we have $f^k(V_V^*) = \nabla_{V_V^*} F_k(V_V^*) \to -\beta^{-1}\nabla_{V_V^*} \ln P_{V_V}(V_V^*)$. Here $P_{V_V}(V_V^*) = \int d\mathbf{r}\delta(V_V(\mathbf{r}) - V_V^*) \exp[-\beta V(\mathbf{r})]/\mathcal{Z}$ is the probability that $V_V(\mathbf{r}) = V_V^*$. Recalling that the Landau free energy of a variable is defined as $F(V_V^*) = -\beta^{-1} \ln P_{V_V}(V_V^*)$, we find that in the proper limit Eq. (3.23) is an estimate of the derivative of the free energy $\nabla_{V_V^*} F(V_V^*)$. The mean force (3.23) can be estimated using hRMC and the relative free energy via integration.

3.3.3 Sampling reactive trajectories: Forward Flux Sampling

Quasi equilibrium techniques such as RhMC, presented in previous section, estimate free energy profiles as functions of suitable order parameters, that monitor the state of progress in the transition. However, dynamical properties cannot be addressed since only conditional equilibrium configurations are explored in simulations.

In order to get informations on the kinetic mechanism of nucleation and wetting, that is the main aim of this thesis work, a versatile technique, the Forward Flux Sampling (FFS) [Allen et al., 2009] has been adopted. Such technique estimates the rate of the transition from one metastable state to another, sampling a large

number of reactive paths. This sampling allows to identify the kinetic mechanism of the process, *e.g.* the physical conditions that may trigger the transition. Moreover, dynamical reactive trajectories include “inertial" effects in the transition, i.e., the fact that a path may be preferred because of inertia along the reaction coordinate.

FFS technique consists in dividing the activated event in a suitable number of “interfaces" and evolving short atomistic trajectories between any two interfaces (Fig. 3.3). In other words, instead of waiting for an extremely improbable event to happen, FFS divides the same event in intermediate steps that are individually accessible by MD. Unrestrained equation of motion are integrated, differently from standard quasi-static methods which use a fictitious term in the potential energy in order to force the sampling of improbable region in the phase space.

The implementation of FFS method generates an ensemble of reactive trajectories from region A, corresponding to the state where the system is initialized, to region B, in which the energetic barrier has been overcome (see Fig. 3.3). The progress of the transition is monitored by defining an order parameter λ. In the study of bubble nucleation λ may correspond to e.g. the volume of the largest bubble in the system [González et al., 2014], while for wetting and recovery transition an appropriate choice could be the number of liquid particles witin a surface groove.

A set of n consecutive, non-intersecting interfaces is defined to partition the region in the phase space between reactants and products. Such interfaces correspond to different values of the order parameter. FFS uses such partitioning of phase space to drive the system along the transition, that otherwise would happen on time scales hardly accessible via brute force MD simulations.

The algorithm can outlined in two main steps and can be implemented in three different variants: Direct FFS, branched growth, and "Rosenbluth like". The first step of the algorithm, common to the three variants, is the evaluation of the flux Φ_0 of a MD trajectory initialized in the basin A, *i.e.* the initial state, at the first interface that limits the “reactant” region.

The second step consists in the calculation, for each of the remaining interfaces, of the conditional probabilities $p(\lambda_{i+1}|\lambda_i)$ of reaching an interface λ_{i+1} starting from the previous interface λ_i. The total rate k_{AB} of the transition is finally evaluated using the product of the flux across the first interface and the conditional probabilities collected for each interface:

$$k_{AB} = \Phi_0 \prod_{i=0}^{n-1} p(\lambda_{i+1}|\lambda_i). \tag{3.24}$$

The difference among the three versions of FFS consists in the procedure used to generate trials trajectories at the interfaces. The three algorithms are schematized below.

Direct method

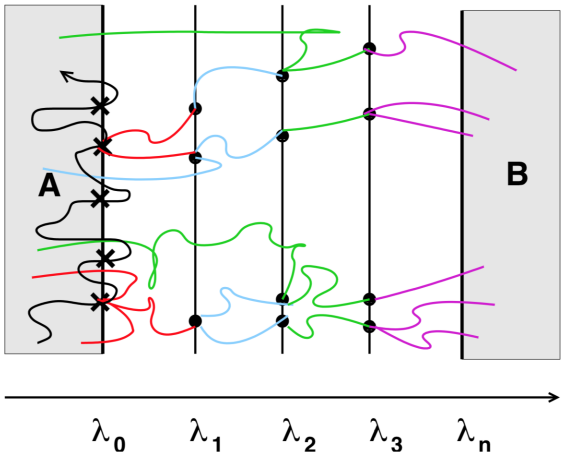

Figure 3.3: Schematic representation of Direct FFS algorithm. Region A (initial state) and region B (final state) are divided by a set of non intersecting interfaces. M_i trials are integrated from interface i, starting from randomly chosen configurations at λ_i. Different colors refers to different interfaces from which trials are started. [Allen et al., 2009]

The procedure of direct FFS is illustrated in Fig. 3.3.

1. Integration of a single long MD trajectory in the pure liquid region. The flux Φ_0 is computed as the number of positive crossing of the first interface N_0 normalized by the total duration of the trajectory.

2. One configuration corresponding to the cross of the first interface is selected at random. A trial run is integrated from this starting point until it reaches the subsequent interface or return in A. In case of success the end point is stored. After repeating the procedure M_0 times, compute $p(\lambda_1|\lambda_0)$ as the fraction of successful trials.

3. Repeat previous step using the collection of points collected at λ_1 and firing M_1 trials. Collect successful configurations at λ_2 and compute $p(\lambda_2|\lambda_1)$.

4. Repeat until λ_n is reached.

Branched growth

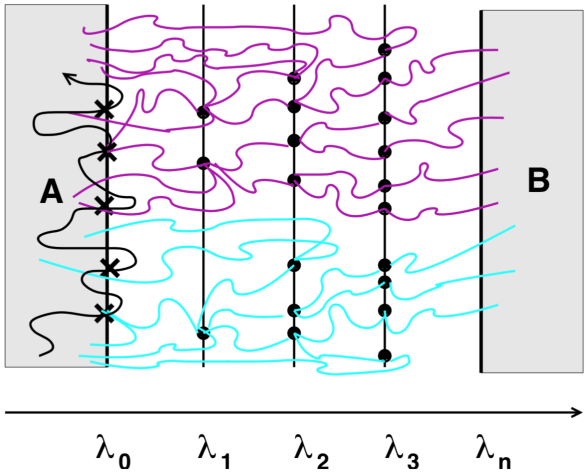

Figure 3.4: Schematic representation of branched growth FFS algorithm. From each points at λ_i, k_i trials are fired. Colors denote different branched paths. [Allen et al., 2009]

The procedure of branched growth method is illustrated in Fig. 3.4.

1. Integration of a single long MD trajectory in the pure liquid region. The flux Φ_0 is computed as the number of positive crossing of the first interface N_0 normalized by the total duration of the trajectory.

2. From the first configuration collected at λ_0 integrate k_0 trials until they reach λ_1 or return in the A basin.

3. From each configuration collected at λ_1 start k_1 trials until they reach λ_2 or return in the A basin.

4. Repeat until λ_n is reached. Compute $p(\lambda_{i+1}|\lambda_i)$ as the number of trials to reach B, divided by the total number of trials $\prod_{i=0}^{n-1} k_i$.

5. Repeat the previous steps for each configuration collected at λ_0.

Rosenbluth like

The procedure of Rosenbluth like method is illustrated in Fig. 3.5.

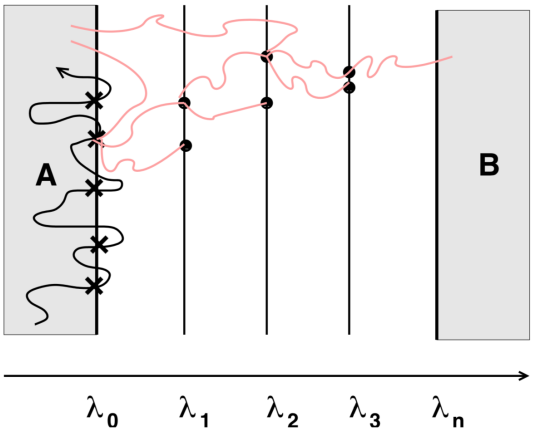

Figure 3.5: Schematic representation of Rosenbluth FFS algorithm. Unbranched transition paths are generated one at time by firing k_i trials from one of the end points collected at λ_i. [Allen et al., 2009]

1. Integration of a single long MD trajectory in the pure liquid region. The flux Φ_0 is computed as the number of positive crossing of the first interface N_0 normalized by the total duration of the trajectory.

2. From the first configuration collected at λ_0 integrate k_0 trials until they reach λ_1 or return in the A basin. Store the successful end points.

3. Choose at random only one of the successful end points and fire k_1 trials from it until they reach λ_2 or return in A.

4. Repeat until interface λ_n is reached.

5. Repeat previous step for each configuration collected at λ_0.

6. Compute $p(\lambda_{i+1}|\lambda_i)$ with the following weighted average:

$$p(\lambda_{i+1}|\lambda_i) = \frac{\sum_b w_{i,b} S_{i,b}/k_i}{\sum_b w_{i,b}} \tag{3.25}$$

where the index b indicates a specific path from A to a configuration at λ_i, $S_{i,b}$ is the number of successful trials fired from that configuration to λ_{i+1}, and

$$w_{i,b} = \prod_{j=0}^{i-1} S_{j,b}/k_j. \tag{3.26}$$

3.3.4 Estimation of nucleation barrier from forward and backward dynamical trajectories

The dynamical trajectories obtained from the FFS method can be exploited to evaluate the stationary probability distribution $\rho(q)$ of a generic parameter q, which can or not coincide with the order parameter used to place the interfaces. The free energy as a function of q is $\Delta\Omega(q) = k_B T \ln \rho(q)$. The combined estimation of the nucleation rate and the free energy barrier allows to evaluate the kinetic prefactor Γ_0, using the Eyring relation $k = \Gamma_0 exp(-\Delta\Omega/k_B T)$. The procedure here employed to evaluate the free energy barrier from FFS data is the one described in [Valeriani et al., 2007].

The stationary distribution $\rho(q)$ is such that the $\rho(q)dq$ is the probability of finding the order parameter q is between q and $q + dq$, for a system which is in the stationary state. $\rho(q)$ can be obtained using the statistical data provided by the reactive and unreactive FFS trajectories starting from the n interfaces. In order to get the stationary distribution of the variable q, both trajectories coming from reactant (region A) and product (region B) must be taken in to account. Thus FFS must be performed forward $A \to B$ and backward $B \to A$ (see Fig. 3.6). Splitting the two contributions $\rho(q)$ can be written as

$$\rho(q) = \Psi(A) + \Psi(B), \tag{3.27}$$

where $\Psi(A)$ and $\Psi(B)$ are the densities produced by the trajectories coming from reactant and product, respectively.

The function $\Psi(A)$ is given by

$$\Psi(A) = p_A \Phi_{0A} \tau_+(q; \lambda_0). \tag{3.28}$$

In the above expression p_A is the probability that the system is in A, Φ_{0A} is the flux of trajectories across the interface which delimits A, and $\tau_+(q; \lambda_0)$ is the average time spent at the value q of the order parameter by a trajectory that starts from A.

The same holds for the contribution coming from trajectories starting from products region

$$\Psi(B) = p_B \Phi_{0B} \tau_-(q; \lambda_n), \tag{3.29}$$

where $\tau_-(q; \lambda_n)$ is the contribution of the trajectories starting from λ_n, in the $B \to A$ reverse FFS procedure. The probabilities p_A and p_B can be obtained from the $A \to B$

and $B \to A$ nucleation rate, observing that in a stationary state $p_A k_{AB} = p_A k_{BA}$. Moreover neglecting the intermediate states, in virtue of the fact that the time scales typical of the permanence in A and B are much larger than the timescale of the transition, it is also true that $p_A + p_B = 1$. Thus

$$p(A) = \frac{k_{BA}/k_{AB}}{1 + k_{BA}/k_{AB}} \tag{3.30}$$

and $p(B) = 1 - p(A)$. The fluxes Φ_{0A} and Φ_{0B} are evaluated in the FFS forward and backward calculation as the number of crossing of the first interface divided by the time of the unrestrained trajectory. The function $\tau_+(q;\lambda_0)$ can be evaluated in terms of the contributions given by the trials trajectories started from each of the n interfaces. Defining as $\pi_+(q,\lambda_i)$ the average time spent at q for a FFS trial run started at λ_i, $\tau_+(q;\lambda_0)$ is given by

$$\tau_+(q;\lambda_0) = \pi_+(q,\lambda_0) + \sum_{i=1}^{n-1} \pi_+(q,\lambda_i) \prod_{j=0}^{i-1} P(\lambda_{j+1}|\lambda_j), \tag{3.31}$$

where the probability of each state q is properly reweighted using the conditional probabilities, in order to correct for the enhanced sampling of FFS at the intermediate states between A and B. Analogously the expression for $\tau_-(q;\lambda_0)$ is given by

$$\tau_-(q;\lambda_n) = \pi_-(q,\lambda_n) + \sum_{i=n-1}^{1} \pi_-(q,\lambda_i) \prod_{j=n}^{i+1} P(\lambda_{j-1}|\lambda_j), \tag{3.32}$$

computed from the trajectories of the reverse FFS implementation. The functions $\pi_/ + -(q,\lambda_i)$ are discretized as follows:

$$\pi_{+/-}(q,\lambda_i) = \frac{N_q}{\Delta q M_i}, \tag{3.33}$$

where N_q is the number of times that along the M_i trials fired from λ_i the order parameter is between q and $q+\Delta q$. N_q is given by $N_q = \Delta t \sum_{k=0}^{M_i} \sum_{s=0}^{n_k} h_q$ where Δt is the timestep width, n_k is the number of timestep of the k-th trial, and h_q is unity if during the timestep the order parameter is between q and $q + \Delta q$, zero otherwise.

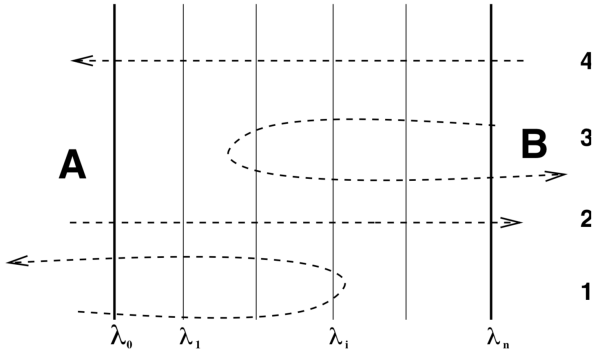

Figure 3.6: Illustration of categories of trajectories that contribute to $\rho(q)$. Trajectories 1 and 2 are generated with an FFS simulation from A to B. Trajectories 3 and 4 are generated with an FFS simulation from B to A. [Allen et al., 2009]

Part II

Results and discussions

Chapter 4

Pressure control in interfacial systems: atomistic simulation of vapor nucleation

4.1 Introduction

Atomistic simulations are routinely used to investigate a variety of multiphase nanoscale systems, such as bubbles, drops, solid walls in contact with fluids, solutions, etc. In order to reproduce experimentally relevant conditions in small simulation samples far from the thermodynamic limit, barostats are often needed to control the pressure.

The principle inspiring many barostats used in molecular dynamics (MD) is to generate the correct equilibrium distribution for the isothermal-isobaric or isoenthalpic-isobaric ensemble evolving an extended system of equations for the generalized degrees of freedom connected to the particles and simulation box. The *force* driving the expansion or compression of the system is the imbalance between the current instantaneous pressure, which depends on the positions and momenta of *all* particles, and the target pressure. Also the dynamics of the particles is affected by the imbalance between the present and target pressure *via* the coupling with the simulation box degrees of freedom [Andersen, 1980, Parrinello and Rahman, 1981, Melchionna et al., 1993, Martyna et al., 1994]. Because the instantaneous pressure depends on all particles, in the following we will refer to this class of barostats as global barostats. *Global barostats* are also used in Monte Carlo simulations. In this case one typically alternates particles and volume moves. [Panagiotopoulos, 1987] The volume move is accepted or rejected depending on the *instantaneous enthalpy* ($H + PV$, H is the

Hamiltonian, P target pressure and V volume of the sample) of the system before and after the move.

Pressure control is relevant also for the simulation of a variety of multi-phase systems, which is beyond the original scope of the global barostats. What sets these systems apart is that different subdomains can have different pressures. A broad range of phenomena falls into this class, including homogeneous and heterogeneous vapor nucleation, [Shen and Debenedetti, 1999, Wang et al., 2008, Meadley and Escobedo, 2012, Sharma and Debenedetti, 2012, Giacomello et al., 2012a, Giacomello et al., 2015, Giacomello et al., 2013] nucleation of polymorphic crystals, [Sloan Jr, 2003, Lauricella et al., 2014, Lauricella et al., 2015, Lauricella et al., 2017] dissolution of bubbles and droplets, condensation or evaporation, etc. Below we show that in these cases, in which the relative amount of the two phases changes along the process, when one uses global barostats the pressure of the preexisting bulk metastable phase might change during the process, which is different from the condition at which experiments are carried out.

Here, in order to appraise these effects, we consider the case of vapor nucleation from a homogeneous metastable liquid. We present a simple macroscopic theory based on the sharp-interface model explaining the behavior of global barostats and their effects on nucleation. Atomistic simulations are performed for a Lennard-Jones liquid in the same nominal thermodynamic conditions as those available in the literature [Wang et al., 2008, Meadley and Escobedo, 2012] (both references use global barostats). A hybrid restrained Monte Carlo scheme [Ciccotti and Meloni, 2011, Elena et al., 2013] is adopted in order to cope with the problem of rare events [Bonella et al., 2012] typical of nucleation and in order to compute the free energy profile of nucleation; the volume of the largest bubble is used as the order parameter [González et al., 2014]. The good agreement between macro- and microscopic results suggests that the intuitive argument of domains at different pressures is, indeed, at the origin of the artifacts associated to global barostats.

A solution to these artifacts proposed, which consists in using a *local* barostat that imposes the (local) force balance between a piston and the contacting liquid. Simulations are run using the local barostat showing that, at variance with global barostats, the local barostat is able to maintain the liquid pressure constant at the target value all along the process.

The manuscript is organized as follows. A macroscopic, sharp-interface model is introduced in Sec. 4.2. In the same section a microscopic formulation of the problem is presented. It is shown that within the sharp-interface limit the two representations

are consistent. In Sec. 4.3.1, the simulation campaign is described in detail, while in Sec. 4.3.2 we validate the local barostat for homogeneous systems. In Secs. 4.3.3 and 4.3.4 the results are discussed. The last section is left for conclusions.

4.2 Theoretical analysis of continuum and atomistic models of a two-phase liquid/vapor system

We focus on the homogeneous nucleation of a vapor bubble in a metastable liquid. This deceptively simple case allows us to analyze the shortcomings of standard barostats in dealing with multiphase systems at different pressures. The same arguments should also apply to a variety of other multiphase systems, including heterogeneous vapor nucleation and condensation.

We start by introducing a simple continuum model of vapor nucleation – the sharp-interface – and the associated classical nucleation theory, CNT. [Kelton and Greer, 2010] This model is based on a number of approximations, including the fact that the interface is ideally sharp, that are sometimes violated in actual systems. Nevertheless, within these approximations, it allows us to obtain an explicit dependence of the liquid pressure and of the energetics of the process on the volume of the vapor bubble, which helps understanding the shortcomings of standard (global) barostats. In the results section, we will illustrate that, even when the sharp-interface model approximations are violated, e.g., when the system is relatively close to the critical point, this theory captures the qualitative trend of the data.

In the sharp-interface model it is assumed that the bulk properties of the fluids are valid up to the interface, where a sharp change in these properties occurs. The liquid and vapor domains are assumed to be uniform and isotropic. In particular, the diagonal terms of the stress tensor are all equal and the off-diagonal terms are zero. In correspondence of the (infinitesimal) interface these conditions are no longer met and the tangential and normal components of the stress tensor to the surface are different. [Rowlinson and Widom, 2013] Within the sharp-interface model this imbalance is translated into a surface tension γ acting at the dividing surface, which has an indirect influence on the liquid and vapor pressures *via* the (extended) Laplace equation. [Giacomello et al., 2012a] In such a system, the average pressure of the whole sample reads:

$$P = \frac{1}{V}\int_V P(\mathbf{x})\,\mathrm{d}\mathbf{x} = P_L\frac{V_L}{V} + P_V\frac{V_V}{V} = P_L(1-\chi_V) + P_V\chi_V \tag{4.1}$$

where, consistently with the sharp-interface model, we assumed that the pressure field is of the form $P(\mathbf{x}) = P_L\theta_L(\mathbf{x}) + P_V\theta_V(\mathbf{x})$, with $\theta_V(\cdot)$ and $\theta_L(\cdot) = 1 - \theta_V(\cdot)$ characteristic functions of the liquid and vapor domains, respectively.[1] The interfacial terms do not contribute directly to the average pressure because the interface is sharp, i.e. of it has an infinitesimal volume. V_L and V_V are the volumes of the liquid and vapor phases, respectively, $V = V_L + V_V$ is the total volume, and $\chi_V = V_V/V$ and $\chi_L = V_L/V$ are the vapor and liquid volume fractions. An atomistic justification of Eq. (4.1) is given below. Equation (4.1) can be used to quantify the variation of the liquid pressure during an isothermal and isobaric bubble nucleation event. A closed set of equations for evaluating the liquid pressure can be obtained adding the extended Laplace law introduced in Ref. [Giacomello et al., 2012a] or, if one is only interested in the liquid pressure at the critical nucleus, its conventional form valid for extremal points of the free energy. Here we use a simpler empirical approach: we assume that P_V is constant and equal to the vapor tension at the simulated temperature; this approximation is then validated by atomistic simulations.

Conventional barostats used in atomistic simulations [Andersen, 1980, Parrinello and Rahman, 1981, Martyna et al., 1994], which have been designed for homogeneous systems, control the average pressure of the sample, P. Thus, within the sharp-interface model, the pressure of the liquid in a sample containing one vapor bubble of volume V_V is:

$$P_L(V_V) = P\frac{1}{(1-\chi_V)} - P_V\frac{\chi_V}{(1-\chi_V)} \tag{4.2}$$

where the dependence of the various terms on the volume of the bubble is made explicit. Since vapor nucleation occurs when $P_V > P_L$, Eq. (4.2) shows that the actual liquid pressure decreases along nucleation and that the driving force of the process, $\Delta P = P_V - P_L = (P_V - P)/(1 - \chi_V)$, grows along it instead of remaining constant as it happens in actual experiments.

Equation (4.2) can be used in conjunction with the CNT of vapor formation to quantify the effect of conventional barostats on the free-energy profile of the process in a finite-size system. In CNT, where it is assumed that the pressure of the liquid is constant along the process (P_L^0), the free energy difference between the liquid containing a bubble of volume V_V and the reference bulk liquid reads [Kelton and Greer, 2010]:

[1] The characteristic function is equal to 1 if $\mathbf{x}$ is within its domain of reference, liquid or vapor in the present case, and 0 otherwise.

$$\begin{aligned}\Delta G^0(V_V) &= N_v[\mu_V(P_L^0) - \mu_L(P_L^0)] + \gamma A \\ &\simeq (P_L^0 - P_V)V_V + \gamma A\end{aligned} \tag{4.3}$$

where N_v is the number of vapor atoms in the bubble, $\mu_V(P_L^0)$ and $\mu_L(P_L^0)$ are the chemical potential of the vapor and liquid phase at P_L^0, respectively, γ is the surface tension, and A is the area of the liquid/vapor interface. The second equality in Eq. (4.3) follows from a first order expansion of chemical potentials around the vapor tension P_V. γ is assumed to be the planar surface tension of the two phases at coexistence. Assuming that the liquid is incompressible and that, as said above, P_V is constant and equal to the vapor tension, the free energy profile at variable liquid pressure is:

$$\Delta G(V_V) = V_V \left[P_L(V_V) - P_L^0\right] + \Delta G^0(V_V) \tag{4.4}$$

We remark that, owing to the many assumptions of CNT, Eq. (4.4) does not necessarily describe in quantitative terms atomistic results, but it is certainly useful to explain what are the potential artifacts connected with the use of conventional barostats on the free energy profile. In Sec. 4.3.1, atomistic simulations implementing various methods for controlling the pressure will be used to quantify these effects on the free-energy profile and nucleation barrier.

Since $\left[P_L(V_V) - P_L^0\right] < 0$ (Eq. (4.2)), the effect of conventional barostats is that of reducing the barrier (Eq. (4.4)) as compared to the case of constant liquid pressure (Eq. (4.3)). In Figure 4.1, we report both the free-energy barrier $\Delta G^0(V_V)$ according to Eq. (4.3) (black line) and the free-energy barrier $\Delta G(V_V)$ according to Eq. (4.4) (red and blue lines for systems of 7000 and 13500 particles, respectively).

In Eqs. (4.3) and (4.4) the free energy is computed setting $P_L^0 = 0.026$, $P_V = 0.046$ and $\gamma = 0.098$ for the reference liquid pressure, vapor tension and surface tension at $T = 0.855$. [Wang et al., 2008] (Lennard-Jones units are used throughout the article: temperature, pressure, length and time are reported in reduced units, ϵ/k_B, $\epsilon/\ \sigma^3$, σ, and $\sigma(m/\epsilon)^{1/2}$, respectively). The liquid volume is assumed to be constant during nucleation and consistent with the bulk density of atomistic systems of $N = 7000$ and 13500 particles: $V_L = N/\rho_L$, where $\rho_L = 0.58$ is the metastable liquid density at the current pressure and temperature of simulations. Given the difference between the liquid and vapor density ($\rho_V = 0.08$), this approximation does not sizably affect the free energy. Global barostat free energy profiles are

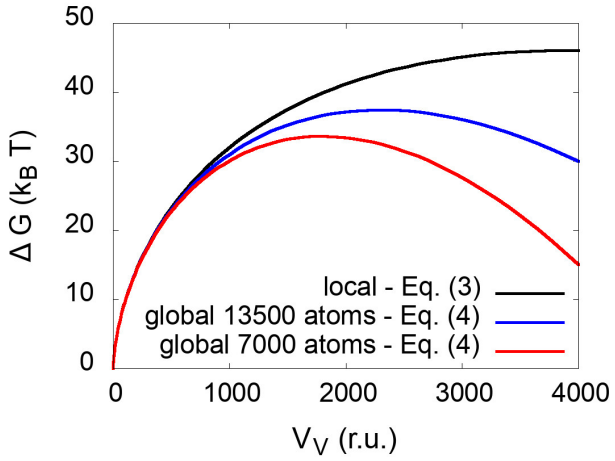

Figure 4.1: Free-energy profiles for homogeneous bubble nucleation with the sharp-interface model for a sample in which one controls the liquid (Eq. (4.3) black line) or total sample pressure (Eq. (4.4) blue and red lines for samples of 13500 and 7000 particles, respectively).

shown in Fig. 4.1 and compared with CNT results. This comparison shows that the free energy profiles with 7000 and 13500 are below the CNT one; in particular the nucleation barrier $\Delta G^\dagger$, the difference between the maximum and initial free energy, follows the trend $\Delta G^\dagger_{7000} < \Delta G^\dagger_{13500} < \Delta G^\dagger_{CNT}$. Indeed, this is consistent with the observation that the driving force ΔP grows along nucleation for global barostats, and its growth is more marked for the smaller sample.

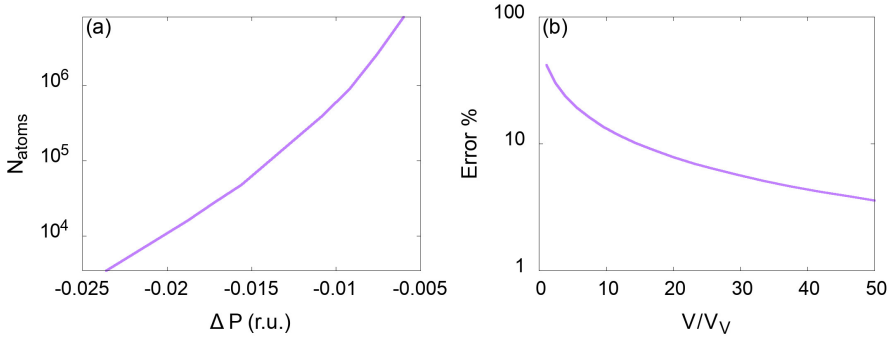

Figure 4.2: (a) Number of particles to have an error of $10\,k_BT$ on the nucleation barrier evaluated via the continuum theory (Eq. (4.4)). (b) Percent error on the barrier as a function of the volume ratio $V/V_V^\dagger$ of the simulation box and the critical bubble $V_V^\dagger$.

In order to extend these results to more general systems, it is worth estimating the error affecting the free energy barrier as a function of the size of the system and thermodynamic conditions due to the global barostat. Fig. 4.2(a) reports the size of the sample corresponding to an error on the barrier of 10 k_BT as a function of $\Delta P = P_L^0 - P_V$.As expected, the closer the system is to two-phase coexistence ($\Delta P = 0$), the larger is the critical nucleus, the larger must be the sample to keep the error under the prescribed threshold. Our model suggests that in the physical conditions studied in previous [Wang et al., 2008, Meadley and Escobedo, 2012] and in the present work, the atomistic system should contain at least $\geq 10^4$ particles in order to have an error on the free-energy barrier $\leq 10\ k_BT$. Panel b of the same figure presents the percent error on the free-energy barrier as a function of the ratio between the total volume and the volume of the critical bubble, $V/V_V^\dagger$. The continuum sharp-interface model shows that, independently of the thermodynamic conditions, simulation boxes 15 times bigger than the critical bubble are necessary to have errors on the barrier ≤ 10 %.

The microscopic expression for the pressure of an isotropic system consisting of n particles interacting *via* a pair potential is:

$$P = \frac{1}{3V}\sum_{i=1}^{n}\left(\frac{\mathbf{p}_i^2}{m_i} + \frac{1}{2}\sum_{j\neq i}\mathbf{r}_{ij}\cdot\mathbf{f}_{ij}\right) \tag{4.5}$$

where $\mathbf{p}_i$ and m_i are the momentum and the mass of the i-th particle, $\mathbf{f}_{ij}$ is the force between i-th and j-th particles, and $\mathbf{r}_{ij}$ is their (vector) distance. With standard barostats it is the imbalance between the pressure P in Eq. 4.5 and the target pressure that drives the system (see, e.g., Ref. [Martyna et al., 1994]).

If we consider a two-phase system containing n_L bulk liquid, n_V bulk vapor particles, and n_{int} interface particles, we can rewrite Eq. (4.5) as the sum of three terms, associated to the liquid, vapor, and interface domains:

$$P = \frac{1}{3V}\sum_{i=1}^{n_L}\left(\frac{\mathbf{p}_i^2}{m_i} + \frac{1}{2}\sum_{j\neq i}\mathbf{r}_{ij}\cdot\mathbf{f}_{ij}\right) + \frac{1}{3V}\sum_{i=1}^{n_V}\left(\frac{\mathbf{p}_i^2}{m_i} + \frac{1}{2}\sum_{j\neq i}\mathbf{r}_{ij}\cdot\mathbf{f}_{ij}\right) + \frac{1}{3V}\sum_{i=1}^{n_{int}}\left(\frac{\mathbf{p}_i^2}{m_i} + \frac{1}{2}\sum_{j\neq i}\mathbf{r}_{ij}\cdot\mathbf{f}_{ij}\right) \tag{4.6}$$

When the interface is vanishingly small the contribution of the corresponding term is negligible and the pressure of the sample is expressed as the sum of the first

and second term, which, when the liquid and vapor domains are large enough, can be interpreted as the liquid and vapor pressures: [2].

$$P_L \simeq \frac{1}{3V_L}\sum_{i=1}^{n_L}\left(\frac{\mathbf{p}_i^2}{m_i}+\frac{1}{2}\sum_{j\neq i}\mathbf{r}_{ij}\cdot\mathbf{f}_{ij}\right) \tag{4.7}$$

and

$$P_V \simeq \frac{1}{3V_V}\sum_{i=1}^{n_V}\left(\frac{\mathbf{p}_i^2}{m_i}+\frac{1}{2}\sum_{j\neq i}\mathbf{r}_{ij}\cdot\mathbf{f}_{ij}\right), \tag{4.8}$$

Thus, consistently with the macroscopic sharp-interface model in Eq. (4.1), when the interface thickness is negligible, Eq. (4.6) reduces to the volume-weighted average of the liquid and vapor pressure $P \simeq (V_L/V)P_L + (V_P/V)P_V$.

4.3 Numerical simulations

4.3.1 Simulation details

We considered a system composed of particles interacting via the truncated and force shifted (TFS) Lennard-Jones (LJ) potential, analogous to those considered in Refs. [Wang et al., 2008, Meadley and Escobedo, 2012]

$$u_{TFS}(r_{ij}) = u_{LJ}(r_{ij}) - u_{LJ}(r_c) - \left|\frac{du_{LJ}}{dr}\right|_{r_c}(r_{ij}-r_c) \tag{4.9}$$

where

$$u_{LJ}(r_{ij}) = 4\epsilon\left[\left(\frac{\sigma}{r_{ij}}\right)^{12}-\left(\frac{\sigma}{r_{ij}}\right)^{6}\right] \tag{4.10}$$

with $r_c = 2.5$. In the TFS-LJ potential the pair particle forces go to zero smoothly as r goes to r_c. The liquid vapor phase diagram of the TFS-LJ system has been reported in Refs. [Wang et al., 2008] and [Errington et al., 2003].

We compute the vapor nucleation free-energy barrier as a function of the largest vapor bubble in the system, V_V, estimated using the M-method [González et al., 2014]. The method consists of several steps. i) Particles are labeled as liquid-like if they have more than five particles closer than 1.6 σ, and vapor-like otherwise.

[2] We remark that these expressions correspond to the bulk liquid and vapor pressures only in the limit of infinite liquid and vapor domains, respectively. In fact, the inner sum runs over all liquid, vapor and interface particles, and the interaction between particles belonging to different ddomains might be non-negligible for small samples.

ii) The simulation box is partitioned into cells. The size of the cells is chosen such that they can contain at most one particle. A cell is labeled liquid or vapor if it contains a liquid-like or vapor-like particle. Empty cells are classified analysing both the first and second neighbors cells. If the number of nearest neighbor face-sharing empty/vapor cells is 7 or more also the number of second nearest neighbor face-sharing empty/vapor is evaluated. If also the number of these cells is 7 or more, the original empty cell is labeled as vapor. iii) Finally, a cluster analysis is performed on the vapor cells and the size of the largest bubble is established as the total volume of largest cluster of interconnected cells, *i.e.* cells sharing a face or a corner (Fig. 4.3).

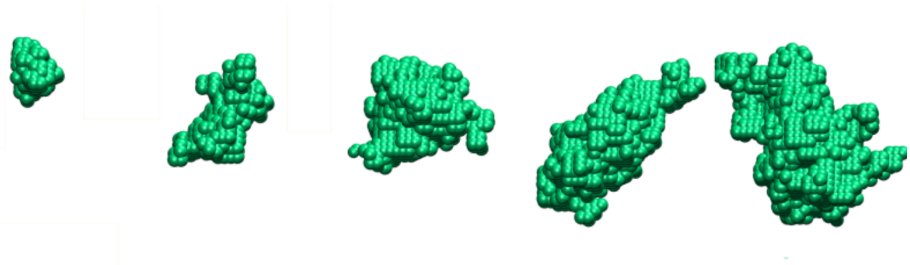

Figure 4.3: Instantaneous bubbles configurations corresponding to increasing bubble's size (from left to right) at $T = 0.855$ and $P_L = 0.026$. The spheres represent the cells of the vapor cluster.

To study vapor nucleation we employ the hybrid Restrained Monte Carlo (hRMC) approach [Ciccotti and Meloni, 2011, Elena et al., 2013, Meloni and Ciccotti, 2015], which is well suited for non-analytical collective variables (CV), such as the size of the largest vapor bubble used here. hRMC allows to sample the conditional probability density function at the current value of the volume of the vapor bubble, and to compute conditional averages. Thus, one can estimate the mean force by the conditional average of the observable $-k(V_V(\boldsymbol{r}) - V_V^*)$, [Maragliano and Vanden-Eijnden, 2006b, Ciccotti and Meloni, 2011] which can be numerically integrated to obtain the free energy profile along the nucleation process. A in-depth explanation of the hRMC method is given in Sec. 3.3.2.

hRMC with a global barostat. A typical MC method for sampling constant pressure ensembles consists in alternating particles and volume moves. Particles moves are accepted or rejected according to the Metropolis criterion, which will be detailed below for the case of hRMC. In volume moves a random (isotropic) expansion/compression is generated and particles positions are rescaled accordingly. The move is accepted or rejected on the basis of the energy and PV values before

and after the move.

In the first step a short NVE MD simulation is integrated, starting from the previous configuration and with momenta extracted from a Maxwell-Boltzmann distribution at the relevant temperature. The acceptance probability is

$$\alpha_{acc} = \min\{1, \exp[-\beta[H' - H]\}, \tag{4.11}$$

where H' and H are the *extended* Hamiltonian of the system before and after the move, respectively. The extended Hamiltonian is the sum of kinetic, $K(\boldsymbol{p})$, and (physical) potential energy, $U(\boldsymbol{r})$, plus a biasing potential energy term which forces the system to visit configurations in which V_V fluctuates around the target value V_V^*: $H(\boldsymbol{p}, \boldsymbol{r}; V_V^*) = K(\boldsymbol{p}) + U(\boldsymbol{r}) + k/2(V_V(\boldsymbol{r}) - V_V^*)^2$; k is the coupling constant determining the degree of fluctuations allowed to the volume of the bubble (see Sec. 3.3.2 for more details). The second MC step consists in a change of the volume of the system. Scaled particles positions do not change in this move. The volume move is accepted/rejected according to the probability:

$$\alpha_{acc} = \min\{1, \exp[-\beta[(H' + PV') - (H + PV)] + N \ln(V'/V)\}, \tag{4.12}$$

where H' and H, V' and V are the *extended* Hamiltonian and volume of the system before and after the move, P is the target pressure and N is the number of particles.

hRMC with the local barostat. To overcome the artifacts due to global barostats we also adopt a local barostat, which consists in enclosing the system between two moving walls of particles to which a constant additional force f is applied (Fig. 4.4(a)). The wall particles interact with the fluid via a suitable potential (here LJ) and, at stationarity, the total force $F = fn_{wall}$ exerted on the liquid by the n_{wall} particles is equal and opposite to that exerted by the fluid particles on the walls, i.e., when the external pressure F/A, with A the area of the walls, is equal to the liquid one P_L. Thus, with the present barostat, stationarity is determined by the (local) balance between the forces of the piston and the liquid in contact with it rather than on the average pressure of the sample, including vapor domains.

In the present work each wall is made of two layers of TFS-LJ atoms (50 times heavier than the fluid ones) in the fcc lattice configuration. The LJ parameters are $\epsilon_{WW} = 10\,\epsilon_{WF}$ and $\epsilon_{FF} = \epsilon_{WF}$ (W = wall, F = fluid). In Fig. 4.4(b) the calibration curve P_L *vs* f is reported for a bulk TFS-LJ liquid; this graph shows that the macroscopic prediction $P_L = fn_W/A$ is fulfilled, confirming the mechanical balance

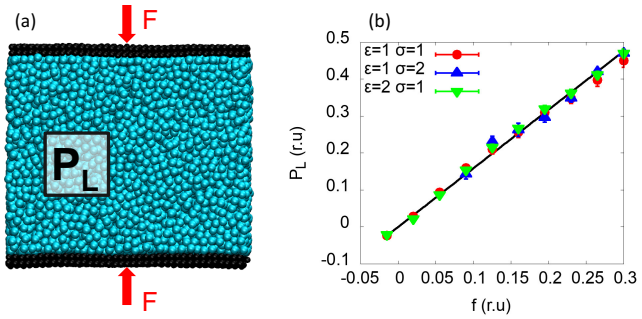

Figure 4.4: (a) Sketch of the local barostat. The solid walls act as pistons: at equilibrium the external force F is balanced by the force exerted on the walls by the liquid pressure P_L. (b) Calibration curve P_L *vs* F for three different solid-liquid LJ interaction parameters ϵ and σ. The solid line is the theoretical prediction $P_L = f n_W / A$.

mechanism by which the local barostat controls the liquid pressure. Fig. 4.4(b) reports data obtained with different values of ϵ_{WF} and σ_{WF} indicating that the local barostat does not sensitively depend on the chosen solid-liquid interaction potential. In other words, the local barostat is rather robust and does not require fine tuning of the solid-liquid interaction.

Other *local barostats* can also be adopted, e.g., that based on a non-interacting particles gas, [Grünwald et al., 2006] but we found the moving walls one to be simpler to use in the presence of a gas phase.

The hRMC simulation protocol used to implement the local barostat is the following. A short MD NVE trajectory of both fluid and solid particles is integrated, initializing particles momenta from a Maxwell-Boltzmann distribution. The boundary conditions are free in the direction orthogonal to the walls and periodic in the other directions. The acceptance probability reads

$$\alpha_{acc} = \min\{1, \exp[-\beta[\tilde{H}' - \tilde{H}]\}, \tag{4.13}$$

In this case the extended Hamiltonian is $\tilde{H}(\boldsymbol{p}, \boldsymbol{r}, V_V^*) = H(\boldsymbol{p}, \boldsymbol{r}; V_V^*) + \sum_{i=1,2\times n_W} f z_i$, where the sum runs over the $2 \times n_W$ particles of the moving walls and z_i is their position in the direction orthogonal to the walls.

Before closing this section, it is worth mentioning that the use of the local barostat

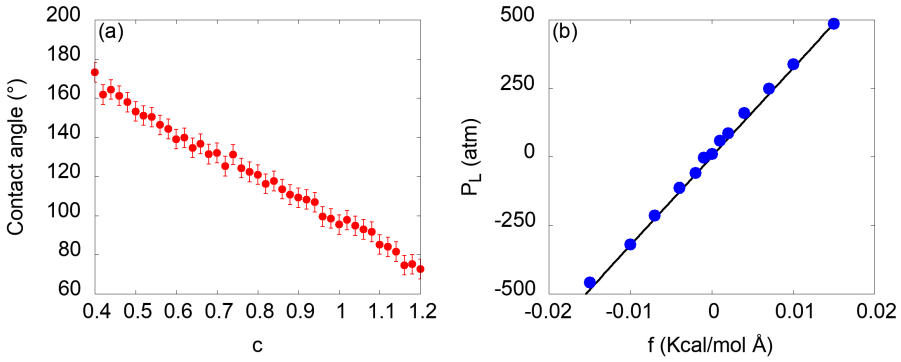

Figure 4.5: Local barostat applied to TIP4P/Ew [Horn et al., 2004] liquid water. (a) Dependence of the Young contact angle on the coefficient c of the modified LJ potential controlling the solid-liquid interaction. The graph shows that acting on this parameter one can tune the hydrophilicity/phobicity over a broad interval. (b) P_L *vs* f calibration curve of the local barostat. The panel shows that the local barostat is able to control the pressure over a range of at least 1000 atm, with both negative and positive values of the pressure. As in the case of the LJ potential, the numerical results are in very good agreement with the theoretical predictions, $P_L = fn_W/A$ (solid line).

is not limited to simple atomic fluids; for example, one can use the local barostat also with molecular fluids such as water. We show this by simulating a small box of TIP4P/Ew [Horn et al., 2004] water with two pistons, in which the wall particles interact with the oxygen atoms of water molecules *via* the modified LJ potential $\tilde{u}_{LJ}(r_{ij}) = 4\epsilon \left[\left(\frac{\sigma}{r_{ij}} \right)^{12} - c \left(\frac{\sigma}{r_{ij}} \right)^{6} \right]$, where c is a parameter that allows one to tune the hydrophilicity/phobicity of the solid (see Fig. 4.5(a) and Ref. [Lisi et al., 2017]). Like in the case of a LJ fluid, the calibration curve of water obeys the force balance relation $P_L = fn_W/A$ (Fig. 4.5(b)).

4.3.2 Validation of the local barostat

We validated the local barostat by comparing results against those obtained with a global one for *bulk* systems. In particular, we focused on the distribution of instantaneous pressures and on the phase diagram (Fig. 4.6). One notices that the instantaneous pressure distribution obtained with the local barostat is, within the error bars, the same as that obtained with the global one. Also the liquid and vapor branches of the TFS-LJ binodal obtained with the local barostat match very well with literature data. [Errington et al., 2003] We also considered the case of more com-

plex molecular fluids, by comparing the liquid branch of the binodal of TIP4P/Ew water obtained by the local and global barostats, and literature data [Vega et al., 2006] (Fig. 4.6(c)). Also in this case there is a very good matching of local barostat results with reference data.

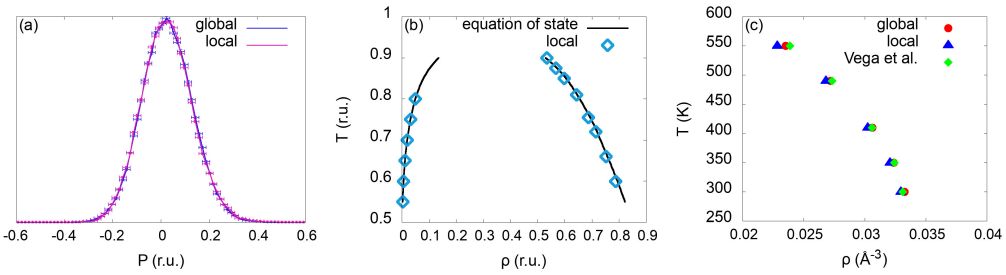

Figure 4.6: (a) Comparison between the distribution of instantaneous pressures of a TFS-LJ bulk liquid system obtained by MTK (global) and local barostat. (b) Liquid and vapor binodal curves for the TFS-LJ potential. The blue points are obtained using the local barostat, black curves are from Ref. [Errington et al., 2003]. (c) Comparison between the liquid branch of the TIP4P/Ew water binodal obtained with the global and local barostats and literature data. [Vega et al., 2006]

4.3.3 Vapor bubble nucleation

Simulations are performed at $T = 0.885$ and $P = 0.026$, *i.e.*, the same conditions used in the literature. [Wang et al., 2008, Meadley and Escobedo, 2012] We considered two computational samples containing 7000 and 13500 particles. These samples are relatively large, in particular, 13500 is larger than those used in the literature [Shen and Debenedetti, 1999, Wang et al., 2008, Meadley and Escobedo, 2012]. For each sample we computed the free-energy profile *vs* the bubble volume with both the global and the local barostats. The mean forces are estimated at a set of 20 V_V^* values of the volume of the largest vapor bubble in the sample (see Sec. 3.3.2 and Refs. [Maragliano and Vanden-Eijnden, 2006b, Ciccotti and Meloni, 2011, Meloni and Ciccotti, 2015]).

As a first remark, we notice that results obtained with the local barostat for the two samples of different size are in good agreement between them (Fig. 4.7) and with the CNT predictions (Fig 4.1). The barrier and critical size are slightly smaller in the atomistic case; this effect is well known (see, e.g., Ref. [Shen and Debenedetti, 1999]) and is associated to the limits of the continuum model, namely to the idealized sharp-interface.

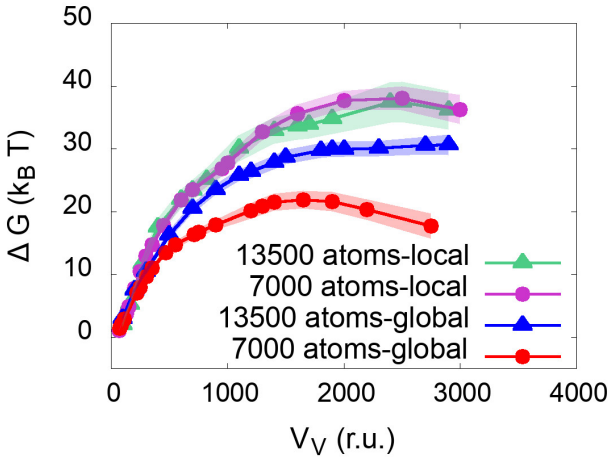

Figure 4.7: Atomistic free-energy profiles for homogeneous bubble nucleation calculated via hRMC simulations.

With the global barostat, the system shows a significant dependence of the free-energy profile on the sample size. In particular, the barriers are $(22 \pm 1)\, k_B T$ and $(30 \pm 1)\, k_B T$ for the small and large samples, respectively, both significantly smaller than the value measured with the local barostat, $(40 \pm 1)\, k_B T$ and $(39 \pm 1)\, k_B T$ for the small and large samples, respectively. These results confirms that, in order to have an accurate prediction of the nucleation barrier, free of finite size effects arising from the pressure control, one has either to simulate very large samples or to resort to a local barostat.

The errors on the free-energy barriers are reflected with exponential sensitivity on the nucleation rates, which are one of the final goals of the simulations of nucleation. Assuming that the nucleation rate follows a CNT-like relation, $k = k_0 \exp(-\Delta G^\dagger / k_B T)$, and assuming that the kinetic prefactor k_0 is not affected by how pressure is controlled, one estimates differences of $4 - 6$ orders of magnitude between the local and global barostats rates, depending on the size of the sample. Even larger errors are expected in the case of fewer particles often used in the older literature.

4.3.4 Effect of the barostat on the properties of the liquid and vapor domains

The sharp-interface model interpretation of the effect of the global barostat on the free energy, discussed in Sec. 4.2, is that the liquid pressure shrinks along vapor nucleation. Here we investigate the variation of the pressure of the liquid domain and other properties of the system as a function of the vapor bubble size with the global and local barostats.

Density. We start by analyzing the dependence of the (conditional ensemble averaged) radial density field, $\rho(r; V_V)$ (r is the distance from the center of the bubble), on the type of barostat. $\rho(r; V_V)$ has been computed for both the 7000 and 13500 particles samples and with both barostats in a radial range encompassing the bubble, interface and liquid domains. We considered samples containing bubbles of several sizes, from very small to supercritical ones. Very small bubbles, $V_V \leq 700$, do not present well defined vapor domains. For bubble larger than this threshold (Fig. 4.8(a) and (b), $V_V = 1500$, to be compared with a critical nucleus of $V_V^\dagger \sim 2500$) the radial density presents the expected profile with bulk vapor and liquid domains separated by an interface. The first observation is that with both barostats and for both samples the interface, the region in which the density changes rapidly from low (vapor) to high (liquid) values, is rather thick, ~ 8. This large value is not surprising considering that simulations are performed at pressure and temperature conditions relatively close to the critical point.

A second observation is that there are important differences between the radial density obtained with the two barostats. With the local barostat the density field of both samples shows two plateaus at small and large r (see insets of Fig. 4.8(a)), corresponding to the vapor and liquid domains, respectively. The density in the bubble is very close to the value corresponding to the vapor tension, which confirms the reliability of the approximation on the value of P_V used in Sec. 4.2. At the other end of the radial range, the density in the bulk liquid reaches the expected value. With the global barostat, on the contrary, in the smaller system the radial density does not seem to reach the vapor and liquid plateaus. In particular, the value of the radial density at the last point is 3.5 % lower than the liquid bulk value at the target pressure and temperature. In the large sample the radial density reaches the target liquid density value but the curve presents a significant slope in this domain, which suggests that it does not correspond to the bulk liquid. This is confirmed by independent NVT simulations performed at the average density of the last four

points of $\rho(r; V_V)$, in which we measured the total vapor fraction, χ_V^{tot}, i.e.,the vapor fraction due all bubbles present in the liquid (Fig. 4.8(c)). Our results show that the system presents two regimes: for densities close to the bulk value, the one measured in the liquid domain of samples containing a small nucleating bubble, χ_V^{tot} is small and constant; for densities corresponding to samples containing larger nucleating bubble χ_V^{tot} is large and grows with V_V, i.e.,with decreasing ρ. [3] This confirms that with the global barostat and in presence of critical bubbles the liquid does not behave as a bulk liquid. Concerning $\rho(r; V_V)$ at small r, in the bubble region the radial density is slightly above the target value.

We believe that the remarkable effect of the global barostat on the density has two main reasons: i) the relatively large compressibility of the LJ liquid and ii) the thick interface at the present thermodynamic conditions. We expect that for less compressible liquids, e.g., water, and at thermodynamic conditions further from the critical point the effect of the global barostat on the density would be smaller. This does not mean that in these cases the barostat-related artifacts on the energetics of nucleation would be smaller, simply it might be more difficult to identify that simulations are performed with an inappropriate setup.

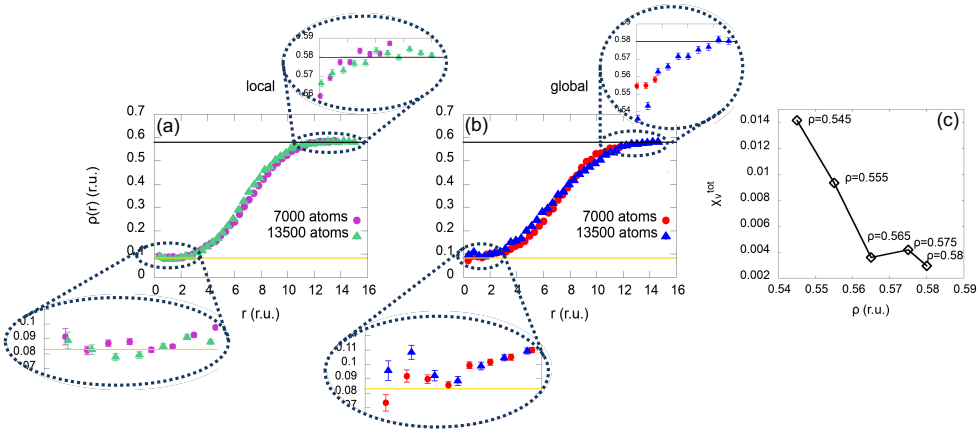

Figure 4.8: Radial density with local (a) and global (b) control of pressure. Data are reported for bubbles of 1000 (being the critical bubble of ~ 2500). The continuum black and yellow lines are the target bulk liquid and vapor densities at coexistence at $T = 0.855$. (c) Fraction of total vapor volume in the NVT simulations at the average pressure of the last 4 radial density points for vapor bubbles of size 300 (leftmost) $< V_V <$ 2300 (rightmost).

[3] In this second regime, spontaneous nucleation is prevented by the constant volume conditions of the simulation.

Liquid pressure. It is important to evaluate the pressure of the liquid domain to validate the assumptions behind the effect of global barostat. In Fig. 4.9 we report the pressure of a liquid control volume far from the vapor bubble and from the solid walls computed via Eq. 4.7 with the prescriptions of Irving and Kirkwood. [Irving and Kirkwood, 1950] These results show the expected decreasing trend of P_L with the bubble size. However, since the sub-domains are small, the large statistical error of the estimated pressure makes it difficult to draw reliable conclusions. This is especially critical in samples containing larger bubbles in which the limited bulk liquid domain imposes to use very small control volumes. Thus, we also follow a different approach, which consists in first determining the mean density in the liquid domain, which converges with the number of hRMC steps faster than the *local pressure*, and then in computing the pressure *via* an independent NVT simulation of a *bulk* liquid with 3000 particles at this density. The density of the bulk sample is set to the average density of the last four points of the radial profile for selected values of the bubble volume (Fig. 4.8(c)). Results show that pressures estimated with both methods are consistent, with lower errors connected with the second one (Fig. 4.9).

Despite the improved statistical accuracy, due to the relatively large scatter of the density (see insets of Fig. 4.8) also for the second approach the overall accuracy on the estimated pressure is limited. Thus, one should focus on the qualitative effects of barostats on the P_L *vs* V_V curves. With the local barostat the liquid pressure is almost constant all along the process and very close to the expected value, typically within the statistical error from the reference pressure (Fig. 4.10). For samples containing larger bubbles one observes a small reduction of this pressure, which is related to the overlap of the bubble with its periodic images that lowers the "liquid" density. On the contrary, in the case of global barostat the pressure significantly decreases with the bubble size. This occurs with both samples but the phenomenon is enhanced in the case of 7000 particles. With the large sample the liquid pressure is initially close to the target value and then deviates for $V_V \geq 1000$.

The dependence of the pressure with the bubble volume and, for a given V_V, with the number of particles in the sample is consistent with the analysis of Sec. 4.2. However, atomistic simulations show a larger deviation from the target pressure than the one predicted by the sharp-interface model. We believe that this is due to two reasons, i) the limited accuracy in the estimate of the pressure *via* the density of the liquid domain[4] and ii) the presence of a very thick interface, which is not taken

[4] a direct measure of the pressure in this domain would not have given more accurate results

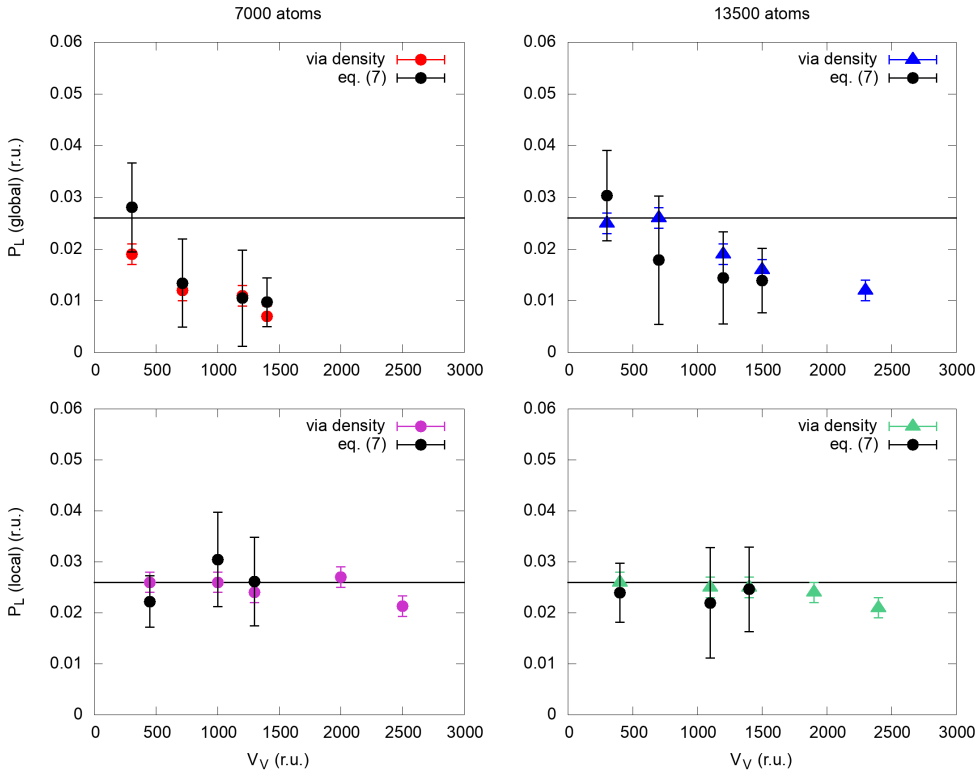

Figure 4.9: Comparison between the pressure computed *via* Eq.(4.7) and *via* an NVT simulation at the density of the bulk liquid domain in a system containing a bubble of volume V_v. The solid black line represents the target value of P_L. These results show that the two approaches are equivalent but the former has a much larger statistical error associated with it.

into account in the sharp-interface model, i.e., that in Eq. 4.1 one discards both a) the continuous change of the normal pressure in going from the liquid to the vapor domain and b) the tangential contribution, which differs from the normal one. Nevertheless, it is remarkable that even in conditions very far from those of Sec. 4.2 the theoretical predictions are in qualitative (pressure) and quantitative (nucleation barrier) agreement with atomistic results.

4.4 Conclusions

In this work we have addressed the issue of controlling pressure in vapor nucleation from a metastable liquid. Our theoretical analysis and numerical simulations show that global barostats result in a underestimation of the liquid pressure, which is

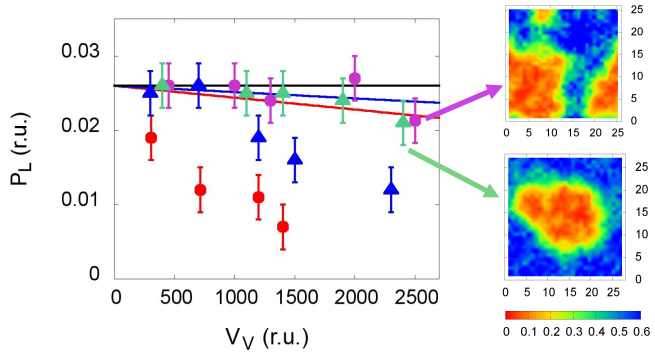

Figure 4.10: Liquid pressure as a function of the bubble size. The red and blue symbols represent the pressure, controlled by a global barostat, for the samples of 7000 and 13500 particles, respectively; purple and green points refer to the pressure for samples controlled by the local barostat. The red and blue lines are the continuum predictions for the liquid pressure (Eq. 4.2). The black line represents the target liquid pressure. In the figure we also report the colormaps of the density field of two snapshots of the samples with 7000 (upper panel) and 13500 (lower panel) particles at $V_V \sim 2500$. These snapshots show that the departure of the pressure from the target value is due to the interaction of the thick interfaces with their periodic images. This problem for bubbles close to the critical size has already been put forward by Meadley and Escobedo [Meadley and Escobedo, 2012] for their simulations on a sample of 10000 particles at the same thermodynamic conditions. When a bubble interacts with its periodic image the radial density in the *liquid* domain (Fig. 4.8) used to compute the pressure, is reduced and the pressure decreases.

particularly severe for large ΔP. In turn, this can bring to artifacts on the driving force and, ultimately, on the free energy of the process.

According to our analysis based on the sharp-interface model, in order to have an error on the nucleation barrier $\leq 10\%$ in a simulation in which the global pressure is set equal to a target value, the simulation box volume should be around 15 times bigger than the critical bubble volume.

To confirm the theoretical predictions, we have performed hRMC simulations aimed at computing the free-energy profile along the nucleation pathway. Atomistic data show a qualitative agreement with the theoretical predictions.

Our results suggest that simulations using standard barostats [Shen and Debenedetti,

1999, Wang et al., 2008, Meadley and Escobedo, 2012, Menzl et al., 2016], if not performed on a reasonably large system size, might be affected by errors of the order of $10-15\ k_BT$ on the barrier height, corresponding to an error of $10^4-10^6\ s^{-1}\sigma^{-3}$ on the rate.

Finite-size effects associated with pressure control can be eliminated by replacing conventional, global, barostats, developed for single-phase systems, with a local barostat, which controls the pressure of the liquid phase. This can be achieved by adding moving solid walls interacting with the liquid via, e.g., a Lennard-Jones potential. The walls, to which is applied an external force, act as pistons compressing the liquid at the desired pressure all along the nucleation process and make it possible to perform constant liquid pressure simulations even with small simulations boxes (e.g., 7000 particles in for the present system).

To conclude, to have an accurate prediction of the nucleation barrier, free of finite size effects arising from the pressure control, one has either to simulate significantly larger samples or to resort to the local barostat.

Chapter 5

Dynamical effects in homogeneous vapor bubble nucleation

5.1 Introduction

Homogeneous bubble nucleation consists in the formation of vapor cavities within the bulk of a metastable liquid. The mechanism and rate governing the inception of nucleation events has been the subject of debate in the recent literature. The results obtained by [Wang et al., 2008] demonstrated the contribution of temperature (local) fluctuations at the initial stage of bubble expansion. In particular, a positive correlation between vapor nucleation inception and the presence of local hot spots has been identified in a superheated liquid at conditions near the critical point of the phase diagram. However, this result has been challenged by brute force MD simulations performed in very large samples at several thermodynamic conditions [Diemand et al., 2014]. The inconsistency between these results suggests that further investigations are required to establish a clear picture of the phenomenon. In particular, the analysis of the "dynamical" properties of the process would be crucial to obtain insights on the mechanism by which the inception of the new phase takes place. In fact, often bubble nucleation rate is determined by combining free energy calculation or even more parametric approaches (Classical Nucleation Theory -CNT- with liquid tension and difference between liquid and vapor pressure as only input data) with empirical for the exponential prefactor in Arrenius-like equations.

The objective of this work is two-fold: to determine how kinetic effects that are not taken into account in standard approaches i) affect the accuracy of the nucleation rate by "standard" formula and ii) what is their influence on the phase transition

mechanism. Depending on the thermodynamic conditions and, as a consequence, on the transition time we will use either *brute force* molecular dynamics or the forward flux sampling, an advanced simulation technique that allows to sample the ensemble of reactive trajectories.

Different thermodynamic conditions are investigated. The first one corresponds to a superheated liquid near the critical point in which bubble nucleation is an activated event hindered by a relatively high free energy barrier ($\Delta G \sim 40 k_B T$). This point has been widely investigated in previous work [Wang et al., 2008, Meadley and Escobedo, 2012]. We also considered milder conditions, closer to that at which phase transition experiments are typically carried out. In these cases the nucleation barrier is often small, of the order of few $k_B T$ ($\sim 5\ k_B T$). In particular, we considered negative and positive liquid pressures, mimicking cavitation and boiling conditions, respectively, both of interest for technological applications.

5.2 Theory

Bulk vapor nucleation is a process often characterized by a large free energy barrier separating the metastable (liquid) from the stable (vapor) state. When such a barrier is significantly larger than the thermal energy available to the system ($k_B T$, with k_B the Boltzman constant and T the temperature) the transition from the liquid to the vapor state is slow: the system can remain trapped in the initial state for a time largely exceeding the one accessible by atomistic simulations. In these cases, special simulation techniques are used to investigate the nucleation process. To the best of our knowledge, four types of approaches have been used to investigate vapor nucleation: extended *brute force* molecular dynamics (MD), [Diemand et al., 2014] quasi-static rare event techniques (umbrella sampling, [Torrie and Valleau, 1977, Shen and Debenedetti, 1999], restrained hybrid Monte Carlo - hRMC, [Ciccotti and Meloni, 2011, Elena et al., 2013, Marchio et al., 2018] boxed dynamics - BXD [Glowacki et al., 2009, Meadley and Escobedo, 2012]), classical nucleation theory with parameters determined from simulations ([Espinosa et al., 2016, Menzl et al., 2016]), dynamical rare event methods (forward flux sampling, [Allen et al., 2006c, Wang et al., 2008, Meadley and Escobedo, 2012] transition interface sampling [van Erp et al., 2003, Menzl et al., 2016]). Each of these approaches has advantages and disadvantages; for example, *brute force* MD introduces no bias on the results but its application is limited to spinodal conditions otherwise the transition time would be too long for current and foreseeable computers. Umbrella sampling, hybrid

restrained hRMC and BXD strongly depend on the choice of the collective variable for describing nucleation [Amabili et al., 2017]. CNT requires the determination of the difference of chemical potential of the two phases and, especially, the surface tension of the liquid, which depends on the size of the bubble. Moreover, despite recent progresses, its extension to heterogeneous and confined systems is non-trivial. [Giacomello et al., 2012a, Giacomello et al., 2015, Giacomello et al., 2013]

Kramers theory In the Kramers theory it is assumed that the system moves diffusively in the free energy profile $U(q)$, with q reaction coordinate of the problem. [Kramers, 1940, Hänggi et al., 1990] Here q is the volume of the largest vapor bubble, V_V, as discussed in detail below. Within this theory, the rate at which bubbles nucleate in a metastable liquid is

$$J_{Kr} = \frac{1}{V}\left[\left(\int_{\cup} \exp\left[-\beta U(V_V)\right] dV_V\right)\left(\int_{\cap} \exp\left[\beta U(V_V)\right]/D(V_V) dV_V\right)\right]^{-1} \tag{5.1}$$

where $\beta = 1/k_B T$, $D(q)$ is the diffusion coefficient, and the symbols $\int_{\cup} \cdot$ and $\int_{\cap} \cdot$ indicate that the integration is carried out in the well of the initial metastable state and at the top of the barrier, respectively. Assuming that $D(V_V)$ is a smooth function of V_V, and that $U(V_V)$ quickly decreases when the system moves out of the *transition state* V_V^*, the maximum of $U(V_V)$ separating the initial and final states, the second integral can be solved using the Laplace method, thus obtaining the following form for the nucleation rate

$$J_{Kr} = \frac{\omega D}{V\sqrt{2\pi k_B T}} \frac{\exp(-\beta \Delta U(V_V^*))}{\int_{\cup} \exp\left(-\beta \Delta U(V_V)\right) dV_V} \tag{5.2}$$

where $\omega = \sqrt{d^2 U(V_V)/dV_V^2|_{V_V = V_V^*}}$ is the square root of the curvature of the free energy at the top of the barrier and $\Delta U(V_V) = U(V_V) - U(0)$, with $U(0)$ free energy of the bulk liquid.

One possibility is to determine the unknown data of Eq. 5.2 in the context of the CNT, which prescribes that $\Delta U(V_V) = U(V_V) - U(0)$ is the reversible work of formation of a spherical bubble of volume V_V from a bulk liquid in a *sharp interface* description of the multiphase system: [Kelton and Greer, 2010]

$$\Delta U(V_V) = (P_L - P_V)V_V + 4\pi\gamma\left(\frac{3V_V}{4\pi}\right)^{2/3}, \tag{5.3}$$

where P_L and P_V are the liquid and vapor pressure, respectively, γ is the liquid/vapor surface tension. Eq. (5.3) allows to determine the barrier height $\Delta U(V_V^*) = 16\pi\gamma^3/3(P_L - P_V)^2$ and the curvature of the free energy at the transition state, $\omega = (P_L - P_V)^2/\sqrt{32\pi\gamma^3}$. The integral over the barrier well can be evaluated numerically from the profile by setting the lower limit of the integral to 0 and the upper limit to $\bar{V}_V$ such that $\Delta U(\bar{V}_V) = k_B T$. Finally, the diffusion coefficient at the top of the barrier can be obtained following the derivation of Menzl et al. [Menzl et al., 2016], in which the Rayleigh-Plesset equation is used to express D in terms of the macrosopic properties of the liquid: $D = 8\pi k_B T\gamma^3/\eta|P_L - P_V|^3$, where η is the viscosity of the system.

If the free energy profile is obtained from quasi-static rare events methods, such as hRMC, one can determine the barrier, curvature and integral in the bulk liquid basin by numerically (see below).

Blander-Katz theory An expression for the kinetic prefactor largely used in the literature, alternative to (5.2), is derived in the work of Blander and Katz [Blander and Katz, 1975]. According to the Blander and Katz model of the kinetics of the nucleation process, bubble nucleation rate can be evaluated with the following expression

$$J_{BK} = n_L \left[\frac{2\gamma}{\pi m B}\right] \exp\left(-\Delta G(V_V^*)/k_B T\right), \tag{5.4}$$

where n_L is the number density of the liquid, m is the mass of a fluid particle, and $B \sim 1 - 1/3(1 - P_L/P_V)$ is an adimensional factor. Due to its simplicity, expression (5.4) is routinely used [Wang et al., 2008, Meadley and Escobedo, 2012, Diemand et al., 2014, Baidakov and Bobrov, 2014], albeit some of the hypothesis behind its derivation have no rigorous justification.

The accuracy of the theories above reported will be addressed in the results section, by performing a direct comparison with the atomistic simulation results. In particular, we will investigate how the two quasi-static models shortly described above cope with kinetic (non-equilibrium) effects, and if the possible discrepancies must be ascribed to the free energy barrier or exponential prefactor. In Sec. 5.4.1 we compare the barrier $\Delta G(V_V^*)$ obtained from FFS/brute force MD, restrained hybrid MC (quasi-static) and CNT barrier. The kinetic prefactor of the atomistic nucleation rate is obtained by inverting the Eyring equation

$$J = \Gamma_0 \exp(-\Delta G(V_V^*)/k_B T), \tag{5.5}$$

where J and $\Delta G(V_V^*)$ are determined by suitable independent procedure [Allen et al., 2009, Wedekind and Reguera, 2008]. The numerical Γ_0 will be compared with that obtained from Eqs. (5.2) and (5.4). In 5.4.2 we investigate the nucleation mechanism. In particular, we will determine a set of suitable properties along reactive and non reactive trajectories. This will allow us to assess the reliability of quasi-static assumption in CNT. The details of the atomistic simulation of bubble nucleation here performed are discussed in the following section.

5.3 Simulation details

We simulate a set of 7098 atoms interacting via a truncated and force shifted (TFS) Lennard Jones (LJ) potential:

$$u_{TFS}(r_{ij}) = u_{LJ}(r_{ij}) - u_{LJ}(r_c) - \left|\frac{du_{LJ}}{dr}\right|_{r_c} (r_{ij} - r_c) \tag{5.6}$$

where

$$u_{LJ}(r_{ij}) = 4\epsilon \left[\left(\frac{\sigma}{r_{ij}}\right)^{12} - \left(\frac{\sigma}{r_{ij}}\right)^{6}\right] \tag{5.7}$$

with $r_c = 2.5$. In the TFS-LJ potential the pair particle forces go to zero smoothly as r goes to r_c. Lennard-Jones units are used throughout the article: temperature, pressure, length and time are reported in reduced units, ϵ/k_B, ϵ/σ^3, σ, and $\sigma(m/\epsilon)^{1/2}$, respectively. The size of the sample is chosen about twice the one in [Wang et al., 2008], large enough to contain a critical nucleus and avoid finite size effects.

LJ fluid is simulated at four different thermodynamic points, corresponding to the following values of temperature and pressure: $P = 0.026$ $T = 0.855$, $P = -0.04$ $T = 0.81$, $P = 0.01$ $T = 0.855$, and $P = 0.001$ $T = 0.845$.

The value of temperature is controlled using the Nosè-Hoover thermostat [Evans and Holian, 1985] with a relaxation time of $\tau_T = 0.093$, the same as [Wang et al., 2008]. The pressure of the system is enforced using a mechanical barostat [Marchio et al., 2018]. In practice the liquid is confined along z direction between two walls parallel to the xy plane. The upper wall can translate along z. On the atoms of upper wall acts an extra force that globally sums up to:

$$f \equiv \frac{F}{N_{wall}} = \frac{P \cdot A}{N_{wall}} \tag{5.8}$$

where F is the overall force acting on the wall, N_{wall} is the number of the wall atoms, P is the imposed pressure, and A is the surface area of the wall.

In those conditions in which we use FFS, we employ the volume of the largest bubble V_V in the system as order parameter. In order to detect it and estimate its volume we employ the M-method [González et al., 2014]. The method can be summarized in the following steps. i) Particles are labeled as liquid-like if they have more than five particles closer than 1.6σ, and vapor-like otherwise. ii) The simulation box is partitioned into cells of a size such that they can contain at most one particle; each cell is labeled liquid or vapor depending on the particles of either type occupying the cell. A cell is vapor like if it is surrounded by a sufficient number of empty cells. Empty cells are classified analysing both the first and second neighbors cells. If the number of nearest neighbor face-sharing empty/vapor cells is 7 or more also the number of second nearest neighbor face-sharing empty/vapor is evaluated. If also the number of these cells is 7 or more, the original empty cell is labeled as vapor. iii) Finally, a cluster analysis is performed on the vapor cells and the size of the largest bubble is established as the total volume of largest cluster of interconnected cells, i.e. cells sharing a face or a corner.

At the first thermodynamic condition ($T = 0.855$, $P = 0.026$), nucleation is hindered by a relatively high energy barrier which prevents nucleation on the brute force MD timescale. In order to tackle the issue of rare events, preserving the dynamical properties of nucleation mechanism, Molecular Dynamics simulations are combined with FFS rare event method, see Sec. 3.3.3, implemented in its direct version [Allen et al., 2009]. The interfaces are placed at following values of the order parameter V_V = 60, 90,120, 150, 210, 280, 350, 450, 550, 700, 820, 950, 1200, 1500, 2000, 2500, 3000. The value of the order parameter along the MD trajectories is evaluated each 5 steps of amplitude $\Delta t = 0.002$. At each interface a set of 576 trials is fired. Each of them is integrated until it reaches the following interface or returns in the metastable liquid basin. The method is implemented also backwards from the last to the first interface, see Sec. 3.3.4, in order to obtain a stationary probability distribution of the order parameter, which is exploited to evaluate the nucleation free energy barriers.

The three remaining thermodynamic conditions are simulated via a brute force integration of the equation of motion. To evaluate nucleation rates and free energy barriers, the approach presented in [Wedekind and Reguera, 2008] has been adopted.

More specifically, nucleation rate is obtained as the inverse of the mean first passage time (MFPT) at the transition state, *i.e.* the average time that the system needs to nucleate a critical bubble starting from the pure liquid. At the same time, the calculation of the stationary probability distribution of the bubble volume within the liquid allows the estimation of the free energy profile.

5.4 Results

5.4.1 Kinetic and energetic contributions to nucleation rate

FFS Nucleation rate The nucleation rate for the TFS-LJ liquid at $T = 0.855$ and $P = 0.026$ is evaluated using FFS method described in Sec. 3.3.3. In Fig. 5.1(a) we report the committor probability P_B. The committor function $P_B(x)$ is defined as the probability that a trajectory initiated from configuration x will reach the final state before the initial state.

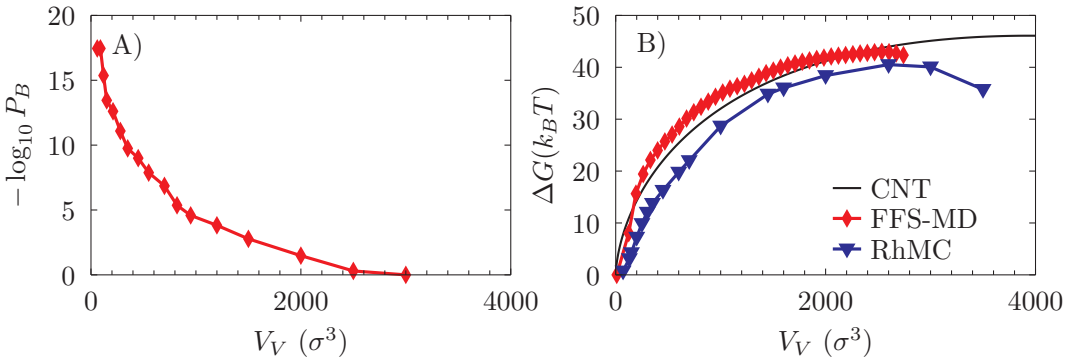

Figure 5.1: (a) Committor probability as a function of the largest vapor bubble in the system. (b) Red points are the free energy barrier estimated via the statistical analysis of forward and backward trajectories described in Sec. 3.3.4. Black line is the CNT barrier (5.3). Blue points are the free energy profiles obtained with the quasi static method RhMC in [Marchio et al., 2018].

The committor P_B is evaluated using the FFS conditional probabilities at the n interfaces λ (see Sec. 3.3.3) as

$$P_B(\lambda_j) = \prod_{i=j}^{n-1} P(\lambda_{i+1}|\lambda_i) \tag{5.9}$$

where the interfaces positions corresponds to the values of V_V listed in Sec. 5.3. The value of the order parameter at which the committor equals 0.5 corresponds to

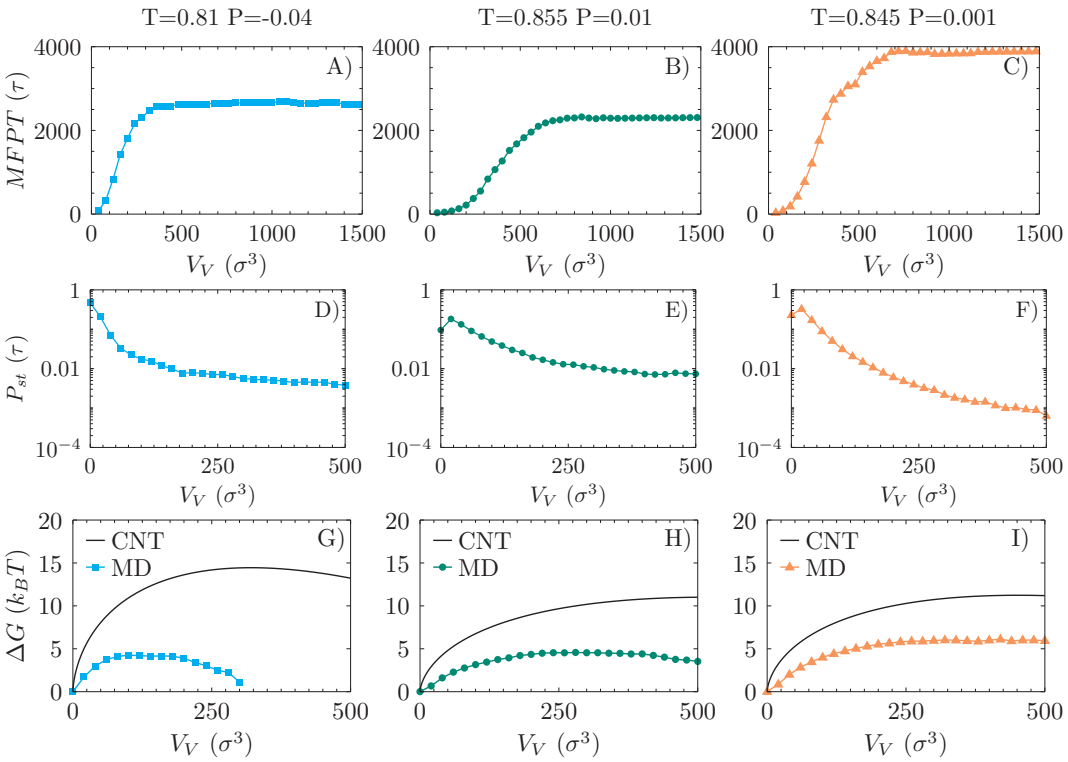

Figure 5.2: (a-c)MFPT as functions of the largest vapor bubble in the system for spontaneous nucleation at three different thermodynamic conditions. (d-f) Stationary probability density functions of the largest vapor bubble in the system. (g-i) Free energy barriers estimated with the approach described in [Wedekind and Reguera, 2008].

the critical size of the bubble, *i.e.* the values at which the bubble grows or shrinks with the same probability. In the system here studied we found $P_B(V_V^*) = 0.5$ at $V_V^* \sim 2500$. The committor at the first interface, $P_B(\lambda_0) \sim 10^{-18}$, multiplied by the flux across λ_0, $\Phi_0 \sim 10^{-5}$, is by definition the nucleation rate $J_{FFS} = 10^{-23}$, with an estimated statistical error [Allen et al., 2006b] of one order of magnitude.

In the simulations carried out with the brute force integration of the equation of motion, the nucleation rate has been evaluated as the inverse of the MFPT evaluated at the values corresponding to the plateaus of Fig. 5.2(a-c). The numerical values of nucleation rate are reported in Tab. 5.1.

FFS Free energy and comparison with CNT At $T = 0.855$ and $P = 0.026$, FFS approach has been implemented forward and backward in order to evaluate the free energy barrier, consistently with the estimation of the nucleation rate (see

Sec. 3.3.4). Results, obtained using the set of interfaces listed in Sec. 5.3, are shown in Fig. 5.1(b) (red points). In the same panel we report the CNT energy profiles (5.3) (black line) and with a quasi static atomistic simulation technique, Restrained hybrid Monte Carlo (RhMC) [Marchio et al., 2018] (blue points).

In the CNT one assumes that, at each volume V_V, the bubble has a spherical shape, that is the configuration that minimizes the energetic cost due to the presence of a liquid/vapor interface. This hypothesis of conditional equilibrium is coherent with quasi equilibrium descriptions of the mechanism. For example, simulations that exploit V_V as order parameter can be carried out *e.g.* with the RhMC quasi static approach used in [Marchio et al., 2018] simulations. When conditional equilibrium is enforced at given fixed values of V_V, bubble shapes are expected to fluctuate around the minimum energy configuration compatible with the imposed restraint, *i.e.* around a spherical shape of a bubble of volume V_V.

In the FFS (or brute force MD) dynamical trajectories, as widely discussed in Sec. 5.4.2, the inception of nucleation process is ruled by fluctuation in local kinetic energy and bubble expansion is observed to take place very quickly.

The "inertia" in the order parameter space, which drives the system to overcome the free energy barrier, may prevent the shape of the bubble to relax towards its minimum free energy configuration (see fig. 5.5). If the shape is not spherical, the excess area in the liquid vapor interface increases the work to form a non spherical bubble of given value V_V. This can be seen as one of the possible explanation of the small discrepancy between FFS and RhMC free energy profiles. Indeed, FFS barrier is systematically higher than RhMC barrier.

The free energy barriers are respectively $\Delta G_{FFS}(V_V^*) = 43 k_B T$, $\Delta G_{RhMC}(V_V^*) = 41 k_B T$, and $\Delta G_{CNT}(V_V^*) = 47 k_B T$. The first two simulative method are in agreement. CNT overestimation of the barrier is instead due to the fact the Tolman [Tolman, 1949] correction to the surface tension has not been taken into account.

Free energy profiles obtained from brute force MD simulation carried out at the three remaining thermodynamic points are shown in Fig. 5.2(g-i). These are obtained using the following expression derived in [Wedekind and Reguera, 2008]:

$$\beta \Delta G(V_V) = \ln(B(V_V)) - \int \frac{dV_V'}{B(V_V')} + C, \tag{5.10}$$

where

$$B(V_V) = \frac{1}{P_{st}(V_V)} \left[\int_0^{V_V} P_{st}(V_V') dV_V' - \frac{\tau(V_V)}{\tau(V_V^*)} \right], \tag{5.11}$$

C is a constant and $P_{st}(V_V)$ is the stationary probability density function of the order parameter V_V, shown in Fig. 5.2(d-f). In the same panels, the CNT estimations of the free energy profiles are shown as black lines. Also in this case, the surface tension adopted in Eq. (5.3) corresponding to the case of a planar surface, probably overestimate the real value, especially in the case of small bubbles. In particular, for spontaneous nucleation, in which the volume of the critical bubbles are very small, the effect of neglecting the curvature of the liquid vapor interface has a more evident effect on the free energy with respect to the previous case.

Kinetic prefactor The estimation of the nucleation rate and free energy barrier from simulations can be used to estimate the contribution of the kinetic prefactor of Eq. (5.5).

MD and theoretical resultsobtained from Kramers (Eq. (5.2)) and from Blander-Katz (Eq. (5.4)) are reported in Tab. 5.1.

	MD			CNT	CNT+BK		CNT+Kr	
	ΔG	Γ_0	J	ΔG	Γ_0	J	Γ_0	J
$P0.026\ T0.855$	42	10^{-4}	10^{-23}	47	10^{-1}	10^{-21}	10^{-4}	10^{-25}
$P-0.04\ T0.81$	4	10^{-5}	10^{-7}	14	10^{-1}	10^{-7}	10^{-5}	10^{-11}
$P0.01\ T0.855$	5	10^{-5}	10^{-7}	11	10^{-1}	10^{-6}	10^{-5}	10^{-10}
$P0.001\ T0.845$	6	10^{-5}	10^{-8}	11	10^{-1}	10^{-6}	10^{-5}	10^{-10}

Table 5.1: Results for nucleation barriers, kinetic prefactor, and nucleation rate. ΔG is expressed in units of k_BT, Γ_0 and J in units of $\sigma^{-3}\,\tau^{-1}$.

Kinetic prefactor obtained from FFS and brute force MD simulations are found to be in perfect agreement with the one predicted by Kramers theory. At the same time they differ by three or four order of magnitudes from Blander-Katz estimation. However, it is crucial to notice that when Eq. (5.4) is combined with the CNT estimation of the barrier to obtain the nucleation rate, a cancellation between errors can improve the agreement with the nucleation rate obtained from simulations. Indeed CNT overestimation of the barrier partially balances the BK overestimation of the kinetic prefactor, producing a deceptive agreement.

5.4.2 Dynamical properties of reactive trajectories

Inception of nucleation In order to characterize significant time dependent properties of the system during the inception and the growth of a nucleating bubble, we analyse nucleation pathways obtained from MD simulations here performed.

For each FFS trajectory, we identify the spatial point where nucleation starts. In the following, we will call this point origine of the nucleation.

We then analyse trajectories passing by this point according to three different classes: i) nucleating trajectories; ii) segments of trajectories reaching the next interface, regardless if they are reactive or not; iii) "failing" segments of trajectories, branches of trajectories that do not react the next interface (starting from the present one). This will allow us to better understand the effect of the various parameters on the success of the trajectory. Temperature in a region within $r_c = 2.5\sigma$ from the origin point of nucleation has been evaluated *via* the following estimator:

$$< T(r_c) >= \frac{1}{3N(r)N_{seg}} \sum_{i=1}^{N} \sum_{j=1}^{N_{seg}} m\mathbf{v}_{ij}^2 \Theta(r_c - r_{ij}), \tag{5.12}$$

where $N(r)$ is the average number of particles at distance within r_c from the origin of nucleation, N_{seg} is the number of trajectory segments considered (which depends on the class of trajectories), m is the mass of a particle, N is the total number of particles, $\mathbf{v}_{ij}^2$ is the velocity of the i-th particle in the j-th segment, and $\Theta(r_c - r_{ij})$ is the Heaviside step function which is 1 if the distance of the particle from the origin r_{ij} is within 2.5σ, 0 otherwise.

Results obtained from FFS simulations are shown in Fig. 5.3(a).

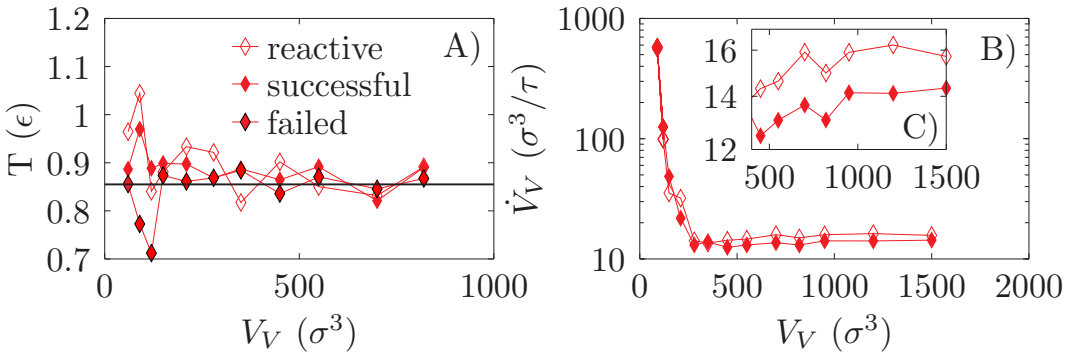

Figure 5.3: (a) Temperature within 2.5 σ from nucleation site as a function of bubble volume for reactive path (empty red points), successful trials (filled red points), and unreactive paths (black/red points). (b) Bubble expansion velocity as a function of bubble volume for reactive path (empty red points), and successful trials (filled red points).

The data show, at the initial stage of the successful nucleation events, a local fluctuation resulting in an excess of the local kinetic energy. This finding is in agreement with the results of Wang et al. [Wang et al., 2008]. Kinetic energy fluctuations

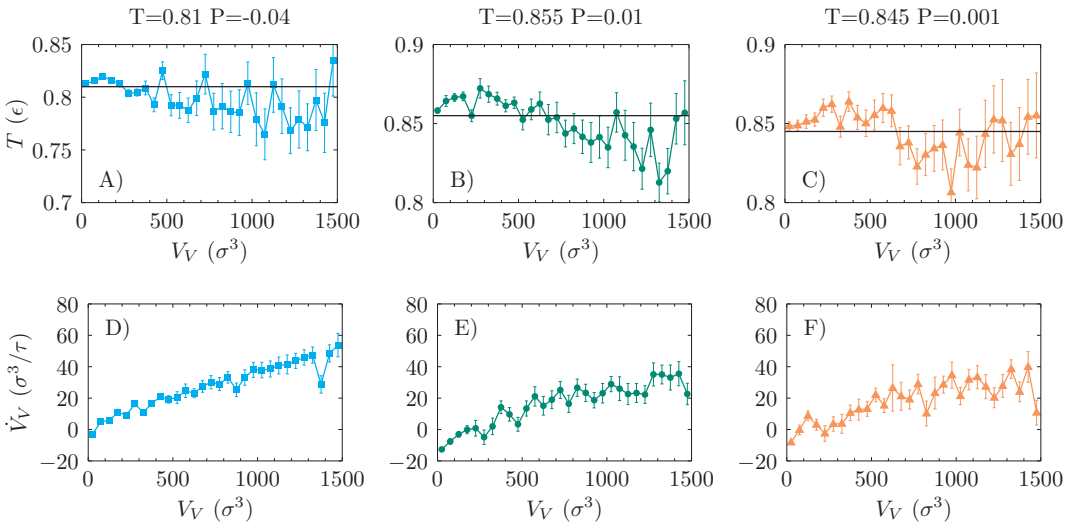

Figure 5.4: estimation of the average kinetic energy as a function of the bubble radius for at interfaces with indexes from 1 to 6. The average is performed in (a) panel over successful segments (reaching the following interface) which belongs to one, or more, reactive trajectories (reaching also the bubble critical size). for (b) panel over the entire set of successful segments, regardless they belongs or not to reactive trajectories.

are the source of the driving force which allows the system to overcome the energetic barrier which divides the liquid from the vapor states. Another important aspect that emerges from the data is that local fluctuations, at least at the first stage of nucleation, are more pronounced in the first set of segments analysed, *i.e.* the ones which are part of one or more reactive trajectories, than in the second set, where all successful trials are taken into account, regardless they belong or not to a reactive trajectory.

The same analysis has been performed for the trajectories obtained from the brute force simulations at thermodynamic conditions at which nucleation occurs spontaneously. Results are shown in Fig. 5.4(a-c). In these thermodynamic conditions, where the barrier is negligible and the critical size of the bubble is relatively small, it is still evident that the initial phase of vapor inception is characterized by a positive fluctuation of the local kinetic energy. Moreover, after the critical size of the bubble is reached, a cooling of the bubble core is observed that is typical of expansion processes.

Inertia along reactive trajectory In order to characterize the dynamical properties of reactive trajectories, the second observable that we consider is the velocity at

which bubbles expands, *i.e.* the variation in time of the bubble volume. In Fig. 5.3(b) we report bubble expansion velocity $\dot{V}_V$ as a function of the bubble volume. Trials are gathered in two subgroups. The first one (filled points) corresponds to the trajectories which reach the interfaces and then return in the liquid basin. The second set (empty points) consists of the trials that reach the current interface and successfully go to the vapor domain. As a first remark, we notice that for activated nucleation at the first stage, which corresponds to the stage ruled by kinetic energy fluctuations as observed in previous paragraph, bubble expansion is faster than in the rest of the trajectories where it is found to approximately become stable around a given value. Moreover, trajectories which succeed in nucleation are found to proceed faster than the ones that return in the liquid basin.

Since along reactive trajectories bubbles grow very quickly, their shapes may not have enough time to relax toward their minimum energy configurations. This statement is in agreement with the results presented in Sec. (5.4.1) where the free energy estimated by dynamical trajectories are found slightly higher than the one obtained with quasi-static RhMC calculation.

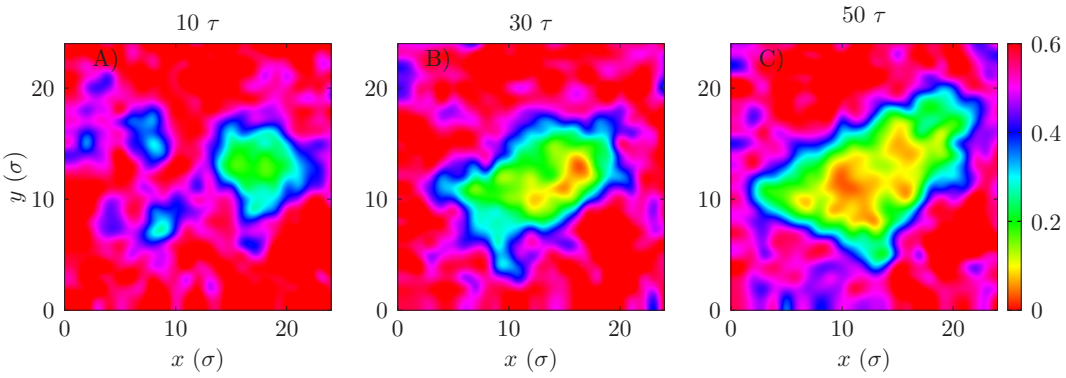

Figure 5.5: 2d Density field obtained considering a slice of the system volume. The shape of the bubble is not spherical and, during growth, bubble remain elongated along the same direction.

As a further evidence of this circumstance, in Fig. (5.5) we report a 2d density field of a system slice at different times along a single reactive trajectory. In panel (a), the initial stage of nucleation characterized by local fluctuations and small cavities is observed. In panels (b) and (c), the bubble grows remaining slightly elongated along the same xy bisectrix direction.

Bubble expansion velocity for spontaneous nucleation simulations are reported

in Fig. 5.4(d-f). Differently from the previous thermodynamic condition, in this in which the free energy barriers are negligible bubble expansion velocity is found to monotonically increase.

5.5 Conclusions

In this work vapor bubble nucleation within a metastable liquid has been addressed analysing the dynamical aspects of the mechanism. MD has been adopted to obtain dynamical trajectories. Moreover, in order to simulate one of the thermodynamical points at which nucleation is very infrequent, MD has been combined to the FFS method, a rare event technique able to preserve the dynamics. The quantitative results obtained from simulations have been used to validate theories that are routinely used to estimate relevant quantities *i.e.* nucleation barrier, nucleation barrier, and kinetic prefactor in the Eyring formula. Moreover, our results confirm the role of thermal fluctuation in triggering the inception of the nucleation event.

Chapter 6

Inertial effects in wetting and drying of nano-patterned surfaces

Hydrophobic nanotextured surfaces, also known as superhydrophobic surfaces, have a wide range of technological applications, including self-cleaning glasses, sanitary fittings, wall paints, anti-moisture, anti-icing and anti-fogging, drop-wise condensation to enhance energy scavenging and water harvesting, friction/drag reduction, anti-adhesion and anti-corrosion. The accidental complete wetting of surface textures, which *destroys* superhydrophobicity, and the opposite process of recovery are two crucial processes that can prevent or enable the technological applications mentioned before. Understanding these processes is key to design surfaces with tailored wetting and recovery properties. However, recent experiments have suggested that the currently available theories are insufficient at describing the observed phenomenology. In this work we offer a dynamical picture of these processes beyond the state of the art showing that the key ingredient determining the experimental behavior is the inertia of the liquid in the wetting and dewetting processes, which is neglected in microscopic and macroscopic *quasi-static* theories inspired to the classical nucleation theory. Present findings are also important for other related phenomena, such as heterogeneous cavitation, where vapor/gas bubbles form at surface asperities.

A textured hydrophobic surface can entrap gas/vapor in its surface corrugations that keeps a liquid deposited on it in a *suspended* state, also known as the Cassie-Baxter state [Cassie and Baxter, 1944]. This suspended state is characterized by a reduced solid/liquid contact area to which a set of properties, such as large (ap-

parent) contact angle [1], low contact angle hysteresis [2], and low tilting angle [3], are associated that. These properties are collectively denominated *superhydrophobicity* [Miwa et al., 2000, Feng et al., 2002, Zhang et al., 2008, Nosonovsky and Bhushan, 2009, E et al., 2017]. Superhydrophobic surfaces are suitable for many technological applications including self-cleaning glasses, sanitary fittings, and wall paints, [Zhang et al., 2016a] anti-moisture and/or anti-icing coatings [Cao et al., 2009], anti-fogging, [Howarter and Youngblood, 2008] surfaces for drop-wise condensation to enhance energy recovery/scavenging [Enright et al., 2014a] and water harvesting [Zhang et al., 2016b], friction/drag reduction, anti-adhesion and anti-corrosion [Ferrari and Benedetti, 2015], boiling enhanced heat transfer [Patankar, 2010] and many more.

A second state exists, known as the Wenzel state, [Wenzel, 1936] in which the liquid completely wets the corrugations of the hydrophobic surface. In the Wenzel state the liquid/solid contact area is much larger and the superhydrophobic properties are lost. The Cassie-Baxter/Wenzel (wetting) transition can be induced by changes of pressure and/or temperature [Brennen, 2013, Betz et al., 2013]; the spontaneous reverse transition (recovery) has proven to be impossible in most practical circumstances even when initial conditions are restored [Checco et al., 2014, Amabili et al., 2016a, Lafuma and Quéré, 2003]. The *fragility* of the Cassie-Baxter state and the difficulty of recovery have hindered the use of superhydrophobic surfaces in practical applications. Thus, an intense experimental and theoretical research activity has been devoted to the investigation of the wetting and recovery mechanisms and of how surface morphology determines the stability of the Cassie-Baxter state and the kinetics of the forward and reverse transition [Lafuma and Quéré, 2003, Lee and Kim, 2011, Lv et al., 2015, Xue et al., 2016, Wang et al., 2017, Amabili et al., 2016a, Giacomello et al., 2012b, Giacomello et al., 2012a, Giacomello et al., 2015, Kusumaatmaja et al., 2008, Checco et al., 2014, Vrancken et al., 2009, Poetes et al., 2010, Giacomello et al., 2016a, Prakash et al., 2016, Lisi et al., 2017, Panter and Kusumaatmaja, 2017, Yao and Ren, 2015, Li and Ren, 2014, Ren, 2014, Savoy and Escobedo, 2012a, Savoy and Escobedo, 2012b, Tretyakov and Müller, 2013, Li et al., 2017, Pashos et al., 2015, Pashos et al., 2016], including the possible effect of dissolved

[1] The Young and apparent contact angle of a liquid is the angle formed by the tangent to the droplet at contact point with the surface and the flat and textured surface itself. In the case of a textured surface, the nominal position of the surface is the plane passing by the top of the corrugations.

[2] The contact angle hysteresis is measured by the difference between the front and rear contact angles right before the droplet depins and slides/rolls along a tilted surface

[3] The tilting angle is the maximum angle the surface can be tilted before the droplet deposited on it starts moving

incondensable gasses [Giacomello et al., 2013, Xiang et al., 2017].

At the conditions of interest for experiments and technological applications the wetting and recovery transitions are often characterized by large relatively free-energy barriers ($\Delta\Omega_w^\dagger$ and $\Delta\Omega_r^\dagger$, respectively) separating the initial and final states. In the presence of barriers larger than the thermal energy k_BT (k_B Boltzmann constant and T the temperature) the transition time scales exponentially with $\Delta\Omega_{w/r}^\dagger$, $\tau_{w/r} = \tau_{w/r}^0 \exp(\Delta\Omega_{w/r}^\dagger / k_BT)$ [Eyring, 1935, Zwanzig, 2001], thus $\tau_{w/r}$ can easily exceed the timescale accessible to experiments and simulations. The very presence of barriers prevents the recovery of the Cassie-Baxter state upon wetting of the corrugations for most of the textured surfaces. Indeed, one of the objectives of the research in this field is to understand the relation between the morphological and geometrical characteristics of the corrugations and the wetting/recovery transition time. [Lee and Kim, 2011, Savoy and Escobedo, 2012a, Lisi et al., 2017, Prakash et al., 2016, Vrancken et al., 2009]

Due to the long transition time, largely exceeding the timescale accessible to *brute force* (continuum and/or atomistic) simulations, special techniques are necessary to investigate the wetting and recovery transitions. Apart from notable exceptions [Savoy and Escobedo, 2012b], the wetting and recovery of textured surfaces has been studied only via *quasi-static methods*, such as umbrella sampling [Prakash et al., 2016], restrained molecular dynamics [Giacomello et al., 2012b, Giacomello et al., 2013, Giacomello et al., 2015], string and nudged elastic band methods [Giacomello et al., 2015, Panter and Kusumaatmaja, 2017, Yao and Ren, 2015, Li and Ren, 2014, Ren, 2014, Pashos et al., 2015, Pashos et al., 2016]. These methods assume that the process is slow and the system is at the *local equilibrium* all along wetting or recovery. In other words, these methods neglect *dynamical effects*, such as inertia. The most probable wetting path predicted by quasi-static approaches – the one associated to the lowest free-energy barrier – breaks the symmetry of the system, e.g., it is characterized by the formation of a gas bubble in the corner of 2D or 3D rectangular pores [Giacomello et al., 2012b, Giacomello et al., 2012a, Giacomello et al., 2015, Lisi et al., 2017, Kusumaatmaja et al., 2008]. A similar asymmetric path, together with the symmetric one, has been observed in experiments. The change of symmetry was ascribed to the presence of impurities in the surface corrugations rather than to the fundamental physics of the process [Lv et al., 2015, Xue et al., 2016].

The objective of this work is to go beyond the quasi-static picture and to establish a comprehensive theory of wetting and recovery of textured surfaces which includes dynamical effects in order to close the gap with experiments. This extended frame-

work is expected to be relevant also for related phenomena, such as heterogenous cavitation, which hardly conforms to a quasi-static picture [Bremond et al., 2005]. To achieve our aim we will study the process over a wide range of thermodynamic conditions. In particular, we will consider thermodynamic conditions corresponding to long and short wetting and recovery transition times. The former corresponds to ambient conditions for most of the common textured hydrophobic surfaces. The latter to more extreme conditions used in wetting experiments on common superhydrophobic surfaces, or milder conditions for novel surfaces. This will allow us to assess whether the standard nucleation theory framework [Kelton and Greer, 2010, Meloni et al., 2016], used to interpret the wetting and recovery transition is adequate to explain recent experiments and to model novel materials. Present results are of interest from both the fundamental and the applicative points of view: in addition to revealing paramount dynamical effects in nucleation, such a theory opens the way to design surfaces with tailored properties that can better resist to intrusion [Amabili et al., 2016b, Giacomello et al., 2016b, Panter and Kusumaatmaja, 2017] and enable facile recovery [Lisi et al., 2017, Prakash et al., 2016].

Anticipating our results, we remark that our simulations allow to reconcile the experimental and theoretical picture of the wetting process: when the free-energy barrier is sufficiently low – close to the values at which the experimental transition is expected to occur – dynamical effects dominate and the meniscus advances in the pores preserving the initial symmetric shape. Similarly, at conditions relevant for the experiments the recovery transition always proceeds asymmetrically with the formation and growth of a bubble in a corner. At variance with the quasi-static picture [Giacomello et al., 2012a, Giacomello et al., 2013, Giacomello et al., 2015, Prakash et al., 2016, Panter and Kusumaatmaja, 2017, Li and Ren, 2014, Ren, 2014, Pashos et al., 2015, Pashos et al., 2016], the present results show that dynamical effects are strongly dependent on the liquid pressure.

We investigated a system consisting of a Lennard-Jones (LJ) liquid wetting a square cavity (Fig. 6.1A) 6.2. Liquid and solid particles interact *via* the modified LJ potential

$$U_{LJ}(r_{ij}) = \epsilon \left[\left(\frac{\sigma}{r_{ij}} \right)^{12} - c_{ij} \left(\frac{\sigma}{r_{ij}} \right)^{6} \right], \tag{6.1}$$

where r_{ij} is the distance between atoms i and j, and ϵ and σ set the energy and length of the particle-particle interactions, respectively. c_{ij} is a scaling parameter which is equal to 1 for atoms of the same species (liquid-liquid or solid-solid) and

P	$\Delta\Omega_{CB/W}$	$\Delta\Omega^{\dagger}_{CB/W}$	$\Delta\Omega^{\dagger}_{W/CB}$
-0.168	-130	133	3
-0.08	-74	91	17
-0.005	21	17	38
0.01	31	12	43
0.035	57	0	57

Table 6.1: Relative free energy between the Cassie-Baxter and Wenzel states, $\Delta\Omega_{CB/W} = \Delta\Omega_{CB} - \Delta\Omega_{W}$, wetting, $\Delta\Omega^{\dagger}_{CB/W}$, and recovery free energy barriers, $\Delta\Omega^{\dagger}_{W/CB}$. The pressure, P, is reported in Lennard-Jones units; the relative free energy and barriers are reported in k_BT.

equal to 0.6 for the liquid-solid interaction, determining the wetting properties of the system which are quantified in terms of the Young contact angle $\theta_Y = 102°$ 6.2. This value is typical of silanized or fluorinated surfaces [Chen et al., 1999, Öner and McCarthy, 2000, Grate et al., 2012]. LJ units are used throughout the letter with the exception of the free energy, which is expressed in units of k_BT.

We determined the wetting and recovery path, energetics, and kinetics using two complementary approaches: restrained molecular dynamics (see Sec. 6.1) (RMD [Maragliano and Vanden-Eijnden, 2006b, Bonella et al., 2012, Ciccotti and Meloni, 2011, Meloni and Ciccotti, 2015, Giacomello et al., 2012b, Giacomello et al., 2015]) and forward flux sampling (FFS [Allen et al., 2005, Allen et al., 2006a, Valeriani et al., 2007, Allen et al., 2006b]) (see Sec. 3.3.3). In both approaches the progress of the process is measured by the number of particles in the cavity, $N(\mathbf{r})$, where $\mathbf{r}$ is the vector of atoms positions at the current configuration of the system (Fig. 6.1A). RMD allows to sample the constant number of particles, temperature, and pressure (conditional) ensemble (nPT) at a prescribed number N of particles inside the surface textures. Via RMD one can also compute the free-energy profile and any statistical property along the *quasi-static* process. FFS, instead, samples the ensemble of reactive (wetting or recovery) trajectories at the prescribed nPT conditions. The driving force of the wetting and recovery processes – the liquid pressure – is controlled by the mechanical barostat discussed in Ref. [Marchio et al., 2018]. See Sec. 6.2 for more details.

We first considered a small 10×10 square pore and performed RMD simulations of the intrusion and extrusion processes at different liquid pressures, corresponding to different values of the free energy difference $\Delta\Omega_{CB/W}$ between the Cassie-Baxter and Wenzel states and of the wetting/recovery barrier $\Delta\Omega^{\dagger}$: higher pressures favor

the stability of the Wenzel state and reduce the wetting barrier and *vice versa* (Table 6.1). Consistently with literature results [Giacomello et al., 2012b, Giacomello et al., 2012a, Panter and Kusumaatmaja, 2017], the RMD wetting transition begins with the liquid depinning from the top corners and entering in the cavity with a (almost) flat meniscus (see Fig. 6.1C); in correspondence of the transition state (the maximum of the free-energy profile, $N \sim 450$) the meniscus bends to form a vapor bubble in one of the two bottom corners of the cavity. Then, the bubble shrinks until it disappears when the system reaches the Wenzel state.

A more quantitative analysis of the wetting mechanism is obtained by considering $\Delta N = N_1 - N_2$ and N along the process, with N_1 and N_2 the number of liquid particles in the left and right halves of the cavity (Fig. 6.1B). When the meniscus is flat $\Delta N \sim 0$, when a bubble is formed in a corner, ΔN is either sizably negative or positive. This is shown for RMD simulations in Fig. 6.1D. The same analysis is performed on the FFS simulations and in Fig. 6.1E-G is reported the join probability $\rho(\Delta N; N)$ at $P = -0.005$, 0.01 and 0.035. At low and moderate liquid pressures (panels E and F) the trajectories are initially ($N \leq 500$) symmetric, with $\rho(\Delta N; N)$ centered at $\Delta N = 0$. Then, in correspondence of the transition state, $\rho(\Delta N; N)$ splits in two branches corresponding to the formation of a bubble in the left or right corners. Thus, at low and moderate pressures the FFS wetting path resembles the RMD one. At $P = 0.035$, $\rho(\Delta N; N)$ is centered around zero all along the process, indicating that at high pressure the mechanism becomes symmetric (Fig. 6.1G). FFS simulations of liquid intrusion in a 20×20 pore at $P = -0.005$ and 0.035 show that the transition from asymmetric wetting at low pressures to symmetric wetting at high pressures is a generic feature that is observed also in larger pores(Fig. 6.4).

The transition from the asymmetric to the symmetric path with increasing pressure is in contrast with the *quasi-static* picture [Giacomello et al., 2012a, Giacomello et al., 2012b, Giacomello et al., 2013, Giacomello et al., 2015, Panter and Kusumaatmaja, 2017] and consistent with the experimental observations [Lv et al., 2015, Xue et al., 2016]. Indeed, considering the transition time determined by FFS ($\tau = 10^{30}$, 10^{19}, and 10^{3} at $P = -0.005$, 0.01, and 0.035, respectively, approximately corresponding to 10^{18}, 10^{7}, and $10^{-9}s$ for water) one expects that in experiments wetting takes place only close to spinodal conditions, when the barrier is vanishingly small. Thus, the present results reconcile theory and experiments: once dynamical effects are taken into account the theory predicts that, at experimental conditions, wetting proceeds mainly through the symmetric path.

The discrepancies between FFS and RMD suggest that dynamical effects, ne-

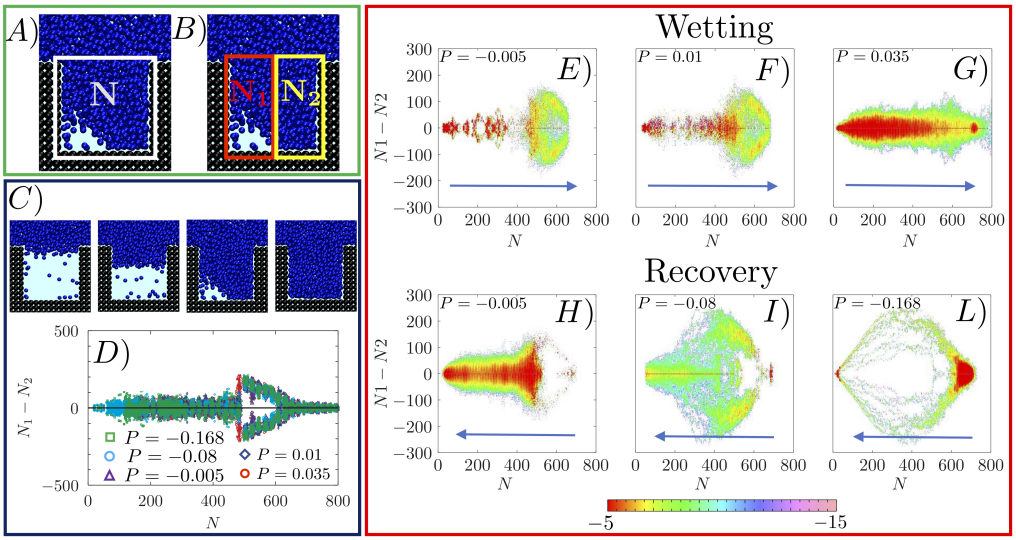

Figure 6.1: A) Computational sample used in the simulation. The blue and brown spheres represent the fluid and solid particles, respectively. The order parameter $N(\mathbf{r})$ is the number of particles comprised within the white frame. B) The red and yellow frames define the boxes used to determine N_1 and N_2 for the calculation of $\Delta N = N_1(\boldsymbol{r}) - N_2(\boldsymbol{r})$. C) Sequence of configurations along the RMD path: the liquid enters in the pore with a flat meniscus, then forms a bubble in a corner and finally the bubble is absorbed and the meniscus touches the bottom wall. The quasi-static process is reversible and thus the recovery path is the reverse of the wetting path. D) $(\Delta N, N)$ values along the RMD wetting (low to high N) or dewetting (high to low N) paths at different positive and negative pressures. Consistently with the snapshots of the panel C), in the early part of the wetting ΔN values centered around 0. At $N \sim 450$ one observes a sharp change, with sizably negative and positive ΔN values. RMD wetting and recovery is independent on the pressure, with pairs of $(\Delta N, N)$ at the different pressures perfectly overlapping. E-L) Logarithm of the probability density, $\log[\rho(\Delta N; N)]$, along the wetting (E-G) and dewetting (H-L) trajectories at different pressures. At low ($P = -0.005$) and moderate ($P = 0.01$) pressures the wetting follows a path consistent with the quasi-static picture of panel D. At higher pressures ($P = 0.035$) $\rho(\Delta N; N)$ is centered around $\Delta N = 0$ all along the wetting path. The recovery always follows a path characterized by an initial ($N > 400$) large positive or negative values of ΔN. However, at small and moderate negative pressures ($P = -0.005, -0.08$) in the second part of the path ($N < 400$) $\rho(\Delta N; N)$ is centered around 0, indicating a recovery of the symmetrical morphology of the meniscus. At more negative pressures ($P = -0.168$) $\rho(\Delta N; N)$ remains centered at large negative or positive values all along the recovery.

glected in the latter approach, play a crucial role in the wetting of the cavity at spinodal conditions. We speculate that inertia of the intruding liquid prevents the bending of the meniscus when the Cassie-Baxter/Wenzel barrier is low and the liquid can rush into the cavity: in this condition the (thermodynamic) force is not sufficient to change the shape of the liquid/gas interface to the minumum free-energy morphology. This hypothesis is supported by the observation that the velocity of advancement of the meniscus, measured by $\dot{N}$, significantly increases with the liquid pressure in correspondence of the transition state while the velocity of bending of the meniscus, estimated by $\Delta\dot{N}$, does not change significantly with P (Fig. 6.5).

We now consider the recovery process by which vapor is formed within the pore and pushes the liquid back to the top of corrugation restoring the Cassie-Baxter state. We remark that this process is equivalent to cavitation or bubble nucleation under confinement, which are important in many applications [Neppiras, 1980, Blake and Gibson, 1987, Suslick et al., 1999, Betz et al., 2013, Coussios and Roy, 2008]. Given the findings on the wetting path, a question naturally arises: do dynamical effects play an important role in the recovery path as well? To address this question we considered three negative liquid pressures (suction), $P = -0.05$, $P = -0.08$, and $P = -0.168$ corresponding to large ($\Delta\Omega^\dagger \sim 40 k_B T$), intermediate ($\Delta\Omega^\dagger \sim 10 k_B T$), and negligible free-energy barriers, respectively. Fig. 6.1H-L shows $\rho(\Delta N; N)$ along dewetting reactive trajectories. One notices that in all cases the process is asymmetric and begins with the formation of a bubble in a corner. However, at moderately negative pressures – i.e., when the recovery barrier is large – right after the transition state the system recovers the symmetric configuration consistently with the quasi-static picture. At more negative pressures, instead, the interface becomes even more asymmetric, maintaining this morphology for most of the recovery path. Only when the meniscus pins to one of the corners at the top of the cavity, the symmetric Cassie-Baxter state is recovered. Similarly to the wetting case, at large negative pressures, when the recovery barrier is negligible, the velocity of the extruding liquid is too fast for the meniscus to reach the equilibrium configuration at that N (Fig. 6.5). In other words, like in the case of wetting, when the extrusion barrier is very low inertial effects dominate.

The inertial effects discussed above cause deviation from other equilibrium properties of the meniscus along wetting and recovery, namely, the value of the contact angle and the curvature of the meniscus. For recovery, these effects are shown in Fig. 6.6. In FFS simulations at moderately negative pressures (P = -0.005) the contact angle θ at the two contact points of the meniscus are equal between them and

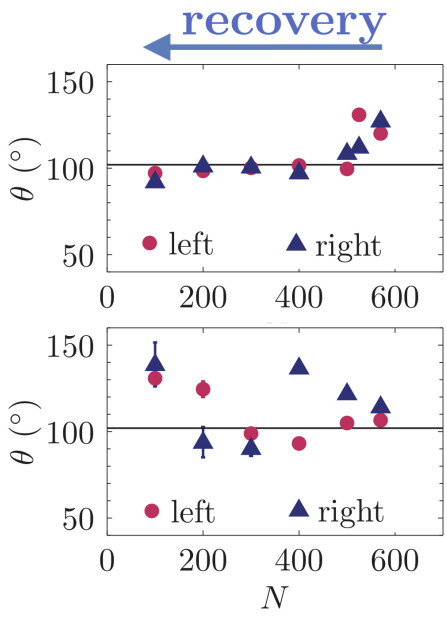

Figure 6.2: Contact angle of the meniscus at the left and right liquid/vapor/solid contact points at $P = -0.005$ (top) and -0.168 (bottom). The contact angle is determined from the derivative of a polynomial interpolation of the liquid/vapor Gibbs interface at its intersect with the solid walls.

very close to the Young value, $\theta_Y = 102°$, all along the process. The departure from θ_Y for small vapor bubbles is due to the limited accuracy in the determination of θ in these conditions. On the contrary, at $P = -0.168$, where (non-equilibrium) inertial effects are large, the values of θ at the two contact points are significantly different for most of the recovery path and very different from θ_Y. In particular, we observe a *jump* in the value of θ at the right contact point when the bubble detaches from the bottom wall ($N \sim 300$ Fig. 6.6). Also notice that the curvature of the meniscus when the recovery is almost complete is opposite to the one predicted by quasi-static theories (see Fig. 6.6).

Concluding, the present simulations have shown that, by including the dynamics in the description of (thermally activated) wetting and dewetting of complex surfaces, it is possible to reconcile experimental and theoretical results. Contrary to previous quasi-static predictions, it was found that the wetting and dewetting transition paths sensitively depend on the liquid pressure, underscoring the importance of liquid inertia. These dynamical effects play a crucial role in enhancing the difference between the wetting and dewetting processes, which are shown to follow symmetric and asymmetric paths, respectively, in typical experimental conditions: hopefully

new experiments will substantiate these new predictions. The revealed phenomenology is explained in terms of a competition between thermodynamic forces and inertia of the moving liquid, which applies to a variety of physical phenomena well beyond wetting: condensation, cavitation, dynamics of the triple line, micel formation and many more.

The implication for simulations is that, when the free-energy barriers characterizing a transition are low, it is crucial to include the dynamics beyond the quasi-static assumption common to many theories (e.g., classical nucleation theory) and rare event methods (e.g., umbrella sampling, restrained MD).

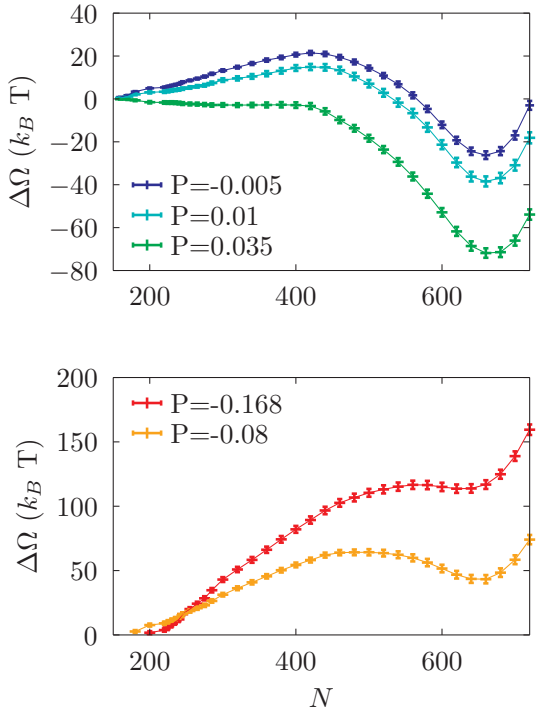

Figure 6.3: Free energy profiles as a function of the number of particles inside the pore computed *via* RMD at various pressures. The Cassie-Baxter state is at $N \approx 200$, while the Wenzel one is at $N \approx 700$. The error bars representing the error on the free energy at each value of N are also reported. arbitrary constant in the free energy has been set so that $\Delta\Omega = 0$ at the Cassie-Baxter state.

6.1 Restrained Molecular Dynamics

The objective of the restrained molecular dynamics, RMD, is to sample the conditional density probability at a prescribed value of an observable, here the number of

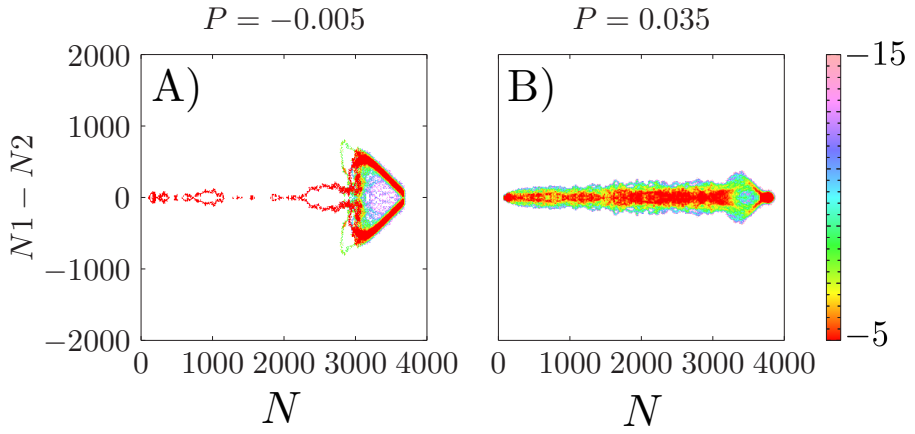

Figure 6.4: Logarithm of the joint probability density function $\rho(\Delta N, N)$ along reactive trajectories in the system with the 20×20 pore at pressures $P = -0.005$ (A) and $P = 0.035$ (B). With increasing pressure the intrusion mechanism passes from asymmetric (A) to symmetric (B).

fluid particles in the pore, and the associated (Landau) free energy. The free energy Ω is defined as:

$$\begin{aligned} \Omega(N^*) &= \beta^{-1} \log \rho_N(N^*) \\ &= \beta^{-1} \log \int d\boldsymbol{r}\, m(\boldsymbol{r}) \delta(N(\boldsymbol{r}) - N^*) \end{aligned} \tag{6.2}$$

where N^* is a particular value of the number of particles in the pore $N(\boldsymbol{r})$, $\beta = 1/k_B T$ is the inverse of the thermal energy, $\delta(\cdot)$ is the Dirac delta function, $m(\boldsymbol{r})$ is the distribution in the proper ensemble, e.g. NPT, and $\rho_N(N^*)$ is the probability density function to observe the value N^* of the observable $N(\mathbf{r})$. In Eq. (6.2) one can replace the Dirac delta functions with a smooth Gaussian approximation, $g_\lambda(\phi_k(\boldsymbol{r}) - N_k) = \sqrt{2\pi/(\beta\lambda)} \exp[-\beta\lambda/2\,(\phi_k(\boldsymbol{r}) - N_k)^2]$. Within this approximation, the derivative of the free energy reads

$$\begin{aligned} \frac{\partial \Omega(N^*)}{\partial N} &\approx \frac{\partial \Omega_\lambda(N^*)}{\partial N} = \\ &= \frac{\int d\boldsymbol{r}\ \lambda\,(N(\boldsymbol{r}) - N^*)\, m(\boldsymbol{r}) g_\lambda(N(\boldsymbol{r}) - N^*)}{\int d\boldsymbol{r}\ m(\boldsymbol{r}) g_\lambda(N(\boldsymbol{r}) - N^*)} \\ &= \int d\boldsymbol{r}\ \lambda(N(\boldsymbol{r}) - N^*)\, \rho(\boldsymbol{r}|N^*)\ . \end{aligned} \tag{6.3}$$

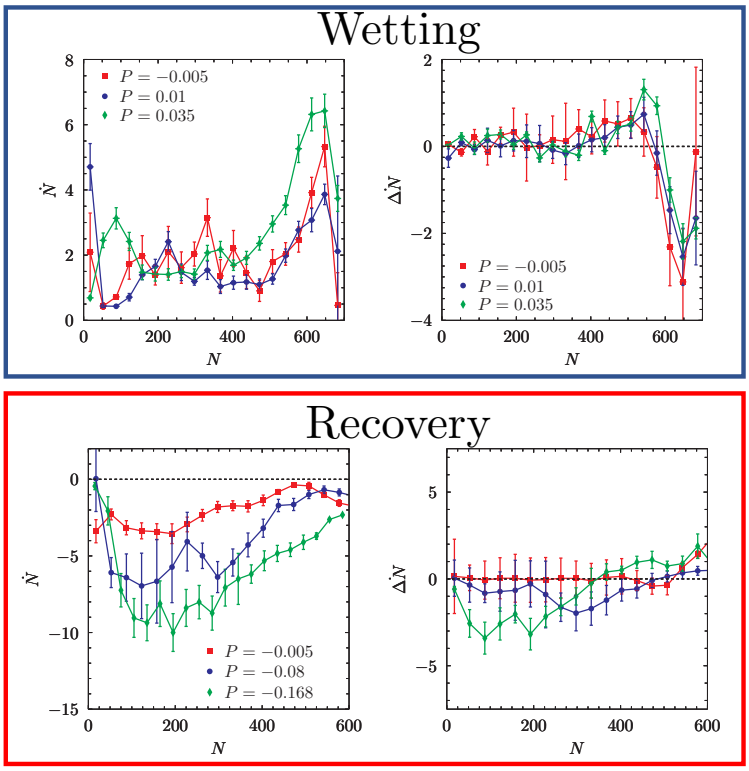

Figure 6.5: $\dot{N}$ (left) and $\Delta\dot{N} = \dot{N}_1 - \dot{N}_2$ (right) as a function of N. $\dot{N}$ measures the velocity of advancement of the liquid in the pore and $\Delta\dot{N}$, the velocity of *sloshing* of liquid from one half box to the other, measures the velocity of bending of the meniscus. In the top and bottom rows we report data for intrusion and extrusion, respectively. The sign of $\Delta\dot{N}$ has been handled so that the sloshing left to right is not compensated from the opposite one in the formation of left and right bubbles. The dashed line representing zero velocity is reported when necessary.

where $\rho(\boldsymbol{r}|N^*)$ is the conditional probability density to find the system in the configuration $\boldsymbol{r}$ given that there are N^* particles in the pore. Thus, one can obtain the free energy profile by numerical integration of the approximate derivative of the free energy of Eq. 6.4 Here, we have set $\lambda = 0.2$, which has already been tested in previous works to be a good trade-off between the convergence of $\partial\Omega_\lambda(N^*)/\partial N$ with λ and the statistical error of the mean force (see, e.g., Refs [Amabili et al., 2016b, Amabili et al., 2016a, Amabili et al., 2017].

Assuming that the ensemble is at constant temperature, $m(\boldsymbol{r})g_\lambda(N(\boldsymbol{r}) - N^*) = \exp\left(-\beta(V(\boldsymbol{r}) + \lambda/2(N(\boldsymbol{r}) - N^*)^2)\right)$, which can be sampled by a constant temperature MD driven by the *augmented* potential $\tilde{V}(\boldsymbol{r}; N^*) = V(\boldsymbol{r}) + \lambda/2(N(\boldsymbol{r}) - N*)^2$,

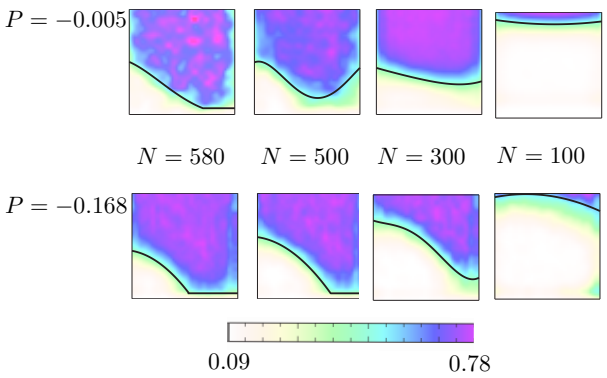

Figure 6.6: Number density field of the fluid at selected points along the recovery process as obtained from FFS at $P = -0.005$ and -0.168. The density field is obtained by discretizing the pore in squared boxes and computing the contribution to the number of particle within each box from Gasussian distributions of standard deviation 1 centered at each particle position and, finally, dividing by the volume of the box. The Gibbs interface (black line), here a polynomial fitting of the points at mid density between the bulk liquid (violet) and bulk vapor (white) densities is also reported. From the derivative of the Gibbs interface at the intersect with the wall at the left and right triple points one can compute the contact angle along the process.

the so-called *Restrained* MD. Indeed, one can extend this approach to the isothermal-isobaric ensemble, provided that one uses a molecular dynamics suitable to sample this ensemble.

In practice, $\partial\Omega(N^*)/\partial N$ is computed as the time average of $\lambda(N(\boldsymbol{r}) - N^*)$ along the RMD. Indeed, the conditional average of any observable can be computed as time average of a suitable estimator along an RMD trajectory.

6.2 Simulation details

The computational sample for both RMD and FFS simulations consisted of 68820 and 12790 fluid and solid particles, respectively. As explained in the main text, Liquid and solid particles interact *via* the modified LJ potential

$$U_{LJ}(r_{ij}) = \epsilon \left[\left(\frac{\sigma}{r_{ij}} \right)^{12} - c_{ij} \left(\frac{\sigma}{r_{ij}} \right)^{6} \right], \tag{6.4}$$

The parameter c_{ij} is set to 1 for fluid-fluid and solid-solid particles interactions. For fluid-solid interactions c_{ij} is set so that the contact angle θ takes a value close to 100°, the typical of silanized or fluorinated surfaces. [Chen et al., 1999, Öner and

McCarthy, 2000, Grate et al., 2012] The value for c_{ij} is chosen following an iterative procedure consisting of three steps: [Giacomello et al., 2012b, Amabili et al., 2016b] i) perform the simulation of a (cylindrical) droplet deposited on a flat surface with a guess value for c_{ij}, ii) determine the value of the contact angle at the present value of c_{ij}, iii) adjust c_{ij} so as to increase/diminish the hydrophobicity of the surface.

The sample for the determination of the contact angle consisted of 54694 fluid and 70000 solid particles. Simulations were run in the NVT ensemble at the same temperature of the RMD and FFS simulations, $T = 0.8$. The drop (Fig. 6.7/A) has a radius of ~ 20. From the MD trajectory one determines the density field (Fig. 6.7/B) and the (Gibbs) liquid/vapor dividing surface. This surface is fitted with a circumference and the contact angle is the derivative of the circumference at its contact point with the nominal position of the surface.

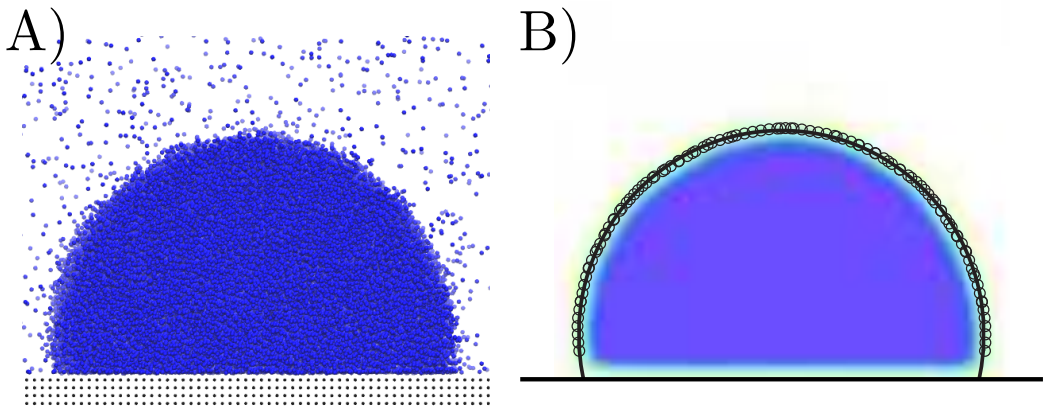

Figure 6.7: A) snapshot of the *atomistic* droplet deposited on a solid surface. In the panel B) is shown the corresponding density field with the circumference fitting fitting the (Gibbs) dividing liquid/vapor surface.

RMD and FFS simulations were run at constant number of particles, temperature and pressure (NPT esemble) using the LAMMPS molecular dynamics code. [Plimpton, 1995] Temperature was controlled using the Nosé-Hoover chain thermostat [Martyna et al., 1992] with a characteristic time of 0.1. Concerning the pressure, we have adopted the mechanical barostat recently introduced by Marchio *et al* [Marchio et al., 2018], which is suited for multi-phase systems. In practice, a solid slab of particles is added above the liquid and an extra force $F_{ext} = PA$ (P is the target pressure and A the area of the solid slab) is applied to these particles (Fig. 6.8). The timestep for the numerical integration of the equation of motion was 0.005.

For RMD simulations we used 35 target values of the order parameter between

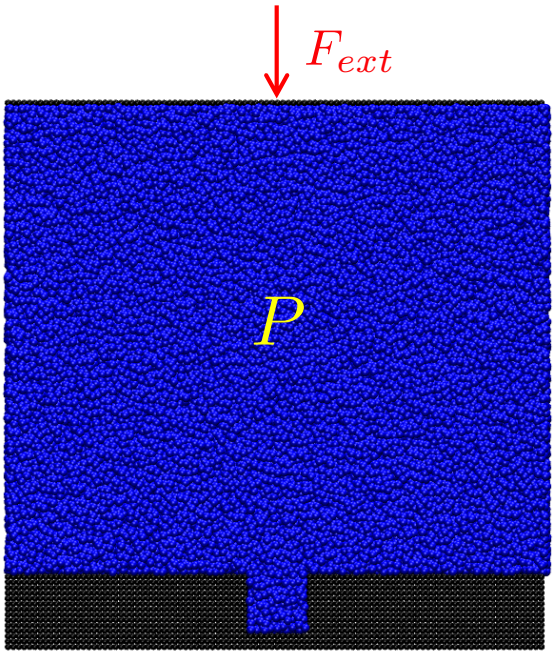

Figure 6.8: Mechanical barostat. An extra slab of solid particles is deposited on the liquid and an extra force is added to these particles that ex

$N^* = 160$ and $N^* = 700$. At each N^* value we performed a 3×10^5 steps long RMD simulation.

The number of FFS interfaces is set such that the probability of reaching the next interface is $0.1 < \rho(N_{j+1}|N_j) < 0.5$. The number of interfaces goes from 15 for the recovery process at very negative pressures to 50 for intrusion at moderate pressure. The distance between interfaces varies along the path, going from a difference of 5 particles in the pore close to the transition state to 60 near the product state.

Chapter 7

Conclusions

The study presented in this thesis concerns bulk and confined vapor nucleation, and wetting of rough surfaces. These topics are relevant in many applications that include energy storage, superhydrophobicity, cavitation, *etc.* Liquid/vapor transitions under confinement are routinely studied with atomistic quasi static theoretical approaches, umbrella sampling [Prakash et al., 2016] and the string method in collective variables [Amabili et al., 2017]. Quasi static simulations based on a continuum description of the multiphase system have also been performed [Magaletti et al., 2015]. Here we investigated the effect of quasi-staticity on a process involving a massive system, the liquid, which might be characterized by a large inertia. Another aspect we investigate is whether the basic algorithms used in the simulations are adequate for nucleation. In fact, standard techniques for the control of the pressure, such as the Martyna-Tobias-Klein barostat, have been developed for homogeneous systems and their use has been extended to nucleation without an assessment of these techniques to phase-change conditions.

Concerning to pressure control, the main issue is how to reproduce the physical conditions of experiments and theoretical models within the relatively small volumes accessible to atomistic simulations. In particular, it has been proven that standard barostating algorithms are unable to control the pressure of the pre-existing phase, the liquid in our case, during the growth of the vapor domain. The reason is that standard, global, barostat controls the pressure of the entire system while in nucleation experiments and theories one controls the pressure of the pre-existing phase. In order to overcome this drawback, that may produce errors of several order of magnitude in the estimation of the nucleation rate, a local barostat has been devised able to selectively control the liquid pressure. Its performances have been tested in

the case of homogeneous bubble nucleation within a metastable superheated liquid and used in the other simulations performed in this thesis.

We first considered homogeneous nucleation. Homogeneous nucleation has been subject of debate in the recent literature, as a result of both qualitative and quantitative inconsistencies in the results obtained by different groups. As an example, it is not yet well established whether local fluctuations of temperature (*hot spots*) are responsible for bubbles inception or not. Our simulations confirm that hot spots are responsible for nucleation both at positive and negative pressure, *i.e.* even when the liquid is in tensile conditions. We have also shown that for homogeneous nucleation dynamical (inertial) effects are not negligible, though they do not affect dramatically the energetics (free energy barrier) and mechanism of the process. From the qualitative point of view, the major difference is that nucleation takes place via the formation of a prolate bubble and the larger liquid/vapor surface per volume results in an increase of the nucleation barrier. To determine the nucleation rate by quasi-static approaches one usually takes advantage of approximated formulas for the exponential prefactor. We considered two of the most widely used formulas, the Blander and Katz and the one derived from Kramers theory, and have shown that the latter is able to give overall nucleation rate in good agreement with direct estimate based on techniques taking into account kinetic effects.

The last stage of the work has been devoted to study the wetting and recovery of superhydrophobic surfaces. The wetting process corresponds to liquid intrusion within surface defects, while recovery, the reverse process, takes place via confined bubble nucleation after which vapor phase is established again within the asperities. Dynamical simulations have been carried out here in order to reconcile the mismatch between experimental and theoretical pictures of the process. In particular, previous quasi-static simulations provided a wetting path in which the meniscus initially entered in the cavities with an almost flat shape and then, when it is close to the bottom of the corrugations, it bends to form a bubble in the corner. This is in contrast with recent experiments showing that the meniscus remains flat all along the wetting. The simulation here performed, in contrast with umbrella sampling and string simulations, show that the properties of the meniscus strongly depend on the thermodynamic conditions (in this particular case on the liquid pressure) at which the process occurs. Indeed, the asymmetric wetting path observed in quasi-static simulations is found only when the wetting barrier is large (several tens of k_BT). When the barrier is low the inertia of the liquid dominates and the wetting is symmetric, as observed in experiments. Inertia is also responsible for the difference

between the wetting and dewetting path, which is predicted to be the same (apart the direction) in quasi static theories.

To conclude, in this thesis I developed a theory of the wetting, recovery and bubble nucleation going beyond the state of the art. In particular, I extended quasi-static theories to include dynamical effects and this proved to be crucial in the modeling of the processes of our interest at operative/experimental conditions. In addition, the simulation of phase change systems with growing/shrinking domains at different pressure required the development of a novel barostating strategy to go beyond standard approaches developed for homogeneous systems.

Bibliography

[Allen et al., 2006a] Allen, R. J., Frankel, D., and ten Wolde P. R. (2006a). Simulating rare events in equilibrium or nonequilibrium stochastic systems. *J. Phys. Chem.*, 124:024102.

[Allen et al., 2006b] Allen, R. J., Frenkel, D., and ten Wolde, P. R. (2006b). Forward flux sampling-type schemes for simulating rare events: Efficiency analysis. *The Journal of chemical physics*, 124(19):194111.

[Allen et al., 2006c] Allen, R. J., Frenkel, D., and ten Wolde, P. R. (2006c). Simulating rare events in equilibrium or nonequilibrium stochastic systems. *The Journal of Chemical Physics*, 124(2):024102–17.

[Allen et al., 2009] Allen, R. J., Valeriani, C., and ten Wolde, P. R. (2009). Forward flux sampling for rare event simulations. *Journal of physics: Condensed matter*, 21(46):463102.

[Allen et al., 2005] Allen, R. J., Warren, P. B., and ten Wolde P. R. (2005). Sampling rare switching events in biochemical networks. *Phys. Rev. Lett.*, 94:018104.

[Amabili et al., 2016a] Amabili, M., Giacomello, A., Meloni, S., and Casciola, C. M. (2016a). Intrusion and extrusion of a liquid on nanostructured surfaces. *Journal of Physics: Condensed Matter*, 29(1):014003.

[Amabili et al., 2016b] Amabili, M., Giacomello, A., Meloni, S., and Casciola, C. M. (2016b). Unraveling the salvinia paradox: design principles for submerged superhydrophobicity. *arXiv preprint arXiv:1612.01769*.

[Amabili et al., 2017] Amabili, M., Meloni, S., Giacomello, A., and Casciola, C. M. (2017). Activated wetting of nanostructured surfaces: Reaction coordinates, finite size effects, and simulation pitfalls. *The Journal of Physical Chemistry B*, 122(1):200–212.

[Andersen, 1980] Andersen, H. C. (1980). Molecular dynamics simulations at constant pressure and/or temperature. *J. Chem. Phys.*, 72(4):2384–2393.

[Atchley and Prosperetti, 1989] Atchley, A. A. and Prosperetti, A. (1989). The crevice model of bubble nucleation. *The Journal of the Acoustical Society of America*, 86(3):1065–1084.

[Azouzi et al., 2013] Azouzi, M. E. M., Ramboz, C., Lenain, J.-F., and Caupin, F. (2013). A coherent picture of water at extreme negative pressure. *Nature Physics*, 9(1):38.

[Baidakov and Bobrov, 2014] Baidakov, V. and Bobrov, K. (2014). Spontaneous cavitation in a lennard-jones liquid at negative pressures. *The Journal of chemical physics*, 140(18):184506.

[Barthlott and Neinhuis, 1997] Barthlott, W. and Neinhuis, C. (1997). Purity of the sacred lotus, or escape from contamination in biological surfaces. *Planta*, 202(1):1–8.

[Betz et al., 2013] Betz, A. R., Jenkins, J., Attinger, D., et al. (2013). Boiling heat transfer on superhydrophilic, superhydrophobic, and superbiphilic surfaces. *International Journal of Heat and Mass Transfer*, 57(2):733–741.

[Blake and Gibson, 1987] Blake, J. R. and Gibson, D. (1987). Cavitation bubbles near boundaries. *Annual review of fluid mechanics*, 19(1):99–123.

[Blander and Katz, 1975] Blander, M. and Katz, J. L. (1975). Bubble nucleation in liquids. *AIChE Journal*, 21(5):833–848.

[Bolhuis, 2003] Bolhuis, P. G. (2003). Transition-path sampling of β-hairpin folding. *Proceedings of the National Academy of Sciences*, 100(21):12129–12134.

[Bonella et al., 2012] Bonella, S., Meloni, S., and Ciccotti, G. (2012). Theory and methods for rare events. *Eur. Phys. J. B*, 85(3):1–19.

[Bremond et al., 2005] Bremond, N., Arora, M., Ohl, C.-D., and Lohse, D. (2005). Cavitation on surfaces. *Journal of physics: Condensed matter*, 17(45):S3603.

[Brennen, 2013] Brennen, C. E. (2013). *Cavitation and bubble dynamics*. Cambridge University Press.

[Cahn and Hilliard, 1959] Cahn, J. W. and Hilliard, J. E. (1959). Free energy of a nonuniform system. iii. nucleation in a two-component incompressible fluid. *The Journal of chemical physics*, 31(3):688–699.

[Cao et al., 2009] Cao, L., Jones, A. K., Sikka, V. K., Wu, J., and Gao, D. (2009). Anti-Icing Superhydrophobic Coatings. *Langmuir*, 25(21):12444–12448.

[Cassie and Baxter, 1944] Cassie, A. and Baxter, S. (1944). Wettability of porous surfaces. *Transactions of the Faraday society*, 40:546–551.

[Caupin and Herbert, 2006] Caupin, F. and Herbert, E. (2006). Cavitation in water: a review. *Comptes Rendus Physique*, 7(9-10):1000–1017.

[Chandler, 2005] Chandler, D. (2005). Interfaces and the driving force of hydrophobic assembly. *Nature*, 437(7059):640.

[Checco et al., 2014] Checco, A., Ocko, B. M., Rahman, A., Black, C. T., Tasinkevych, M., Giacomello, A., and Dietrich, S. (2014). Collapse and reversibility of the superhydrophobic state on nanotextured surfaces. *Physical Review Letters*, 112(21):216101.

[Chen et al., 1999] Chen, W., Fadeev, A. Y., Hsieh, M. C., Öner, D., Youngblood, J., and McCarthy, T. J. (1999). Ultrahydrophobic and ultralyophobic surfaces: some comments and examples. *Langmuir*, 15(10):3395–3399.

[Ciccotti and Meloni, 2011] Ciccotti, G. and Meloni, S. (2011). Temperature accelerated monte carlo (tamc): a method for sampling the free energy surface of non-analytical collective variables. *Phys. Chem. Chem. Phys.*, 13(13):5952–5959.

[Coussios and Roy, 2008] Coussios, C. C. and Roy, R. A. (2008). Applications of acoustics and cavitation to noninvasive therapy and drug delivery. *Annu. Rev. Fluid Mech.*, 40:395–420.

[Daniello et al., 2009] Daniello, R. J., Waterhouse, N. E., and Rothstein, J. P. (2009). Drag reduction in turbulent flows over superhydrophobic surfaces. *Physics of Fluids*, 21(8):085103.

[Debenedetti, 1996] Debenedetti, P. G. (1996). *Metastable liquids: concepts and principles*. Princeton University Press.

[Diemand et al., 2014] Diemand, J., Angélil, R., Tanaka, K. K., and Tanaka, H. (2014). Direct simulations of homogeneous bubble nucleation: Agreement with classical nucleation theory and no local hot spots. *Physical review E*, 90(5):052407.

[Duane et al., 1987] Duane, S., Kennedy, A. D., Pendleton, B. J., and Roweth, D. (1987). Hybrid monte carlo. *Physics letters B*, 195(2):216–222.

[E et al., 2017] E, J., Jin, Y., Deng, Y., Zuo, W., Zhao, X., Han, D., Peng, Q., and Zhang, Z. (2017). Wetting Models and Working Mechanisms of Typical Surfaces Existing in Nature and Their Application on Superhydrophobic Surfaces: A Review. *Advanced Materials Interfaces*, 5(1):1701052–39.

[Elena et al., 2013] Elena, A. M., Meloni, S., and Ciccotti, G. (2013). Equilibrium and rate constants, and reaction mechanism of the hf dissociation in the hf (h2o) 7 cluster by ab initio rare event simulations. *J. Phys. Chem. A*, 117(49):13039–13050.

[Enright et al., 2014a] Enright, R., Miljkovic, N., Alvarado, J. L., Kim, K., and Rose, J. W. (2014a). Dropwise Condensation on Micro- and Nanostructured Surfaces. *Nanoscale and Microscale Thermophysical Engineering*, 18(3):223–250.

[Enright et al., 2014b] Enright, R., Miljkovic, N., Alvarado, J. L., Kim, K., and Rose, J. W. (2014b). Dropwise condensation on micro-and nanostructured surfaces. *Nanoscale and Microscale Thermophysical Engineering*, 18(3):223–250.

[Eroshenko et al., 2001] Eroshenko, V., Regis, R.-C., Soulard, M., and Patarin, J. (2001). Energetics: a new field of applications for hydrophobic zeolites. *Journal of the American Chemical Society*, 123(33):8129–8130.

[Errington et al., 2003] Errington, J. R., Debenedetti, P. G., and Torquato, S. (2003). Quantification of order in the lennard-jones system. *J. Chem. Phys.*, 118(5):2256–2263.

[Espinosa et al., 2016] Espinosa, J. R., Vega, C., Valeriani, C., and Sanz, E. (2016). Seeding approach to crystal nucleation. *The Journal of Chemical Physics*, 144(3):034501–11.

[Evans and Holian, 1985] Evans, D. J. and Holian, B. L. (1985). The nose–hoover thermostat. *The Journal of chemical physics*, 83(8):4069–4074.

[Eyring, 1935] Eyring, H. (1935). The activated complex in chemical reactions. *The Journal of Chemical Physics*, 3(2):107–115.

[Feng et al., 2002] Feng, L., Li, S., Li, Y., Li, H., Zhang, L., Zhai, J., Song, Y., Liu, B., Jiang, L., and Zhu, D. (2002). Super-hydrophobic surfaces: from natural to artificial. *Advanced materials*, 14(24):1857–1860.

[Ferrari and Benedetti, 2015] Ferrari, M. and Benedetti, A. (2015). Superhydrophobic surfaces for applications in seawater. *Advances in Colloid and Interface Science*, 222(C):291–304.

[Frenkel and Smit, 2001] Frenkel, D. and Smit, B. (2001). *Understanding molecular simulation: from algorithms to applications*, volume 1. Elsevier.

[Gallo et al., 2018] Gallo, M., Magaletti, F., and Casciola, C. M. (2018). Thermally activated vapor bubble nucleation: The landau-lifshitz–van der waals approach. *Physical Review Fluids*, 3(5):053604.

[Giacomello et al., 2012a] Giacomello, A., Chinappi, M., Meloni, S., and Casciola, C. (2012a). Metastable Wetting on Superhydrophobic Surfaces: Continuum and Atomistic Views of the Cassie-Baxter–Wenzel Transition. *Phys. Rev. Lett.*, 109(22):226102.

[Giacomello et al., 2013] Giacomello, A., Chinappi, M., Meloni, S., and Casciola, C. M. (2013). Geometry as a catalyst: how vapor cavities nucleate from defects. *Langmuir*, 29(48):14873–14884.

[Giacomello et al., 2012b] Giacomello, A., Meloni, S., Chinappi, M., and Casciola, C. (2012b). Cassie–Baxter and Wenzel states on a nanostructured surface: phase diagram, metastabilities, and transition mechanism by atomistic free energy calculations. *Langmuir*, 28(29):10764–10772.

[Giacomello et al., 2015] Giacomello, A., Meloni, S., Müller, M., and Casciola, C. (2015). Mechanism of the Cassie-Wenzel transition via the atomistic and continuum string methods. *J. Chem. Phys.*, 142(10):104701.

[Giacomello et al., 2016a] Giacomello, A., Schimmele, L., and Dietrich, S. (2016a). Wetting hysteresis induced by nanodefects. *Proceedings of the National Academy of Sciences*, 113(3):E262–E271.

[Giacomello et al., 2016b] Giacomello, A., Schimmele, L., Dietrich, S., and Tasinkevych, M. (2016b). Perpetual superhydrophobicity. *Soft matter*, 12(43):8927–8934.

[Glowacki et al., 2009] Glowacki, D. R., Paci, E., and Shalashilin, D. V. (2009). Boxed Molecular Dynamics: A Simple and General Technique for Accelerating Rare Event Kinetics and Mapping Free Energy in Large Molecular Systems. *The Journal of Physical Chemistry B*, 113(52):16603–16611.

[González et al., 2014] González, M. A., Menzl, G., Aragones, J. L., Geiger, P., Caupin, F., Abascal, J. L., Dellago, C., and Valeriani, C. (2014). Detecting vapour bubbles in simulations of metastable water. *J. Chem. Phys.*, 141(18):18C511.

[Grate et al., 2012] Grate, J. W., Dehoff, K. J., Warner, M. G., Pittman, J. W., Wietsma, T. W., Zhang, C., and Oostrom, M. (2012). Correlation of oil–water and air–water contact angles of diverse silanized surfaces and relationship to fluid interfacial tensions. *Langmuir*, 28(18):7182–7188.

[Grünwald et al., 2006] Grünwald, M., Rabani, E., and Dellago, C. (2006). Mechanisms of the wurtzite to rocksalt transformation in cdse nanocrystals. *Physical review letters*, 96(25):255701.

[Hänggi et al., 1990] Hänggi, P., Talkner, P., and Borkovec, M. (1990). Reaction-rate theory: fifty years after kramers. *Reviews of modern physics*, 62(2):251.

[Horn et al., 2004] Horn, H. W., Swope, W. C., Pitera, J. W., Madura, J. D., Dick, T. J., Hura, G. L., and Head-Gordon, T. (2004). Development of an improved four-site water model for biomolecular simulations: Tip4p-ew. *J. Chem. Phys.*, 120(20):9665–9678.

[Howarter and Youngblood, 2008] Howarter, J. A. and Youngblood, J. P. (2008). Self-Cleaning and Next Generation Anti-Fog Surfaces and Coatings. *Macromolecular Rapid Communications*, 29(6):455–466.

[Huang, 2009] Huang, K. (2009). *Introduction to statistical physics*. Chapman and Hall/CRC.

[Irving and Kirkwood, 1950] Irving, J. and Kirkwood, J. G. (1950). The statistical mechanical theory of transport processes. iv. the equations of hydrodynamics. *J. Chem. Phys.*, 18(6):817–829.

[Joanny and De Gennes, 1984] Joanny, J. and De Gennes, P.-G. (1984). A model for contact angle hysteresis. *The journal of chemical physics*, 81(1):552–562.

[Johnson Jr and Dettre, 1964] Johnson Jr, R. E. and Dettre, R. H. (1964). Contact angle hysteresis. iii. study of an idealized heterogeneous surface. *The journal of physical chemistry*, 68(7):1744–1750.

[Jungblut and Dellago, 2016] Jungblut, S. and Dellago, C. (2016). Pathways to self-organization: Crystallization via nucleation and growth. *The European Physical Journal E*, 39(8):77.

[Kelton and Greer, 2010] Kelton, K. and Greer, A. L. (2010). *Nucleation in condensed matter: applications in materials and biology*, volume 15. Elsevier.

[Kramers, 1940] Kramers, H. A. (1940). Brownian motion in a field of force and the diffusion model of chemical reactions. *Physica*, 7(4):284–304.

[Kusumaatmaja et al., 2008] Kusumaatmaja, H., Blow, M., Dupuis, A., and Yeomans, J. (2008). The collapse transition on superhydrophobic surfaces. *EPL (Europhysics Letters)*, 81(3):36003.

[Lafuma and Quéré, 2003] Lafuma, A. and Quéré, D. (2003). Superhydrophobic states. *Nature materials*, 2(7):457.

[Laio and Gervasio, 2008] Laio, A. and Gervasio, F. L. (2008). Metadynamics: a method to simulate rare events and reconstruct the free energy in biophysics, chemistry and material science. *Reports on Progress in Physics*, 71(12):126601.

[Lauricella et al., 2017] Lauricella, M., Ciccotti, G., English, N. J., Peters, B., and Meloni, S. (2017). Mechanisms and nucleation rate of methane hydrate by dynamical nonequilibrium molecular dynamics. *The Journal of Physical Chemistry C*, page DOI: 10.1021/acs.jpcc.7b05754.

[Lauricella et al., 2014] Lauricella, M., Meloni, S., English, N. J., Peters, B., and Ciccotti, G. (2014). Methane clathrate hydrate nucleation mechanism by advanced molecular simulations. *The Journal of Physical Chemistry C*, 118(40):22847–22857.

[Lauricella et al., 2015] Lauricella, M., Meloni, S., Liang, S., English, N. J., Kusalik, P. G., and Ciccotti, G. (2015). Clathrate structure-type recognition: application to hydrate nucleation and crystallisation. *The Journal of chemical physics*, 142(24):244503.

[Lee and Kim, 2011] Lee, C. and Kim, C.-J. (2011). Underwater restoration and retention of gases on superhydrophobic surfaces for drag reduction. *Physical Review Letters*, 106(1):014502.

[Li et al., 2017] Li, Y., Quéré, D., Lv, C., and Zheng, Q. (2017). Monostable superrepellent materials. *Proceedings of the National Academy of Sciences USA*, 114(13):3387–3392.

[Li and Ren, 2014] Li, Y. and Ren, W. (2014). Numerical study of vapor condensation on patterned hydrophobic surfaces using the string method. *Langmuir*, 30(31):9567–9576.

[Lisi et al., 2017] Lisi, E., Amabili, M., Meloni, S., Giacomello, A., and Casciola, C. M. (2017). Self-recovery superhydrophobic surfaces: Modular design. *ACS Nano*, DOI: 10.1021/acsnano.7b06438.

[Lv et al., 2015] Lv, P., Xue, Y., Liu, H., Shi, Y., Xi, P., Lin, H., and Duan, H. (2015). Symmetric and asymmetric meniscus collapse in wetting transition on submerged structured surfaces. *Langmuir*, 31(4):1248–1254.

[Magaletti et al., 2015] Magaletti, F., Marino, L., and Casciola, C. M. (2015). Shock wave formation in the collapse of a vapor nanobubble. *Physical review letters*, 114(6):064501.

[Maragliano and Vanden-Eijnden, 2006a] Maragliano, L. and Vanden-Eijnden, E. (2006a). A temperature accelerated method for sampling free energy and determining reaction pathways in rare events simulations. *Chemical physics letters*, 426(1):168–175.

[Maragliano and Vanden-Eijnden, 2006b] Maragliano, L. and Vanden-Eijnden, E. (2006b). A temperature accelerated method for sampling free energy and determining reaction pathways in rare events simulations. *Chem. phys. lett.*, 426(1):168–175.

[Marchio et al., 2018] Marchio, S., Meloni, S., Giacomello, A., Valeriani, C., and Casciola, C. (2018). Pressure control in interfacial systems: Atomistic simulations of vapor nucleation. *The Journal of chemical physics*, 148(6):064706.

[Martyna et al., 1992] Martyna, G. J., Klein, M. L., and Tuckerman, M. (1992). Nosé–hoover chains: the canonical ensemble via continuous dynamics. *J. Chem. Phys.*, 97:2635.

[Martyna et al., 1994] Martyna, G. J., Tobias, D. J., and Klein, M. L. (1994). Constant pressure molecular dynamics algorithms. *J. Chem. Phys.*, 101(5):4177–4189.

[Meadley and Escobedo, 2012] Meadley, S. L. and Escobedo, F. A. (2012). Thermodynamics and kinetics of bubble nucleation: Simulation methodology. *J. Chem. Phys.*, 137(7):074109.

[Mehlig et al., 1992] Mehlig, B., Heermann, D., and Forrest, B. (1992). Hybrid monte carlo method for condensed-matter systems. *Physical Review B*, 45(2):679.

[Melchionna et al., 1993] Melchionna, S., Ciccotti, G., and Lee Holian, B. (1993). Hoover npt dynamics for systems varying in shape and size. *Mol. Phys.*, 78(3):533–544.

[Meloni and Ciccotti, 2015] Meloni, S. and Ciccotti, G. (2015). Free energies for rare events: Temperature accelerated md and mc. *Eur. Phys. J. Special Topics*, 12(224):2389–2407.

[Meloni et al., 2016] Meloni, S., Giacomello, A., and Casciola, C. M. (2016). Focus article: Theoretical aspects of vapor/gas nucleation at structured surfaces. *The Journal of Chemical Physics*, 145(21):211802.

[Menzl et al., 2016] Menzl, G., Gonzalez, M. A., Geiger, P., Caupin, F., Abascal, J. L., Valeriani, C., and Dellago, C. (2016). Molecular mechanism for cavitation in water under tension. *Proc. Natl. Acad. Sci. USA*, 113(48):13582–13587.

[Miwa et al., 2000] Miwa, M., Nakajima, A., Fujishima, A., Hashimoto, K., and Watanabe, T. (2000). Effects of the Surface Roughness on Sliding Angles of Water Droplets on Superhydrophobic Surfaces. *Langmuir*, 16:5754–5760.

[Neppiras, 1980] Neppiras, E. A. (1980). Acoustic cavitation. *Physics reports*, 61(3):159–251.

[Nosonovsky and Bhushan, 2009] Nosonovsky, M. and Bhushan, B. (2009). Superhydrophobic surfaces and emerging applications: Non-adhesion, energy, green engineering. *Current Opinion in Colloid & Interface Science*, 14(4):270–280.

[Öner and McCarthy, 2000] Öner, D. and McCarthy, T. J. (2000). Ultrahydrophobic surfaces. effects of topography length scales on wettability. *Langmuir*, 16(20):7777–7782.

[Panagiotopoulos, 1987] Panagiotopoulos, A. Z. (1987). Constant pressure molecular dynamics algorithms. *Mol. Phys.*, 61(4):813–826.

[Panter and Kusumaatmaja, 2017] Panter, J. R. and Kusumaatmaja, H. (2017). The impact of surface geometry, cavitation, and condensation on wetting transitions: posts and reentrant structures. *Journal of Physics: Condensed Matter*, 29:084001.

[Parrinello and Rahman, 1981] Parrinello, M. and Rahman, A. (1981). Polymorphic transitions in single crystals: A new molecular dynamics method. *J. Appl. Phys.*, 52(12):7182–7190.

[Pashos et al., 2015] Pashos, G., Kokkoris, G., and Boudouvis, A. G. (2015). Minimum energy paths of wetting transitions on grooved surfaces. *Langmuir*, 31(10):3059–3068.

[Pashos et al., 2016] Pashos, G., Kokkoris, G., Papathanasiou, A., and Boudouvis, A. (2016). Wetting transitions on patterned surfaces with diffuse interaction potentials embedded in a young-laplace formulation. *The Journal of Chemical Physics*, 144(3):034105.

[Patankar, 2010] Patankar, N. A. (2010). Supernucleating surfaces for nucleate boiling and dropwise condensation heat transfer. *Soft Matter*, 6(8):1613–8.

[Plimpton, 1995] Plimpton, S. (1995). Fast parallel algorithms for short-range molecular dynamics. *J. Comp. Phys.*, 117(1):1–19.

[Poetes et al., 2010] Poetes, R., Holtzmann, K., Franze, K., and Steiner, U. (2010). Metastable underwater superhydrophobicity. *Physical review letters*, 105(16):166104.

[Prakash et al., 2016] Prakash, S., Xi, E., and Patel, A. J. (2016). Spontaneous recovery of superhydrophobicity on nanotextured surfaces. *Proceedings of the National Academy of Sciences*, 113(20):5508–5513.

[Ren, 2014] Ren, W. (2014). Wetting transition on patterned surfaces: transition states and energy barriers. *Langmuir*, 30(10):2879–2885.

[Rowlinson and Widom, 2013] Rowlinson, J. S. and Widom, B. (2013). *Molecular Theory of Capillarity*. Courier Corporation.

[Savoy and Escobedo, 2012a] Savoy, E. S. and Escobedo, F. A. (2012a). Molecular simulations of wetting of a rough surface by an oily fluid: Effect of topology, chemistry, and droplet size on wetting transition rates. *Langmuir*, 28(7):3412–3419.

[Savoy and Escobedo, 2012b] Savoy, E. S. and Escobedo, F. A. (2012b). Simulation study of free-energy barriers in the wetting transition of an oily fluid on a rough surface with reentrant geometry. *Langmuir*, 28(46):16080–16090.

[Sharma and Debenedetti, 2012] Sharma, S. and Debenedetti, P. G. (2012). Evaporation rate of water in hydrophobic confinement. *Proceedings of the National Academy of Sciences*, 109(12):4365–4370.

[Shen and Debenedetti, 1999] Shen, V. K. and Debenedetti, P. G. (1999). A computational study of homogeneous liquid–vapor nucleation in the lennard-jones fluid. *J. chem. phys.*, 111(8):3581–3589.

[Skripov et al., 1988] Skripov, V. P., Sinitsyn, E., Pavlov, P., Ermakov, G., Muratov, G., Bulanov, N., and Baidakov, V. (1988). Thermophysical properties of liquids in the metastable (superheated) state.

[Sloan Jr, 2003] Sloan Jr, E. D. (2003). Fundamental principles and applications of natural gas hydrates. *Nature*, 426(6964):353.

[Smith and Frenkel, 2002] Smith, B. and Frenkel, D. (2002). Understanding molecular simulation: From algorithms to applications. *Academic, San Diego*.

[Sprik and Ciccotti, 1998] Sprik, M. and Ciccotti, G. (1998). Free energy from constrained molecular dynamics. *The Journal of chemical physics*, 109(18):7737–7744.

[Suslick et al., 1999] Suslick, K. S., Didenko, Y., Fang, M. M., Hyeon, T., Kolbeck, K. J., McNamara, W. B., Mdleleni, M. M., and Wong, M. (1999). Acoustic cavitation and its chemical consequences. *Philosophical Transactions of the Royal Society of London A: Mathematical, Physical and Engineering Sciences*, 357(1751):335–353.

[Tolman, 1949] Tolman, R. C. (1949). The effect of droplet size on surface tension. *The journal of chemical physics*, 17(3):333–337.

[Torrie and Valleau, 1977] Torrie, G. M. and Valleau, J. P. (1977). Nonphysical sampling distributions in Monte Carlo free-energy estimation: Umbrella sampling. *Journal of Computational Physics*, 23(2):187–199.

[Tretyakov and Müller, 2013] Tretyakov, N. and Müller, M. (2013). Correlation between surface topography and slippage: a molecular dynamics study. *Soft Matter*, 9(13):3613–3623.

[Truesdell et al., 2006] Truesdell, R., Mammoli, A., Vorobieff, P., van Swol, F., and Brinker, C. J. (2006). Drag reduction on a patterned superhydrophobic surface. *Physical review letters*, 97(4):044504.

[Tuckerman, 2010] Tuckerman, M. (2010). *Statistical mechanics: theory and molecular simulation*. Oxford university press.

[Valeriani et al., 2007] Valeriani, C., Allen, R. J., Morelli, M. J., Frenkel, D., and Rein ten Wolde, P. (2007). Computing stationary distributions in equilibrium and nonequilibrium systems with forward flux sampling. *The Journal of chemical physics*, 127(11):114109.

[van Erp et al., 2003] van Erp, T. S., Moroni, D., and Bolhuis, P. G. (2003). A novel path sampling method for the calculation of rate constants. *The Journal of Chemical Physics*, 118(17):7762–7774.

[Vega et al., 2006] Vega, C., Abascal, J., and Nezbeda, I. (2006). Vapor-liquid equilibria from the triple point up to the critical point for the new generation of tip4p-like models: Tip4p/ew, tip4p/2005, and tip4p/ice. *The Journal of chemical physics*, 125(3):034503.

[Vrancken et al., 2009] Vrancken, R. J., Kusumaatmaja, H., Hermans, K., Prenen, A. M., Pierre-Louis, O., Bastiaansen, C. W., and Broer, D. J. (2009). Fully reversible transition from wenzel to cassie- baxter states on corrugated superhydrophobic surfaces. *Langmuir*, 26(5):3335–3341.

[Wang et al., 2017] Wang, Y., Zaytsev, M. E., The, H. L., Eijkel, J. C., Zandvliet, H. J., Zhang, X., and Lohse, D. (2017). Vapor and gas-bubble growth dynamics around laser-irradiated, water-immersed plasmonic nanoparticles. *ACS nano*, 11(2):2045–2051.

[Wang et al., 2008] Wang, Z.-J., Valeriani, C., and Frenkel, D. (2008). Homogeneous bubble nucleation driven by local hot spots: A molecular dynamics study. *J. Phys. Chem. B*, 113(12):3776–3784.

[Wedekind and Reguera, 2008] Wedekind, J. and Reguera, D. (2008). Kinetic reconstruction of the free-energy landscape. *The Journal of Physical Chemistry B*, 112(35):11060–11063.

[Wenzel, 1936] Wenzel, R. N. (1936). Resistance of solid surfaces to wetting by water. *Industrial & Engineering Chemistry*, 28(8):988–994.

[Xiang et al., 2017] Xiang, Y., Huang, S., Lv, P., Xue, Y., Su, Q., and Duan, H. (2017). Ultimate stable underwater superhydrophobic state. *Physical review letters*, 119(13):134501.

[Xue et al., 2016] Xue, Y., Lv, P., Lin, H., and Duan, H. (2016). Underwater superhydrophobicity: Stability, design and regulation, and applications. *Applied Mechanics Reviews*, 68(3):030803.

[Yao and Ren, 2015] Yao, W. and Ren, W. (2015). Liquid-vapor transition on patterned solid surfaces in a shear flow. *The Journal of Chemical Physics*, 143(24):244701.

[Zhang et al., 2016a] Zhang, M., Feng, S., Wang, L., and Zheng, Y. (2016a). Lotus effect in wetting and self-cleaning. *BIOTRI*, 5(C):31–43.

[Zhang et al., 2016b] Zhang, S., Huang, J., Chen, Z., and Lai, Y. (2016b). Bioinspired Special Wettability Surfaces: From Fundamental Research to Water Harvesting Applications. *Small*, 13(3):1602992–28.

[Zhang et al., 2008] Zhang, X., Shi, F., Niu, J., Jiang, Y., and Wang, Z. (2008). Superhydrophobic surfaces: from structural control to functional application. *Journal of Materials Chemistry*, 18:621–633.

[Zheng et al., 1991] Zheng, Q., Durben, D., Wolf, G., and Angell, C. (1991). Liquids at large negative pressures: water at the homogeneous nucleation limit. *Science*, 254(5033):829–832.

[Zwanzig, 2001] Zwanzig, R. (2001). *Nonequilibrium statistical mechanics*. Oxford University Press.